A Study of Biomedical Time Series Using Empirical Mode Decomposition

Extracting event-related modes from EEG signals recorded during visual processing of contour stimuli

Inaugural-Dissertation zur Erlangung der Doktorwürde
der Fakultät für Sprach-, Literatur- und Kulturwissenschaften

der Universität Regensburg

Vorgelegt von
Karema S. A. Al-Subari
aus
Thamar, Yemen

SUBMITTED IN FULFILLMENT
OF THE REQUIREMENTS FOR
THE DEGREE OF DOCTOR OF
PHILOSOPHY IN INFORMATION
SCIENCE

2017

Erstgutachter: Prof. Dr. rer. soc. Rainer Hammwöhner and Prof. Dr.-Ing. Bernd Ludwig
Zweitgutachter: Prof. Dr. rer. nat. Elmar Wolfgang Lang

Acknowledgements

Foremost, I would like to express my special appreciation and thanks to my advisor Prof. Dr. Elmar Lang, you have been an outstanding mentor for me. I would like to thank you for encouraging my research and for allowing me to grow as a research scientist. I am very grateful for your patience, motivation, enthusiasm, and immense knowledge that, taken together, make you a great mentor. Words can not express my gratitude for all that you have done. This thank is not enough. But, I want to thank you. Thank you for listening to me, for genuinely asking how I was doing, for being such a positive light.

I would also like to thank Prof. Dr. Rainer Hammwöhner for providing me with the opportunity to do my PhD thesis within his group. As far as I regret that he is not able to witness the present day, I am absolutely convinced that his memory will always be with me.

My gratitude also goes to Prof. Dr. Bernd Ludwig who accepted to be my first supervisor after the sudden death of Prof. Dr. Rainer Hammwöhner. I really appreciate your very careful review of my thesis, comments, corrections and suggestions that ensued. They were valuable and very helpful to improve my thesis.

A very special thanks goes to Prof. Dr. Anna Maria Tomé and Dr. Gregor Volberg for sharing their knowledge and having always an open ear for discussion.

I also want to thank present and past members of Computational Intelligence and Machine Learning Group (CIML) for their assistance and having a good time. I can never forget the warm and friendly atmosphere of the entire CIML group. I wish everybody all the best and good luck with your lives.

My sincere thanks go to my family. Without their love and support over the years, none of this would have been possible. To my darling husband Saad for his constant encouragement and belief in me. I appreciate everything that you are trying to do for me and for our family. To my beloved daughters Sulaf and Celine, you are truly gifts from God. You have always been the source of my joy and I will always do what is best for you.

To everybody else who accompanied me in this beautiful PhD journey: THANK YOU!

The first and last thank goes to God for blessing me much more than I deserve.

Abstract

Noninvasive neuroimaging techniques like functional Magnetic Resonance Imaging (fMRI) and/or Electroencephalography (EEG) allow researchers to investigate and analyze brain activities during visual processing. EEG offers a high temporal resolution at a level of submilliseconds which can be combined favorably with fMRI which has a good spatial resolution on small spatial scales in the millimeter range. These neuroimaging techniques were, and still are instrumental in the diagnoses and treatments of neurological disorders in the clinical applications. In this PhD thesis we concentrate on electrophysiological signatures within EEG recordings of a combined EEG-fMRI data set which where taken while performing a contour integration task. The estimation of location and distribution of the electrical sources in the brain from surface recordings which are responsible for interesting EEG waves has drawn the attention of many EEG/MEG researchers. However, this process which is called *brain source localization* is still one of the major problems in EEG. It consists of solving two modeling problems: forward and inverse. In the forward problem, one is interested in predicting the expected potential distribution on the scalp from given electrical sources that represent active neurons in the head. These evaluations are necessary to solve the inverse problem which can be defined as the problem of estimating the brain sources that generated the measured electrical potentials. This thesis presents a data-driven analysis of EEG data recorded during a combined EEG/fMRI study of visual processing during a contour integration task. The analysis is based on an ensemble empirical mode decomposition (EEMD) and discusses characteristic features of event related modes (ERMs) resulting from the decomposition. We identify clear differences in certain ERMs in response to contour vs non-contour Gabor stimuli mainly for response amplitudes peaking around 100 $[ms]$ (called $P100$) and 200 $[ms]$ (called $N200$) after stimulus onset, respectively. We observe early $P100$ and $N200$ responses at electrodes located in the occipital area of the brain, while late $P100$ and $N200$ responses appear at electrodes located in frontal brain areas. Signals at electrodes in central brain areas show bimodal early/late response signatures in certain ERMs. Head topographies clearly localize statistically significant response differences to both stimulus conditions. Our findings provide an independent proof of recent models which suggest that contour integration depends on distributed network activity within the brain.
Next and based on the previous analysis, a new approach for source localization of EEG data based on combining ERMs, extracted with EEMD, with inverse models has been presented. As the first step, 64 channel EEG recordings are pooled according to six brain areas and decomposed, by applying an EEMD, into their underlying ERMs. Then, based upon the problem at hand, the most closely related ERM, in terms of frequency and amplitude, is combined with inverse modeling techniques for source localization. More specifically, the

standardized low resolution brain electromagnetic tomography (sLORETA) procedure is employed in this work. Accuracy and robustness of the results indicate that this approach deems highly promising in source localization techniques for EEG data.
Given the results of analyses above, it can be said that EMD is able to extract intrinsic signal modes, ERMs, which contain decisive information about responses to contour and non-contour stimuli. Hence, we introduce a new toolbox, called EMDLAB, which serves the growing interest of the signal processing community in applying EMD as a decomposition technique. EMDLAB can be used to perform, easily and effectively, four common types of EMD: plain EMD, ensemble EMD (EEMD), weighted sliding EMD (wSEMD) and multivariate EMD (MEMD) on the EEG data. The main goal of EMDLAB toolbox is to extract characteristics of either the EEG signal by intrinsic mode functions (IMFs) or ERMs. Since IMFs reflect characteristics of the original EEG signal, ERMs reflect characteristics of ERPs of the original signal. The new toolbox is provided as a plug-in to the well-known EEGLAB which enables it to exploit the advantageous visualization capabilities of EEGLAB as well as statistical data analysis techniques provided there for extracted IMFs and ERMs of the signal.

Abstrakt

Nichtinvasive bildgebende Verfahren der Hirnforschung wie etwa funktionelle Magnetresonanz-Tomographie (fMRT) oder Elektroenzephalographie (EEG) ermöglichen Forschern die Untersuchung und Analyse von Gehirnaktivitäten während der Verarbeitung visueller Information. EEG bietet eine hohe zeitliche Auflösung im sub-Millisekunden Bereich und kann vorteilhaft mit der Funktionellen MRT kombiniert werden, die eine gute räumliche Auflösung im Millimeterbereich bietet. Diese bildgebenden Verfahren waren und sind noch wesentlich für die Diagnose und Therapie neurologischer Erkrankungen in klinischen Behandlungen. In dieser Dissertation liegt das Augenmerk auf elektrophysiologischen Signaturen in EEG Aufzeichnungen eines fMRT-EEG Datensatzes während einer Kontourintegrationsaufgabe. Die Schätzung der räumlichen Verteilung elektrischer Signalquellen im Gehirn hat seit langem das Interesse vieler EEG/MEG – Forscher geweckt. Trotzdem ist diese Quellenlokalisation ein weitgehend ungelöstes Problem der EEG – Forschung. Es umfasst die Lösung zweier Teilprobleme: Der Schätzung der Verteilung elektrischer Aktivitätsherde auf der Schädeloberfläche (Forward problem) und die Lokalisation der ihnen zugrunde liegenden Signalquellen (inverse problem). Im Vorwärtsproblem wird also aus einer angenommenen räumlichen Verteilung von elektrischen Signalquellen (Dipolquellen) die flächenhafte Verteilung der zugehörigen elektrischen Potentiale auf der Schädeloberfläche geschätzt. Das inverse Problem versucht dagegen aus beobachteten Potentialverteilungen die räumliche Verteilung der zugehörigen Signalquellen zu schätzen. Die Dissertation präsentiert eine Daten-getriebene Analyse von EEG Signalen, die während einer Kontour – Integrationsaufgabe aufgezeichnet wurden. Die Analyse basiert auf einer empirischen Modenzerlegung und diskutiert charakteristische Merkmale Ereignis-bezogener Moden (ERMs), aus denen sich die Signale zusammensetzen. Die Analyse kann, bezüglich der beiden Stimulus Paradigmen (Kontour – nicht-Kontour), deutliche Unterschiede in bestimmten ERMs nachweisen. Dies gilt insbesondere für ERMs mit positiven Maxima (P100) etwa 100 ms nach Stimulus Präsentation bzw. negativen Extrema (N200) ca. 200 ms nach visueller Stimulation. Die Reizantworten P100 und N200 erscheinen in den frontalen Gehirnregionen ca. 70 ms verzögert gegenüber den entsprechenden Reizantworten, die im visuellen Kortex beobachtbar sind. Reizantworten, die an Elektroden in zentralen Gehirnregionen aufgenommen wurden, zeigen ein bi-modales Verhalten mit einer Signalaufspaltung in eine frühe und eine späte Reizantwort. Die Ergebnisse von Hypothesentests bzgl. der statistischen Signifikanz der Reizantworten können als topographische Karten visualisiert werden. Sie zeigen klar eingegrenzte Gebiete erhöhter neuronaler Aktivität im okzipitalen bzw. frontalen Kortex mit klaren Unterschieden bzgl der Stärke der Reizantwort. Diese Befunde liefern einen unabhängigen Beweis für die These, dass an der Kontourintegration neuronale Netzwerke

beteiligt sind, die über Gebiete im visuellen und frontalen Kortex umfassen. Mit Hilfe der empirischen Modenzerlegung konnte auch eine neue Methode der inversen Modellierung entwickelt werden, die eine Lokalisation der den beobachteten Potentialverteilungen zugrunde liegenden Signalquellen mit großer Präzision ermöglicht. Für die inverse Modellierung wurde eine als sLORETA bekannte und bewährte Methode der Quellenlokalisation eingesetzt. Schlieslich wurde noch eine neue Toolbox, EMDLAB genannt, entwickelt, die dem wachsenden Interesse der EEG Forscher an der empirischen Modenzerlegung Rechnung trägt und geeignete Werkzeuge zur EEG Analyse zur Verfügung stellt. EMDLAB umfasst viele wichtige EMD Dialekte wie etwa ensemble EMD, weighted sliding EMD und multi-variate EMD. Mit Hilfe der Toolbox können auch wichtige Charakteristika Ereignisbezogener Potentiale oder Ereignis-bezogener intrinsicher Moden gewonnen werden. Die Toolbox ist in Verbindung mit der weit verbreiteten Toolbox EEGLAB verwendbar und verwendet deren ausgezeichnete Visualisierungsmöglichkeiten und statistischen Analysewerkzeuge.

Table of Contents

List of Figures

List of Tables

List of Publications

Publications of author related to this thesis

[1] **K. Al-Subari**, S. Al-Baddai, A. Tomé, G. Volberg, R. Hammwöhner, and E.W. Lang. Ensemble empirical mode decomposition analysis of EEG data collected during a contour integration task. *PLoS ONE*, 10(4):e0119489, 04 2015.

[2] **K. Al-Subari**, S. Al-Baddai, A. Tomé, M. Goldhacker, R. Faltermeier, and E.W. Lang. EMDLAB:a toolbox for analysis of single-trial EEG dynamics using empirical mode decomposition. *Journal of Neuroscience Methods*, 253:193–205, 07 2015.

[3] **K. Al-Subari**, S. Al-Baddai, A. Tomé, G. Volberg, B. Ludwig, and E.W. Lang. Combined EMD - sLORETA Analysis of EEG Data Collected during a Contour Integration Task. *PLoS ONE*, 11(12):e0167957, 12 2016.

Other publications during the PhD study

[4] S. Al-Baddai, **K. Al-Subari**, A. Tomé, G. Volberg, S. Hanslmayr, R. Hammwöhner, and E.W. Lang. Bidimensional ensemble empirical mode decomposition of functional biomedical images taken during a contour integration task. *Biomedical Signal Processing and Control*, 13:218–236, 2014.

[5] S. Al-Baddai, **K. Al-Subari**, A. Tomé, G. Volberg, and E.W. Lang. A combined EMD - ICA analysis of simultaneously registered EEG-fMRI data. *BMVA*, 2015(2):1–15, 2015.

[6] E. Gallego-Jutglà, S. Al-Baddai, **K. Al-Subari**, A. Tomé, E. Lang, and J. Solé-Casals. Face recognition by fast and stable bi-dimensional empirical mode decomposition. *BIOSIGNALS 2015 - Proceedings of the International Conference on Bio-inspired Systems and Signal Processing, Lisbon, Portugal* ., 12-15 January:385-391, 2015.

[7] S. Al-Baddai, **K. Al-Subari**, A. Tomé, D. Salas-Gonzales, and E.W. Lang. Analysis of fmri images with BEEMD based-on green's functions. *Biomedical Signal Processing and Control*, 30:53–63, 2016.

[8] S. Al-Baddai, **K. Al-Subari**, A. Tomé, J. Sole-Casals, and E.W. Lang. A green's function-based bi-dimensional empirical mode decomposition. *Information Sciences*, 348:305–321, 2016.

[9] S. Al-Baddai, P. Marti, E. Gallego-Jutglà, **K. Al-Subari**, A. Tomé, E. W. Lang, and J. Solé-Casals. Bi-dimensional Empirical Mode Decomposition based Recognition System for Noisy Faces. *Pattern Recognition Letters*, Submitted (2017).

Chapter 1

Introduction

The mammalian visual system is able to recognize a multitude of objects within a visual scene. Object recognition presupposes the ability for contour integration and figure-ground separation. Visual integration is defined as the process of combining the output of neurons, which carry small attributes of a scene, into a complex structure more suitable for the guidance of behavior. Contour integration is one of the most elementary tasks during visual feature integration. Still it is debated whether contour integration is confined to the visual cortex or whether higher brain areas are involved as well. The traditional theory of visual processing suggests a hierarchy of serial processing steps through a bottom-up cascade of discrete visual areas [51]. But this strict bottom - up processing is challenged by more recent theories proposing a parallel bottom-up and top-down information flow [111]. The ability to integrate oriented contrast edges (Gabor elements) into a contour depends on the spacing and orientation of the Gabor elements relative to the path orientation [54][119]. Similar principles apply in the multi-stable organization of regular arrays of elements in rows and columns [34][35]. Other, more general, stimulus properties also seem to influence the binding of contour elements: Closed contours are more easily detected than open ones [109][165]. Likewise, symmetric contours are also easier to detect than asymmetric ones [128]. Indeed, contour integration improves when Gabor elements are oriented perpendicular to the contour within a closed area, and deteriorates, when these elements are oriented parallel to the contour [38].

Event - related potentials and contour integration

Analyzing brain activities during visual processing is largely based on non-invasive techniques like functional Magnetic Resonance Imaging (fMRI) and/or Electroencephalography (EEG). The former offers good spatial resolution [106], while the latter excels in temporal resolution hence finds applications also in brain - computer interfacing [230][212]. Traditionally, EEGs are studied at the level of event related potentials (ERPs) which represent averages over a sufficiently large number of single trial recordings. Characteristic ERP components and their related latencies are then compared for different stimulus conditions. Several studies investigate differences between contour and non-contour stimulus conditions for various components of event related potentials (ERPs) [26][127][216][141]. Such differ-

ences arise mostly for mean peak amplitudes of the ERP components $P1$ and $N1$ denoting the first positive and first negative components appearing after stimulus onset, respectively. Early studies already demonstrated that modulations during contour integration do not only vary with context but also with task demand [26]. This study already shows that contour integration involves a neural network including anterior and posterior brain areas in addition to the visual cortex. Recently, electrophysiological studies [127] provided further clear evidence that context modulates the electrophysiological signature of contour integration at early stages of visual processing. Modulating effects were mainly seen for the ERP components $N1$ and $P2$, corresponding to the first negative and the second positive ERP components appearing after stimulus onset. However, no effect was seen for the first positive ERP component $P1$. In summary, context primarily exerts a modulatory effect on the $N1$ component. These studies thus highlight the dynamic interplay between perceptual grouping and the context in which it operates. A more recent contour integration study using EEG analysis [216] advocated the hypothesis that perceptual grouping involves top-down selection rather than a mere pooling of afferent information streams encoding local elements in the visual field. Differential brain activity, i. e. statistically significant differences in stimulus response amplitudes for the ERP component $N1$, occurring roughly at a latency of $170 - 180$ $[ms]$, could be detected only during a contour integration task within parietal, lateral occipital and primary visual areas. If the contour stimuli were presented with a concurrent task (i.e., if the contours were not the detection target), then no differences in brain activity were found between contour and non-contour stimuli. The study concludes that contour integration seems to be based on selecting information from primary visual areas, and appears to be controlled by the lateral occipital cortex. This conclusion corroborates results of another recent EEG study on contour integration [217]. A contour and a non-contour stimulus were presented within the same trial in fast succession, with the task to indicate whether the contour was shown within the first or within the second presentation interval. As a result, differences in brain activity between contour and non-contour stimuli occurred for stimuli shown in the first interval, but were completely absent for stimuli shown in the second interval. Thus, top-down information obtained from the serial presentation shaped the brain activity in response to contour stimuli.

The above mentioned debate about competing theories concerning the mechanisms of contour integration has been the focus of yet another electrophysiological study. Tackling the question whether serial facilitative interactions between collinear cells in the primary visual cortex (V1) or pooling of inputs in higher-order visual areas determine contour integration, the authors applied high-density electrophysiological recordings to assess the spatio-temporal dynamics of brain activity in response to Gabor contour stimuli embedded in Gabor noise versus control stimuli. The study concluded that the earliest effects could be observed in the ERP component $N1$ rather than in the component $C1$ of the visual evoked potential. Inverse modeling identified sources in the lateral occipital complex (LOC) within the ventral visual stream as the generators of $N1$ modifications. Also modulatory contextual effects appeared only at this later processing period. The authors claim that these results are consistent with a pooling of information from primary visual areas in higher cortical areas only at a latency characteristic for the occurrence of the $N1$ stimulus response com-

ponent [198]. Concurrent to traditional ERP research, there is also increasing interest in oscillatory brain responses during contour integration. Oscillatory brain activity is thought to reflect rhythmic changes between relatively high and relatively low excitability within a neural population. By synchronizing neural activity, groups of neurons can be transiently linked into neural assemblies to jointly process a given task [61]. With respect to contour integration, several studies revealed local power increases in beta frequencies ($15-30Hz$) during contour compared to non-contour processing. The beta power difference occurred relatively early ($<160\ ms$) and mostly at parietal and occipital electrodes across studies [217][206]. Furthermore, increased neural long-range synchronization has been observed during contour compared to non-contour processing within theta (4-7 Hz) [73], alpha (8-12 Hz) [217] and beta frequencies [216]. Differences in high-frequency (gamma) oscillations, sometimes assumed to be a correlate of conscious visual perception [97], have not yet been found during contour integration. The results together show that brain activity differences during contour and non-contour processing are not only reflected in the ERP amplitude, but also in neural oscillations within low-to-mid frequencies.
Technically, EEG and fMRI data sets can be recorded in separate sessions or simultaneously. Integration of both, EEG and fMRI, recordings into one dataset for combined data analysis can be performed either in a symmetrical or an asymmetrical way. The latter methods include fMRI - directed EEG analysis and EEG-directed fMRI analysis [151]. Symmetrical data fusion methods mainly resort to different variants of Independent Component Analysis (ICA). Simultaneously recording EEG and fMRI signals is a demanding technique in terms of data recording and signal processing. However, their combination can reveal both the location of active brain areas and the temporal order of their activation. A very recent example is provided by a study of the dynamics of contour integration in the human brain, where EEG and fMRI data were acquired simultaneously during passively viewing Gabor stimuli under contour and non-contour conditions. By applying JointICA to the EEG and fMRI responses of the subjects, the authors gained temporally and spatially highly resolved brain responses during contour integration which could not be derived from unimodal recordings. Within EEG recordings, they found differences for stimuli with and without contours around 240 $[ms]$ after stimulus onset, in early visual (V1/V2) as well lateral occipital areas. Furthermore, they found an additional later activity, occurring roughly at a delay of 300 $[ms]$, in early visual areas for less salient contours, possibly reflecting re-entrant processing of such stimuli. Another combined EEG and fMRI study revealed that contour detection depends on the information transfer between lateral occipital and parietal brain areas [73], where a good detection performance required a high functional connectivity between these sites. Together these studies indicate that contour detection is accomplished within cortical networks, involving feedback loops between higher and lower visual processing areas.

Signal decomposition techniques

Several signal decomposition techniques are available for a more detailed data analysis. Especially artifact removal, i. e. the extraction of signal components unrelated to cognitive brain activities, using blind signal separation techniques like principal and independent com-

ponent analysis (PCA, ICA) are standard techniques available in toolboxes like EEGLAB [40]. Such exploratory data analysis is hampered by the intrinsically non-stationary nature, and the non-linear couplings involved in signal generation. To help alleviate such issues, recently, an empirical nonlinear analysis tool for complex, non-stationary temporal signal variations has been pioneered by N. E. Huang et al. [80]. Such technique is commonly referred to as Empirical Mode Decomposition (EMD), and, if combined with Hilbert spectral analysis, it is called *Hilbert - Huang Transform* (HHT). EMD utilizes empirical knowledge of oscillations intrinsic to a time series in order to represent them as a superposition of components with well defined instantaneous frequencies. They adaptively and locally decompose any non-stationary signal in a sum of *Intrinsic Mode Functions* (IMF) which represent zero-mean, amplitude- and (spatial-) frequency-modulated components. EMD represents a fully data-driven, unsupervised signal decomposition which does not need any *a priori* defined basis system. EMD also satisfies the perfect reconstruction property, i.e. superimposing all extracted IMFs together with the residual slowly varying trend reconstructs the original signal without information loss or distortion. Thus EMD lacks the scaling and permutation indeterminacy familiar from blind source separation (BSS) techniques. Because EMD operates on sequences of local extremes, and the decomposition is carried out by direct extraction of the local energy associated with the intrinsic time scales of the signal itself, the method is thus similar to traditional Fourier or Wavelet decompositions. It differs from the wavelet-based multi-scale analysis, however, which characterizes the scale of a signal event using pre-specified basis functions. Owing to this feature, EMD, and even more so its noise-assisted variant called *Ensemble Empirical Mode Decomposition* (EEMD), is a highly promising signal processing technique in dealing with problems of a multi-scale nature. Note that with EMD a data representation as an expansion into intrinsic modes is generated from the signal itself and no predefined basis system, as for example in Wavelet decompositions, is used for the signal representation. Thus an EMD decomposition reflects in a natural way the characteristics of non-stationary signals in either time or spatial domains. Note further that Fourier transforms have constant frequencies and weights, while Hilbert transforms allow the frequency as well as the amplitudes to vary over time.
Given the background discussed above, we suppose that EEMD is able to extract intrinsic signal modes, so-called event related modes (ERMs), which contain decisive information about responses to contour and non-contour stimuli. Such ERMs should appear at various electrode locations indicating the presence of extended neuronal networks which process such stimuli. We further hypothesize that such response signatures are better visible, with a high statistical significance, in these modes rather than in the original recordings. Also any latencies related to such signal components could be quantified more precisely.

Signal processing toolboxes

Brain states analysis using non-invasive monitoring techniques such as electroencephalogram (EEG) have been receiving much attention because of increasing interest and popularity of research related to brain computer/machine interfacing (BCI/BMI) methods, due to the very interesting possibility of computer-aided communication with the outside world

[183]. Therefore, this technology is expected to be at the core of future intelligent computing. Recently, several new signal processing methods have been used in EEG signal processing [129]. Most of these new methods need new tools to adapt routines of EEG data processing. Additionally, this sort of interactive tools makes the possibility of analysing the multimodal EEG data collected using more complex experimental designs much easier, for example a Neuroelectromagnetic Forward Head Modeling Toolbox(NFT) [1], a Source Information Flow Toolbox(SIFT) [146][41], Measure Projection Toolbox (MPT) [197] and Brain-Computer Interface LAP toolbox (BCILAB) [105][104]. These toolboxes are integrated with the well-established EEGLAB software environment [40], an interactive menu-based and scripting software for processing electrophysiological (EEG) data under the MATLAB interpreted programming script environment.
In this thesis, a new toolbox called EMDLAB which is an open software environment for electrophysiological data analysis is introduced. EMDLAB can be used to perform, easily and effectively, four common types of EMD: plain EMD, ensemble EMD (EEMD), weighted sliding EMD (wSEMD) and multivariate EMD (MEMD) on EEG data. The main purpose of EMDLAB toolbox is to extract characteristics of either the EEG signal by IMFs or ERMs. In EMDLAB, data structure and visualization of the extracted modes is adopted from the EEGLAB MATLAB toolbox [40], therefore it is proposed to use EMDLAB as a plug-in for EEGLAB. Similarly, the toolbox is mainly designed for EEG data, although both EEGLAB and EMDLAB can process MEG data as well. Contrary to other toolboxes dedicated to the analysis of ERPs, EMDLAB is used to analyze the characteristic of ERPs based on the extracted modes.

Brain source imaging

During the last decades, functional imaging techniques like fMRI and Positron emission tomography (PET) dominated in neuroscientific research. Concomitantly, the importance of the technically much simpler, but less straightforward to analyze, EEG declined to some degree. Still, EEG plays an important role thanks to its high temporal resolution in the millisecond range and its direct access to neuronal activation rather than measuring it indirectly via the Blood Oxygenation Level Dependent (BOLD) effect as in fMRI. Brain source imaging and reconstruction from continuous and single-trial EEG/MEG data thus have received increased attention to improve our understanding of rapidly changing brain dynamics, and using this information for improved real-time brain monitoring, brain computer interfacing (BCI), and neurofeedback [25]. Recently, several new beamformers have been introduced for reconstruction and localization of neural sources from EEG and MEG. Beamformers provide a versatile form of spatial filtering suitable for processing data from an array of sensors [195].
Thus EEG provides dynamic information on submillisecond time scales which can be combined favorably with fMRI measurements which provide complementary high resolution information on small spatial scales in the millimeter range [7][10][213][8][4]. EEG reflects voltages generated mostly by excitatory postsynaptic potentials (EPSPs) from apical dendrites of massively synchronized neocortical pyramidal cells. Ionic current inflow at den-

dritic synapses and ionic outflow at the soma induce current dipoles at the pyramidal cells which finally cause the event-related membrane potentials (ERPs) seen in EEG recordings. Unfortunately, these source imaging techniques [225][74] face the problem of ambiguity of the underlying static electromagnetic inverse problem. That is to say, the signals measured on the scalp surface do not directly indicate the location of the active neurons in the brain. Many different source configurations can generate the same distribution of potentials and magnetic fields on the scalp [52][53]. Thus, the analysis of such EEG data is quite involved, encompassing machine learning and signal processing techniques like feature extraction [10][9] and inverse modeling [67]. For timely accounts of recent advancements and actual challenges in dynamic functional neuroimaging techniques, including electrophysiological source imaging, multimodal neuroimaging integrating fMRI with EEG/MEG, and functional connectivity imaging, see the reviews of Bin He [76] and Jatoi et al. [89]. Additionally, a systems level approach to understanding information processing in the human brain is offered by Edelman et al. [45] who advocate substantial efforts to shape the future of systems neuroengineering. Furthermore, for a recent open source toolbox, named *Brainstorm*, which offers tools to analyze MEG/EEG data, combine it with anatomical MRI data and locate underlying neuronal sources of activation, see Tadel et al. [204].
Source localization affords solving an inverse problem in EEG source analysis which is highly ill-posed due to a large p, small n problem setting [101]. Unique solutions can, however, be achieved by imposing additional constraints to the resulting optimization problem. Such constraints are often of a purely mathematical nature, but biophysically realistic constraints have been formulated as well (see for example LAURA [168])[15][32]. Source localization methods use measured scalp potentials in the microvolt range, and apply signal processing techniques to estimate current sources inside the brain which best explain the observations. The analysis first predicts scalp potentials resulting from a hypothetical current distribution inside the head - this is called the *forward problem* [77][72][132][218]. In a second step, these simulations are used in conjunction with the electrode potentials measured at a finite number of locations on the scalp to estimate the current dipole sources that fit these measurements - this is called the *inverse problem* [67][225]. Over the years, researchers have developed non-parametric (also referred to as distributed source models or source imaging) as well as parametric (also called equivalent current dipole methods or spatio-temporal dipole fit models) approaches to tackle the source localization problem [44][67]. Source localization accuracy depends on several factors like head-modeling errors [202][221], source-modeling errors and measurement noise contributions [185]. Also it has been pointed out that the scalp potential needs to be sampled with electrodes evenly and densely distributed along the scalp surface [201]. Localization accuracy increases in a non-linear fashion with the number of electrodes, and estimates indicate that probably no less than 500 electrodes would be needed for an accurate sampling of the surface potential distribution [184][126]. But it has also been pointed out recently that the absolute improvement in accuracy decreases with the number of electrodes [200]. Bayesian approaches, have been reviewed recently [21], allow to compare several models and indicate that spatial localization precision in the millimeter range can be achieved reliably. Localization accuracy increases in a non-linear fashion with the number of electrodes, and the latter need to spread

over all the scalp surface homogeneously. If electrodes are concentrated in certain scalp segments, source localization can turn awfully wrong [140]. For practical purposes, Baillet et al. [16][17] suggested a spatial accuracy of 5 $[mm]$ and a temporal accuracy of 5 $[ms]$, respectively. Among the many source localization methods available, low resolution electrical tomography (LORETA) [155] and its extensions standardized LORETA (sLORETA) [156] and exact LORETA (eLORETA) [157][159] are the most commonly employed techniques. Especially sLORETA seems to outperform other techniques in most practical situations. Hence it is considered the method of choice in this thesis.
In Chapter 5, a new method which combine an EEMD analysis with a source localization scheme, more specifically an sLORETA source estimation will be introduced in Chapter 6. The introduced approach offer the possibility to use the extracted modes as inputs into an sLORETA analysis and explore whether their underlying characteristic can help in source localization.

Thesis outline

In this thesis we concentrate on electrophysiological signatures within EEG recordings of the fMRI/EEG contour integration task. EEMD method is used to investigate neural correlates of contour integration via intrinsic modes extracted from the EEG signals, recorded while applying two visual Gabor stimulus conditions i. e. *contour true* (CT) and *non-contour true* (NCT), and studying the related electrophysiological response signals.

The organization of this thesis can be summarized as follows:

- Chapter 2: the theoretical backgrounds for the main concepts are presented in detail in this chapter. First the physiology of the human brain and their recorded electrical activity EEG will be described. Then some main concepts related to the EEG called ERPs and BCIs are detailed. The final part of this chapter will give a background about the main uses of the EEG, called source localization.

- Chapter 3: the main decomposition technique EMD used in this work for the features extraction is explained in this chapter. The latter introduces a detailed background about the EMD algorithm, its characteristic features, issues, limitation and evaluation. A the end, some common EMD extensions that are developed to overcome limitations are presented.

- Chapter 4: this chapter is devoted to a description of the dataset available and the way, data has been acquired and preprocessing. It provides also a concise summary of the perceptual learning and contour integration.

- Chapter 5: in this chapter, EEMD is applied to EEG brain data that are acquired during a contour integration task in the Institute of Experimental Psychology of the University of Regensburg, to solve the forward problem. It presents a detailed description of the EEMD analysis applied and quantifies the results obtained. Component time courses and related head topographies further illustrate these results.

- Chapter 6: here, EEMD is used for inverse modeling of the EEG data. An EEMD analysis combining with a source localization scheme, sLORETA will be used to estimate sources. Obtained results and related brain images are presented in detail.
- Chapter 7: a new toolbox called EMDLAB which is an open software environment for electrophysiological data analysis will be introduced in this chapter. The presented new toolbox provides a GUI, which helps the user to handle his data and perform signal processing tasks fitted to EMD analysis. Moreover, instructions for the use and results when applying to real data are provided.
- Chapter 8: in this final chapter, the thesis will be ended with thorough conclusions of the present work.

Chapter 2

Biomedical Background

2.1 Human Brain

The human brain is the main organ that is responsible for monitoring and controlling a large number of functions of the human body. It is the part of central nervous system which is located in the skull. This highly complex organ, together with the spinal cord and network of nerves, controls the information flow throughout the body, voluntary actions such as reading, talking, and involuntary reactions such as breathing and digestion [70]. The human brain consists of four main parts: Cerebrum (divided into two large paired cerebral hemispheres), Diencephalon (Thalamus and HypoThalamus), Cerebellum and Brain stem. The cerebrum part is the largest one which is located in the uppermost portion of the brain. It consists of four lobes: the frontal lobe, the parietal lobe, the temporal lobe, and the occipital lobe. The frontal lobe is located at the front of the brain and associated with reasoning, planning, parts of speech, movement, emotions, and problem solving. The parietal lobe is positioned above the occipital lobe and behind the frontal lobe. It is responsible for movement, orientation, recognition, perception of stimuli. The temporal lobe is the bottom middle part and located behind the temples. It is responsible for processing auditory information. The occipital lobe is the visual processing center of the brain that is located at the back of cerebrum. The various important parts of the brain can be easily located from the anatomical images shown in Figure 2.1.
The brain is made up of many cells, including neurons and glial cells. These neurons are cells that serve as the building blocks of the nervous system, transmitting electro-chemical signals to and from the brain and nervous system. There are about 100 billion neurons in the brain [99]. When these neurons are activated, local current flows are produced. This electrical activity of the brain can be recorded using electroencephalography (EEG) method.

2.2 Electroencephalography(EEG)

The first human EEG recording was obtained by the German physiologist and psychiatrist Hans Berger in 1924 in Jena. He named this recording electroencephalogram (EEG). Since then, this recording technique has been one of the most used methods to study brain ac-

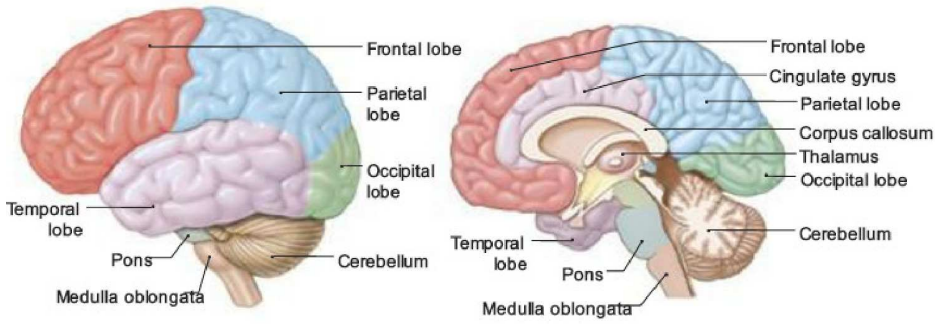

Figure 2.1 **The parts of human brain** (adapted from [199]).

tivities. Compared to other recording techniques such as functional magnetic resonance imaging (fMRI) and Positron emission tomography (PET), EEG has been largely used for multiple advantages e.g, simplicity and low cost. Electroencephalography (EEG) is the recording of the electrical activity of the brain through multiple electrodes placed on the scalp that is the top of the head where hairs grow. Recording this activity is usually taken over a small period of time, for the duration of a round half an hour only. EEG is used to diagnose different disease e.g epilepsy, comma and other disorders of brain because of injury or illness.

2.2.1 EEG Signal Recording

EEG is recorded by placing different sensors (electrodes) on the scalp of the head in special positions. The scalp area is prepared by light abrasion to reduce impedance caused by dead skin cells. These electrodes are either attached to an individual wire or in some systems embedded into caps or nets. The locations of the electrode and names are specified by the international $10-20$ system which is an internationally standard method to describe and apply the location of scalp electrodes in the context of an EEG experiment [88]. It is based on dividing the head into proportional distances from prominent skull landmarks (reference points): first, the Nasion which is the point between the forehead and the nose; second, the Inion which is the most prominent projection of the occipital bone at the posterioinferior (lower rear) part of the human skull [189]. This division provides adequate coverage of all regions of the brain. In this system, 21 electrodes are placed on the surface of the scalp as demonstrated in Figure 2.2.

Electrode placements are named by letters according the anatomical area where the electrode corresponds: prefrontal or frontopolar (Fp), frontal (F), central (C), temporal (T), posterior (P), occipital (O) and auricular (A). The letters are accompanied by either a number ,indicating lateral placement, or the letter z indicating zero or midline placement. Electrodes with odd numbers are specified at the left side of the head while even numbers correspond to the right side. The 10 and 20 refer to the actual distances between electrodes when measured from Nasion to Inion [57]. The standard set-up of $10-20$ system included only 19

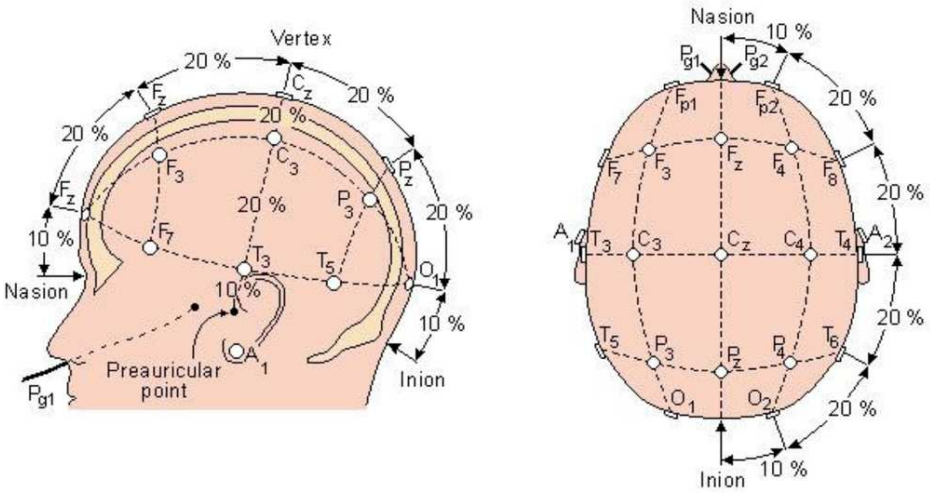

Figure 2.2 **The international 10-20 electrodes placement system** [131].

electrodes. Later on, additional electrodes can be added to increase the spatial resolution for a particular area of the brain.
The EEG signals recorded from the scalp electrodes are amplified by connecting each electrode to one input of an amplifier. These amplifiers amplify the difference between the active electrode and the reference which reduce the outside interference and artifacts because they amplify just the potential difference between two electrodes distorted by the same artifact. During EEG recording, unwanted signals which have created artifacts could happened due to noise. These artifacts are not related to brain activity rather affecting the signal measurement making it difficult for analysis. There are different types of artifacts such as environmental artifacts which are generated from outside the body, e.g the impedance of an electrode. Another type of artifacts which are useful- biological artifacts such as electrooculography (EOG) and electrocardiography (ECG) can help to predict different mental states and provide information. EOG is used to measure eye movements while ECG is used to record the electrical activity of the heart [22].
The placement of the electrodes and the connection between them is referred to as a montage. EEG signals can be recorded using either a bipolar montage or a referential one. In bipolar montage, each channel (waveform) represents the voltage difference between two adjacent electrodes, while in referential, each channel represents the difference between a certain electrode and a specified reference electrode [3].

2.2.2 EEG Usage

The EEG measurements are commonly used in two main areas:

- Medical area: one of the most important EEG applications is to evaluate several types of brain disorders. A clinical EEG recording typically lasts about $20-30$ minutes and used

to diagnose or monitor various health circumstances, including: seizures and epilepsy, brain diseases, sleep disorders, infections, confusion, head injuries, etc. [152].

- Research area: EEG is used widely in human research areas for various purposes. It is used commonly in psychophysiological and neuroscience studies, cognitive science, cognitive psychology and neurolinguistics [229].

2.2.3 EEG Brain Waves

Electrical potential recorded at the surface of the human scalp changes due to the different activities of the brain. These activities contain several periodic or rhythmic wave patterns which have been categorized into five main groups according to their frequency range (see Figure 2.3)

- Delta waves (δ) have a frequency range up to 3 Hz. They are the slowest wave of all the rhythms and the highest one in amplitude. These waves are visible in deep sleep in adults, infants and children.

- Theta waves (θ) have the frequency range from 4 Hz to 7 Hz. They are seen normally in young children. They also can be seen in adults and older children during drowsiness and sleep. These waves occur most often in sleep but also have been associated with reports of meditative and creative states. They are seen in central, temporal and parietal parts of head.

- Alpha waves (α) have the frequency range from 8 Hz to 15 Hz. They are also called Berger's waves in memory of the founder of EEG. They are most commonly seen in adults. Alpha waves are dominant during flowing thoughts and in some meditative states. They can be clearly observed in posterior and occipital regions of the head.

- Beta waves (β) have the frequency range from 16 Hz to 30 Hz. They are known as high frequency and low amplitude brain waves which are generally seen while normal waking consciousness. They are involved in thinking and active concentration. Beta waves with higher frequencies are related to high levels of arousal. They are seen in various parts of brain including primary motor, somatosensory and posterior parietal cortices in the neocortex [95]

- Gamma waves (γ) have the frequency range from 31 Hz to 100 Hz. They are the highest frequency of brain waves. Gamma waves were not studied and considered as *spare brain noise* until researchers discovered. They are involved in higher mental activity, including binding senses, cognition, information processing, learning and perception. These waves appear in each part of brain.

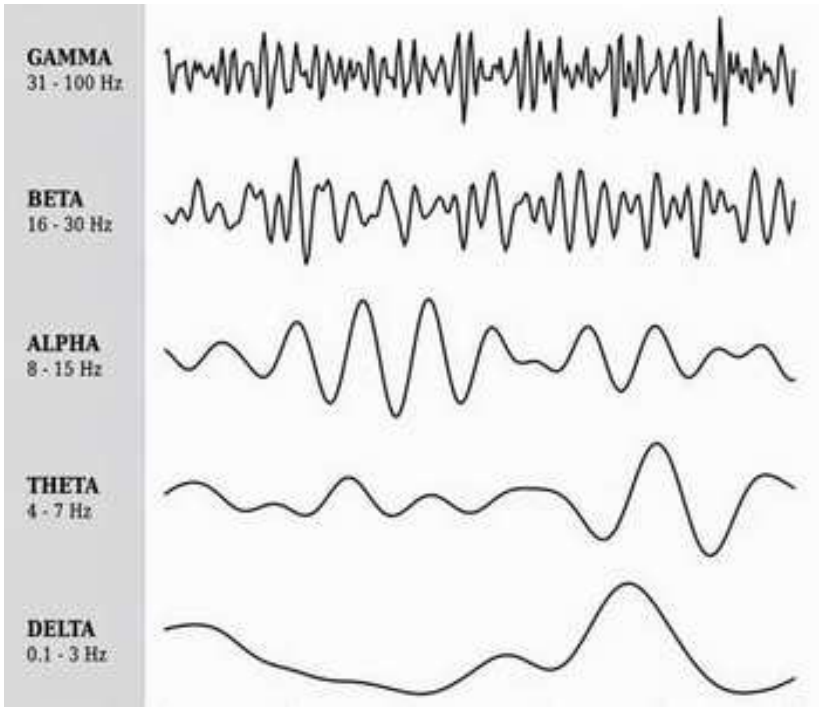

Figure 2.3 **Most common EEG waveforms** (adapted from [149]).

2.3 Event-Related Potentials (ERPs)

EEG is a useful measurement of the electrical activity within the brain. This technique is based on placing electrodes on the scalp, amplifying the signal, and plotting the voltage variations of the brains activity during the session. Although EEG represents the electrical activity within the whole brain, cognitive neuroscientists are concerned with specific neural processes. These neural responses can be extracted using averaging methods. They are known as Event-Related Potentials (ERPs) and show the summation of postsynaptic potentials between neurons [232].

2.3.1 What is ERP?

Event-related potentials (ERPs) are the measured brain responses to specific events or stimuli. ERPs can be generated by measuring the voltage changes caused in the brain during cognitive processing. They are an average of many EEG trials recordings that are time locked to specific events or stimuli [24]. ERPs consist of series of positive and negative voltage peaks that are called components [96]. These components are recognized by either the letter N or P which represents the polarity (negative/positive), followed by a number indicating the latency in milliseconds or the component's ordinal position in the waveform. For instance, the mean peak amplitudes of the ERP components $P100$ and $N100$ denoting the positive and negative components appearing 100 ms after the stimulus onset, respectively. ERPs

can be classified either according to the nature of the stimulus: visual, somato-sensory, and auditory or according to their latency: short latency ($< 100ms$) and long latency ($> 100ms$) potentials. The shorter latency components are named exogenous components and generated during the sensory stimulus processing stages while the longer latency components are called endogenous components and represent the cortical processing stages[137].
Figure 2.4 presents an example of ERP of time-locked EEG signals which are related to a visual stimulus. Figure 2.4-Left shows 3 EEG trials signals while Figure 2.4-Right depicts their averaged ERP waveform.

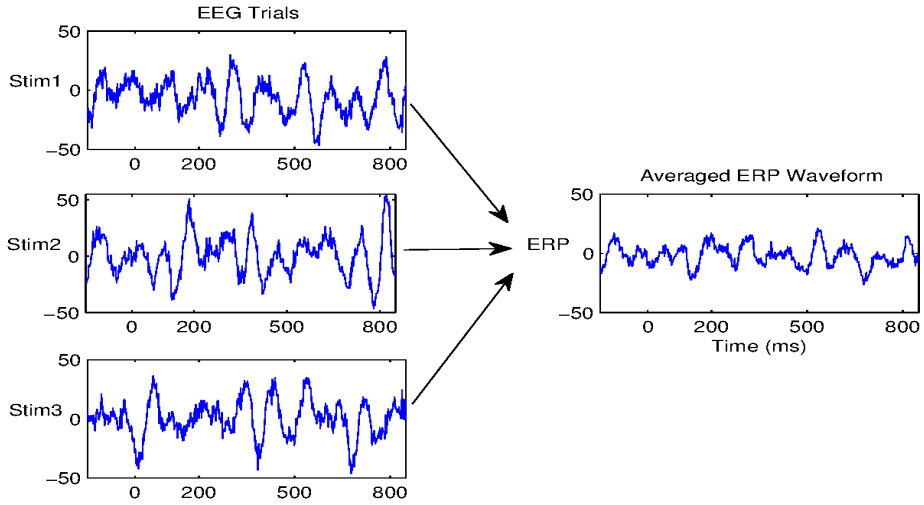

Figure 2.4 **An example of averaged ERP waveform.** *Left:* 3 different EEG time-locked waveforms elicited during a visual task. *Right:* the averaged ERP waveform across the signals in the left panel.

2.3.2 ERP Wave Properties

The ERP waveforms are described according to three parameters [93](see Figure 2.5):

- Amplitude: the maximum value of the wave from the trough (negative or positive). It represents information about the neural activity as the response to the stimulus.
- Latency: is the time delay between the stimulus presentation and its response. It represents the timing of the neural activity in milliseconds.
- Scalp Distribution: the voltage distribution over the scalp of the brain at any time point. It gives information about the activated areas of brain.

Figure 2.5 illustrates an averaged ERP waveform following a visual stimulus. It shows several ERP components: $P100$, $N200$ and $P300$ with their amplitudes and latencies. The amplitude is measured from the prestimulus baseline to the peak, and the latency is measured from stimulus onset to the peak. The related scalp topographic maps of $P100$, $N200$ and $P300$ components are illustrated at the bottom.

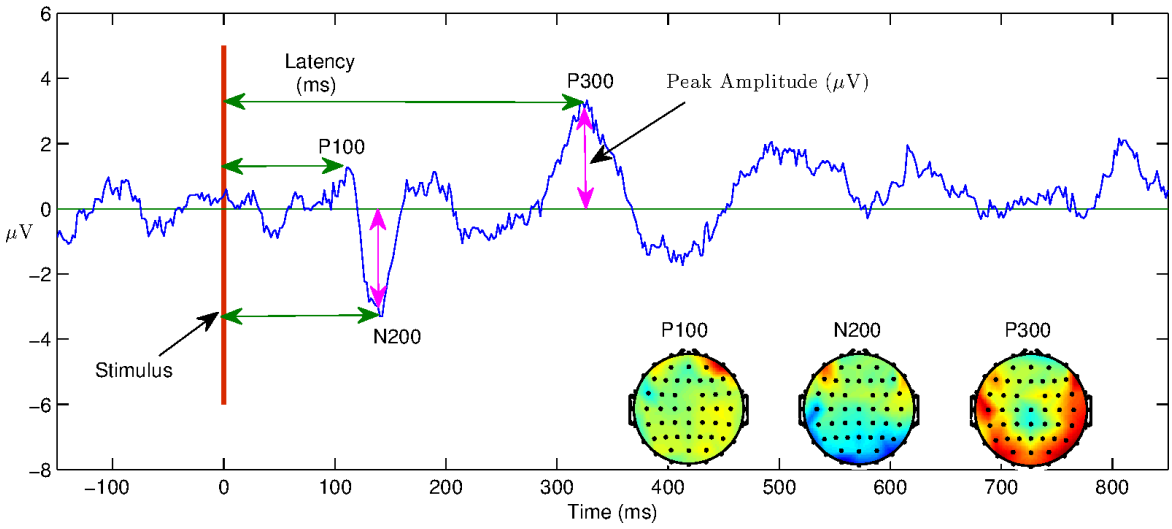

Figure 2.5 **ERP waveform with its related components:** *P*100**,** *N*200 **and** *P*300 **in response to a visual stimulus.** The amplitudes and latencies for each component are illustrated using magenta and green double arrows, respectively. The red line identifies the stimulus onset. The associated scalp current distributions of the *P*100, *N*200 and *P*300 components are depicted at the bottom.

2.3.3 ERP Advantages and Disadvantages

There are many benefits for ERP method compared to other brain response measurement. But on the other hand, there are some limitations:

- The ERP is a non-invasive method which leads to excellent temporal resolution compared to neuroimaging methods, such as fMRI and Positron Emission Tomography (PET) [121]. ERP resolves data down to milliseconds and exposes more temporal information underlying cognitive functions, where early components represent sensory processing and later components represent higher-level cognitive processes. However, the spatial resolution of the ERP is poor, where the location of ERP sources is an inverse problem that cannot be exactly solved, only estimated [232][233].
- ERPs provide a measure between stimulus and response, that allows understanding of the effects of specific experimental manipulations much better than behavioural responses. In addition, ERP can provide a measure of processing of stimuli even if there is no behavioral change [125].
- ERP experiments are more flexible compared to those in neuroimaging techniques where there are constraints on testing conditions [193].
- The ERP method is cheaper to do than other imaging techniques [39].
- As compared to neuroimaging measures, the ERP method is less sensitive to movement artifacts which makes it useful when studying infants [207].

ERPs are used widely in many research fields: neuroscience, cognitive psychology, cognitive science, and psycho-physiological.

2.4 Brain-Computer Interfaces (BCIs)

Many people have speculated that brain activity measure like EEG might one day lead to a new non-muscular path for the brain to communicate with the external world, which is essentially a brain-computer interface (BCI). Over the past few years however, the history of brain computer interface begins with Hans Berger's discovery of the electrical activity of the human brain and the development of EEG. In 1924, when Berger was able to identify oscillatory activity, he used some devices with silver wires, Lippmann capillary electrometer and others. The term BCI was first introduced by Dr. Jacques Vidal in his first peer-reviewed publications on this topic [90][91]. He is known as the inventor of BCIs in the BCI community as mentioned in several articles (e.g.,[231][11]). And later, many BCI studies from many fields, including neurology, engineering, psychology, computer sciences, etc. were done. These studies aim to a better understanding of the human brain functions via detecting and translating features of brain signals into device commands that achieve the user's target.

2.4.1 What is a BCI

BCI, also sometimes known as a brain-machine interface (BMI), is a computer-based system that allows communication and interaction between the human brain and output devices. This interface enables users to read the signals produced from different locations of the brain, analyze and convert them into required outputs that are passed to an output device, as shown in Figure 2.6. A BCI lets users to act on the world [230].

2.4.2 Principle of BCI

A BCI is mainly consists of 4 sequential steps as described by [230]:

- Signal acquisition: this is the main step for any BCI. It is the process of reading the brain signals using a specific type of sensor. These signals are amplified, digitized and transferred in preparation for later processing.
- Feature extraction: in this step, the digitized signals are analyzed to extract the pertinent signal characteristics. These characteristics have to be more relevant to the users's target. They can be extracted in the time-domain or the frequency-domain [49][43][98], or both [190]. In current BCI systems, features such as amplitude, latency and frequency power spectra are commonly used. To ensure the accuracy in selecting signal features, artifacts need to be removed such as electromyographic signals.

- Feature translation: in this stage, the extracted features from previous step are converted into device commands. These commands, in turn, will produce outputs that achieve the user's goal.
- Device output: here, the generated commands in the former step are used to operate the external device.

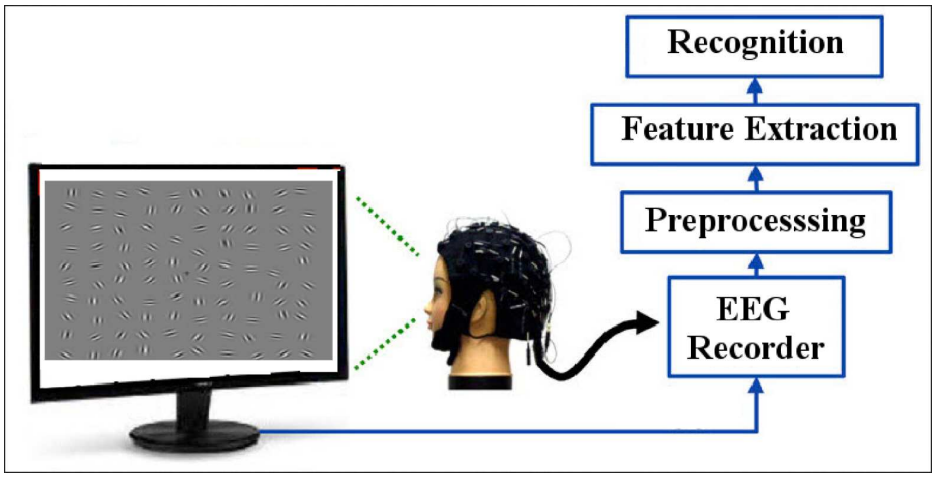

Figure 2.6 **Brain-Computer Interface scheme for Contour Task.**

2.4.3 BCI Applications

BCI is an interesting field that can help researchers to solve many problems that seem to be complicated. The main goal of BCI applications is to convert the users intent or ideas to an action in external device. Actually, the area of possible BCI applications is very wide. It can be used to complex problems as well as simple ones. Since BCI research has begun in the 1970s, It has concentrated firstly on neuroprosthetics applications that designed for substituting damaged hearing, sight and movement. Any applications of BCI focused on patients that have disorders of consciousness (DOC).These patients can not make communication with others around world [30]. One of the most common BCI application is neurofeedback (NFB) training. It is a type of biofeedback that uses brain signals mostly EEG, to improve the brain functions such as, working, attention and memorization. BCIs also are used in many applications, including spelling [117], semantic categorization [222], silent speech communication [29] and computer games, etc.
Concisely, we can say that BCIs have participated in different areas of research. They are contributor in medical, educational, neuroergonomics and smart, neuromarketing and advertisement, self-regulation, games and entertainment, and security and authentication environments.

2.5 EEG Source Localization

Neuroelectromagnetic source imaging (NSI) is the scientific field allocated to modeling and evaluating the spatiotemporal dynamics of neuronal currents throughout the brain that generate the electric potentials and magnetic fields measured with electromagnetic (EM) recording technologies [173]. Thus, over the past few decades, localizing electrical sources in the brain from surface recordings has attracted the attention of many EEG/MEG researchers. Source localization is one of the complex real world problems because of the complicated nature of the brain. It is the process of estimating the locations of activity sources inside the brain depending on the electrical recordings over the surface of the scalp. This electrical recordings reflect the activities of neurons in the brain. Activities of daily living, including motor, cognitive and sensory activities may lead to such neuronal activities. The problem lies in that a multiple of sources may lead to the same potential distribution over the surface of the head. The only way to address this problem is to construct models for the head and the underlying sources. When these suppositions are done, then the source localization is separated into a forward problem and an inverse problem. Figure 2.7 illustrates the source localization procedure which is based on the distribution of scalp amplitudes in single time point. This procedure starts with recording EEG time series signals, and then preparing these measured signals for solving the inverse problem through applying some signal processing techniques. The inverse problem tries to locate the underlying sources from recorded measurements, whereas the forward problem supposes a source definition in order to predict an electrical potential distribution map.

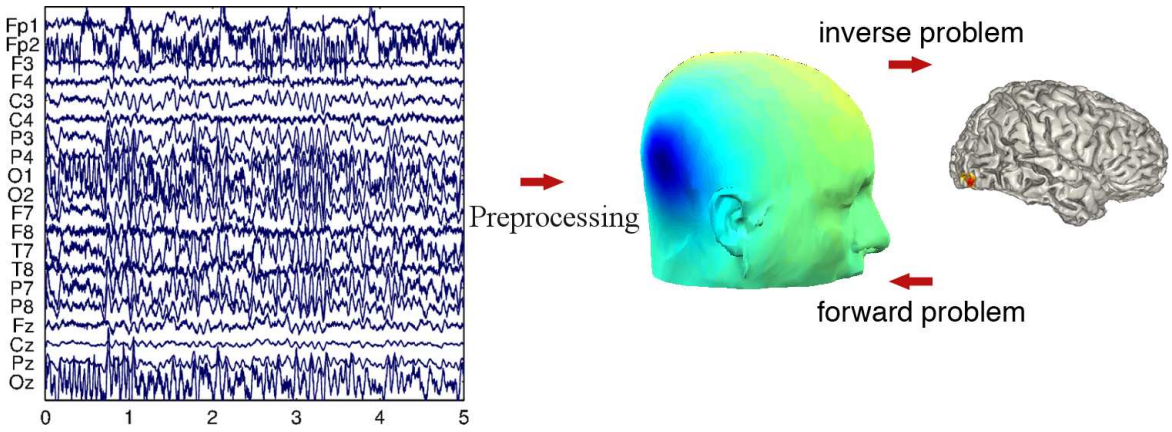

Figure 2.7 **The key parts of EEG source localization.** They start with time series recorded at the scalp sensors, passing through a preprocessing step and ending with localizing the sources (adapted from [169]).

2.5.1 Forward Problem

The EEG forward problem is the process of defining the potential distributions arising from neural sources in the head model [72]. The mathematical formulation of the forward prob-

lem is derived from Poisson's equation [130][92][71]. In the past, several studies of EEG forward mapping has mainly concentrated on multilayer spherical models, for example [23][42][243]. These studies were simple and easy to compute, so they were applied to approximate the human head. Forward solutions can be applied to compare either scalp potentials for different approaches or calculated and measured potentials [60][55] and for source imaging [64][75]. Additionally they are also required for EEG inverse solutions [144]. With forward modeling[62] [94], one is interested in predicting the expected potential distribution on the scalp, specifying position and activations of dipole current sources, and electrical conductivity of the different regions of the head. Poisson's equation can be used to relate the scalp potentials to the current density distribution inside the brain. It is developed by using the divergence operator. For further details about Poisson's equation derivation via Maxwell's equations, one can see textbooks on electromagnetism [71][131][210].

By applying the divergence operator to the vector field of the current density $K(x,y,z)$, then the divergence of K is represented as

$$\nabla.\mathbf{K} = \lim_{G\to 0} \frac{1}{G} \oint_{\partial G} \mathbf{K} d\mathbf{S} \tag{2.1}$$

where $\nabla.\mathbf{K}$ is the current source density and symbolized with I_m in [130]

$$\nabla.\mathbf{K} = I_m \tag{2.2}$$

The relation between the current density K and the electric field E is stated by Ohm's law

$$\mathbf{K} = \sigma\mathbf{E} \tag{2.3}$$

where σ is the position dependent conductivity value.

Now, the scalar potential field ϕ is presented due to Faraday's law being zero under quasi-static conditions $(\nabla * E = 0)$ [181]. A link between the potential field ϕ and the electric field E can be introduced using the gradient operator

$$\mathbf{E} = -\nabla\phi \tag{2.4}$$

The vector $-\nabla\phi$ at any point represents the direction where the scalar field ϕ most rapidly increases, and the minus sign indicates that the orientation of the electric field is from the high potential region to a low potential region.

When all the equations above are combined together, Poisson's differential equation is obtained as follows

$$\nabla.(\sigma\nabla(\phi)) = -I_m \tag{2.5}$$

This Poisson's equation can mathematically describe the EEG forward problem for electrical conduction in the head [167]. Accordingly, solving the EEG forward problem requires solving this equation. This in turn requires finding the scalp potentials ϕ. This parameter is

defined by 3 factors, the electrode position r, the dipole position r_{dip} and the dipole moment $\mathrm{d} = d e_{\mathrm{d}}$ with magnitude d and orientation e_{d}.

For one dipole and one electrode, the electrode potential can be defined as

$$\phi(r) = g(r, r_{dip}, \mathrm{d}) \tag{2.6}$$

This equation measures the potential at an electrode located at a point on the scalp with position vector l. This vector is defined by a single dipole with dipole moment e_d placed in l_{dip} inside the brain.

In case of multiple dipole sources, the electrode potential will be

$$\phi(r) = \sum_i g(r, r_{dip_i}, \mathrm{d}_i) = \sum_i g(r, r_{dip_i}, d_i e_{\mathrm{d}i}) \tag{2.7}$$

Assuming the superposition principle, Equation 2.7 can be rewritten as

$$\phi(r) = \sum_i g(r, r_{dip_i}, e_{\mathrm{d}i}) d_i \tag{2.8}$$

For N electrodes and p dipoles, the forward problem can be reformulated as

$$\begin{bmatrix} \phi(r_1) \\ \vdots \\ \phi(l_k) \end{bmatrix} = \begin{bmatrix} g(r_1, r_{dip_1}, e_{d_1}) & \dots & g(r_1, r_{dip_p}, e_{d_p}) \\ \vdots & \ddots & \vdots \\ g(r_n, l_{dip_1}, e_{d_1}) & \dots & g(r_N, r_{dip_p}, e_{d_p}) \end{bmatrix} \begin{bmatrix} d_1 \\ \vdots \\ d_p \end{bmatrix}$$

$$\phi = G(r_k, r_{dip_i}, e_{d_i}) D \tag{2.9}$$

where $k = 1, \ldots, n$ and $i = 1, \ldots, p$. ϕ is data measurements matrix, G is the gain matrix and D is the matrix of dipole magnitudes.

More generally, a noise perturbation matrix ε is added

$$\Phi = GD + \varepsilon \tag{2.10}$$

2.5.2 Inverse Problem

The inverse problem is about estimating the underlying current sources inside the brain that generated the measured electrode potentials. It is not possible to solve the inverse problem directly. Instead, iterative forward solutions for different source configurations are required. Starting from the EEG forward solution, data measured at specified positions of electrodes on the scalp, one can work back and estimate the sources that fit these measurements- the inverse problem.
Equation 2.10 presents the general model for the inverse problem. The aim of the inverse

problem then is to estimate $\hat{D}$ of the dipole magnitude matrix by giving the electrode positions and scalp readings ϕ and using the gain matrix G calculated in the forward problem.

Whereas the general forward solution is well-defined, the inverse solution is ill-posed [78] due to the non-uniqueness of the solution as $p \gg n$ in most of the imaging applications. Besides that, the accuracy of estimating the sources is affected by some factors, such as EEG noise and modeling error [228]. Consequently, EEG inverse solutions are unstable.
There are two main groups of methods which were introduced to solve the EEG inverse problem: non-parametric and parametric methods. Non-parametric methods, also referred to as distributed inverse solution (DIS), rely on a distributed source model in which the number of dipoles is unknown, but the positions and orientations are fixed. Most common examples of non-parametric methods are: Low Resolution Electromagnetic Tomography (LORETA) [160] and its derivations sLORETA(standard) and LORETA-FOCUSS (Focal underdetermined system solution) [67].
On the other hand, parametric methods, also called Concentrated Source Models (CSM) rely on a model that has a fixed number of dipoles. The most commonly used approaches of parametric methods are the non-linear least squares solver [56][211], Multiple Signal Classification [145][192], and parametric adaptations of beam forming techniques [17].
One of the most robust methods for source localization is referred to as standardized low resolution brain electromagnetic tomography (sLORETA) which was introduced by [156]. For single point sources and noiseless data, sLORETA has been shown to provide an exact source localization even for blurred images. However it was shown also that the precision with which sources can be localized strongly depends on the number, and even more so on an even distribution over the scalp surface, of electrodes from which electrical potentials are collected [219].

2.5.2.1 Standardized Low Resolution Brain Electromagnetic Tomography (sLORETA)

There are multiple methods which were introduced to solve the EEG inverse problem. These methods can be categorized into parametric and non parametric methods. The major difference between the two is whether the dipoles number is fixed in advance or not. One of the most common used non parametric methods is standardized low resolution brain electromagnetic tomography (sLORETA). It has been proposed by [156]. Based on scalp distribution of electric potentials, sLORETA was used to estimate the cortical electrical activity that could be responsible for that surface potential. It is an open source software environment that is publicly available at $http://www.uzh.ch/keyinst/loreta.htm$. It is an improvement over previously developed tomography LORETA [160]. The sLORETA method is a standardized discrete, three-dimensional (3D) distributed and linear, minimum norm inverse solution. For single point sources and noiseless data, sLORETA has been shown to provide an exact source localization even for blurred images. For further details about the description of the method, one can see [156]. The mathematical proof of its exact, zero-error localization property is explained in [157] and [158]. It is also important to mention that sLORETA has no localization bias even if there is measurement or biological noise [157]. However, there are studies [196][68] which showed that the method is not biased in the ab-

sence of measurement noise and biased in the presence of measurement noise. On the other hand, several studies have recently shown the validity of sLORETA in EEG/fMRI studies [153][142] and EEG localization for epilepsy [182].
The sLORETA computation was made in a realistic head model [62] that is based upon *MNI*152 template [136] with the three-dimensional solution space. In practical simulations, the solution was restricted to cortical gray matter, as specified by the corresponding digitized Probability Atlas [112]. The standard electrode positions of the *MNI*152 scalp were determined as in [94] and [154]. A total of 6239 voxels at 5 mm spatial resolution were created for the intracerebral volume. Thus, sLORETA images represent the electric activity at each voxel in neuroanatomic space as the exact magnitude of the estimated current density. Anatomical labels as Brodmann areas are also reported using MNI space, with correction to Talairach space [27].
The forward problem amounts to solving Poisson's equation

$$\nabla^2\phi(\mathbf{r}_k,t) = -\varepsilon^{-1}\rho_q(\mathbf{r},t) \tag{2.11}$$

for the electrical potential $\Phi(\mathbf{r}_k,t)$, registered at scalp location $\mathbf{r}_k$ at sampling time t, as function of the charge density $\rho_q(\mathbf{r},t)$ inside the brain. Biophysically, scalp potentials can be described as stemming from ionic currents in apical dendritic trees of pyramidal neurons resembling dipolar charge distributions at locations $\mathbf{r}_i$ and having dipole polarization $\mathbf{d}_i$. According to the superposition approximation, the total potential at any scalp electrode location $\mathbf{r}_k$ amounts to

$$\phi(\mathbf{r}_k,t) = \sum_i \varphi\left(\mathbf{r}_k,\mathbf{d}_i(\mathbf{r}_i,t)\right) \backsimeq \sum_i \mathbf{g}\left(\mathbf{r}_k,\mathbf{r}_i\right)\cdot\mathbf{d}_i(t) \tag{2.12}$$

where $\mathbf{g}(...)$ is called the gain or lead field which depends on dynamic electric susceptabilities inside the brain. Given N_e electrodes, N_v dipoles and T discrete time samples, the measured scalp potentials at all N_e electrode locations at times $t_1,\ldots,t_T$ can be collected into an $N_e \times T$ - dimensional data matrix $\Phi(t)$ which is estimated via

$$\mathbf{O}_c\Phi(t) = \mathbf{O}_c\mathbf{G}(\mathbf{r}_j,\mathbf{r}_i)\mathbf{D}(\mathbf{r}_i,t) + \mathbf{E}_n(t) \tag{2.13}$$

Note that all EEG signal-related quantities, i. e. $\Phi,\mathbf{G}$, are conveniently re-referenced to an average EEG signal by applying the $N_e \times N_e$ - dimensional centering operator $\mathbf{O}_c = \mathbf{I} - \mathbf{1}\mathbf{1}^T(\mathbf{1}^T\mathbf{1})^{-1}$ which obeys the relation $\mathbf{O}_c\mathbf{1} = \mathbf{0}$. Note that source localization does not depend on the choice of the reference electrode, as long as the reference is correctly integrated into the model [140]. Further, $\mathbf{G}$ represents the $N_e \times N_v$ - dimensional gain or lead field matrix, $\mathbf{D}(\mathbf{r}_i,t)$ the $N_v \times T$ - dimensional matrix of current dipole moments $\mathbf{d}_i(t_n) \equiv \mathbf{d}(\mathbf{r}_i,t_n) = (d_{x,i}(t_n),d_{y,i}(t_n),d_{z,i}(t_n))^T$ at a finite set $\mathscr{I} = \{i|1,\ldots,N_v\}$ of grid points $\mathbf{r}_i$ and a finite set of discrete time points $t = t_1,\ldots,t_T$, and $\mathbf{E}_n$ denotes additive noise. The N_v grid points are located in cortical gray matter and the hyppocampus. While the gain matrix $\mathbf{G}$ is estimated via solving the forward problem [188][62][72], the inverse problem tries to deduce the dipole matrix $\mathbf{D}$ from electrical potentials Φ measured at electrode locations $\mathbf{r}_k$ at any discrete time t_n. Non-parametric optimization methods solve the inverse

problem by estimating the dipole matrix $\mathbf{D}^*$ which maximizes the posterior probability distribution $p(\mathbf{D}|\Phi)$ of current dipole sources $\mathbf{d}_i(t_n)$ given the observations $\Phi(\mathbf{r}_k, t_n)$. Assuming a Gaussian posterior density, the corresponding log-posterior density is related to an energy functional $F_\alpha(\mathbf{d}) = \mathbf{R}(\mathbf{d}) - \alpha\mathbf{L}(\mathbf{d})$, which consists of the data log-likelihood representing a reconstruction error $\mathbf{R} = \| \Phi - \mathbf{GD} \|^2$ and a log-prior which constitutes a regularization term [205]. In case of sLORETA, the latter is, in the spirit of Tikhonov regularization, taken as $\mathbf{L}(\mathbf{D}) = \| \mathbf{D} \|^2$ yielding a minimum norm least squares estimate

$$\mathbf{D}_{MNE} = \mathbf{G}\left(\mathbf{G}\mathbf{G}^T + \alpha\mathbf{O}_c\right)^\dagger \Phi. \tag{2.14}$$

The latter becomes standardized by the square root of its $N_v \times N_v$ - dimensional co-variance matrix $\Sigma_D = \mathbf{G}^T\left(\mathbf{G}\mathbf{G}^T + \alpha\mathbf{O}_c\right)^\dagger \mathbf{G}$. Thus, at any given time point t, the (3×1) - dimensional vector of the estimated standardized dipole moment $\tilde{\mathbf{d}}$ at voxel location $\mathbf{r}_i$ is obtained as [159][220]

$$\mathbf{d}_{MNE,i}(t) \equiv \mathbf{d}_{MNE}(\mathbf{r}_i, t) = [\Sigma_D]_{ii}^{-1/2}\,\mathbf{d}(\mathbf{r}_i, t) \tag{2.15}$$

Finally the sLORETA brain maps result from computing estimates of the equivalent standardized current dipole energy at all grid points $\mathbf{r}_i . i = 1, \ldots, N_v$

$$E_{dip}(\mathbf{r}_i) \backsimeq \mathbf{d}_{MNE,i}^T \left([\Sigma_D]_{ii}\right)^{-1} \mathbf{d}_{MNE,i} \tag{2.16}$$

where $\mathbf{d}_{MNE,i}$ is the minimum norm current dipole moment estimate at the i-th voxel and $[\Sigma_D]_{ii}$ is the (3×3) - dimenional i-th diagonal block of the co-variance matrix Σ_D [156][67] [159].

Note that because pyramidal neurons span all cortical layers, the model is often simplified by assuming that, at each grid point, the direction of the ionic currents inside the apical dendritic trees, and thus the equivalent dipole moment orientation, is orthogonal to the surface. Then only its amplitude needs to be estimated. In that case, the matrix $\mathbf{D}$ has dimension $N_v \times 1$ and each i - th element corresponds to the amplitude of the i - th voxel, and the dimension of the gain matrix, as well as $\Sigma_{\hat{\mathbf{D}}}$, also changes to $N_e \times N_v$.

Chapter 3

Empirical Mode Decomposition (EMD)

3.1 Motivation

Data analysis plays a big role in pure different researches and applications. Basically, it is a process of transforming data using analytical and logical techniques for purposes of obtaining constructive information. In the real world, there are many types of signals which contain a lot of information that people are interested in. The structures of these types extend from simple to complex ones. The first natural classifying of all signals is into either stationary or non-stationary categories. Analyzing stationary signals is an easy process compared to non-stationary ones. But most of real world signals are non-linear and non-stationary. This leads us to the need of breaking the process down into individual components and analyzing each one separately, this breaking process is called decomposition. There are a number of time frequency (TF) representation methods of time domain signals such as Fourier Transform (FT), Wavelet transform, etc. The Fourier transform is based on decomposing the process into harmonic functions with fixed frequencies and amplitudes. Although the Fourier transform is widely used, but there are some critical restrictions: the system must be linear and the data must be strictly periodic or stationary. Otherwise the resulting spectrum could not reflect the interesting characteristic of the system behavior. On the other hand, Wavelet transform is used to avoid constraints associated with non-stationarity system. Contrary to FT, it decomposes the process into a fixed basis of time and frequency functions. However, it characterizes the scale of a signal event using pre-specified basis functions. In practical applications, it would be good to have an adaptive decomposition that could overcome the limitations of above described methods. Recently, an empirical nonlinear analysis tool for complex, non-stationary temporal signal variations has been pioneered by N. E. Huang *et al.* [80]. Such technique is commonly referred to as Empirical Mode Decomposition (EMD), and, if combined with Hilbert spectral analysis, it is called Hilbert-Huang Transform (HHT). EMD utilizes empirical knowledge of oscillations intrinsic to a time series in order to represent them as a superposition of components with well defined instantaneous frequencies. They adaptively and locally decompose any non-stationary signal into many modes with different frequency characteristics, called Intrinsic Mode Functions (IMF). These IMFs represent zero-mean, amplitude- and (spatial-)

frequency-modulated components. EMD is a fully data-driven, unsupervised method. It is based on an adaptive basis system. EMD also satisfies the completeness property, i.e. original signal can be reconstructed by superimposing all extracted IMFs together with the residual without information loss or distortion.
This chapter explains the theory behind Empirical Mode Decomposition (EMD). It covers a detailed explanation on how the EMD has been implemented. EMD extensions, instantaneous frequency estimation, other properties and issues are also discussed.

3.2 EMD Algorithm

Empirical mode decomposition (EMD) is a purely data-driven analysis tool for complex non-linear and non-stationary time series. It adaptively and locally decomposes any non-linear and non-stationary time series into oscillations on various frequency scales. These resulting oscillatory modes are called intrinsic mode functions (IMFs) that represent zero-mean amplitude and frequency modulated components. EMD is intuitive, direct, a posteriori and adaptive, with the basis of the decomposition based on, and derived from, the data. The essence of the decomposition is based on identifying the intrinsic oscillatory modes empirically by their characteristic time scales in the data. Extracting the IMFs is an iterative process that relies on subtracting the highest oscillation components from the original data with step by step process, which is called the *sifting process*.

3.2.1 Intrinsic Mode Function (IMF)

The principle of EMD method is to decompose any signal $x(t)$ into a set of a mono-component functions called Intrinsic Mode Functions (IMFs) which are zero-mean, amplitude- and (spatial-) frequency-modulated components. The monocomponent function refers to an oscillation similar to common harmonic functions. Therefore, the IMFs represent the signal as amplitude and frequency modulated (AM-FM) signals which are arranged in order of highest frequency to lowest frequency components. The AM carries the envelope and the FM is the constant amplitude variation in frequency and computed using a sifting process. To achieve this, an IMF must satisfy two conditions:

- In the whole dataset the number of maxima and minima can at most differ by one.
- At any point the local mean $m(t)$ of the upper envelope and lower envelope should be close to zero.

Note that achieving the second condition leads to consider the IMF as wide sense stationary signal which simplifies its analysis. Nevertheless, an IMF could have modulated amplitude and frequency as presented in Figure 3.1.
The first condition results to a narrow-band signal, and it is necessary to ensure achieving the conditions needed to calculate the instantaneous frequency [80][84]. The second condition is a local requirement caused by the global one which requires symmetric upper and lower envelopes of an IMF that makes the signal ready for modulation [80][79][83]. It is not easy to find the envelopes because of the nonlinear and non-stationary nature of the data.

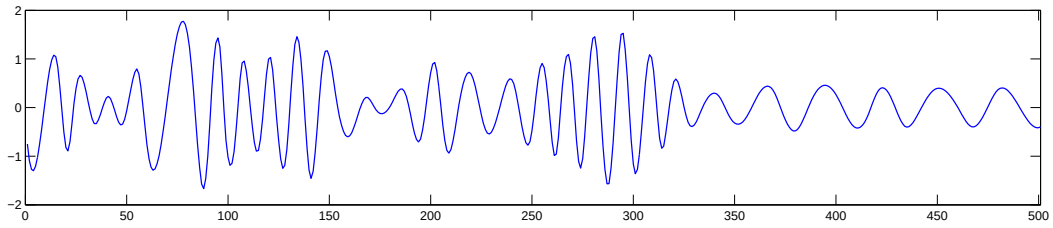

Figure 3.1 **An example of Intrinsic Mode Function (IMF).**

3.2.2 Sifting Process

Although the mathematical proof of EMD has not been developed yet, there are methods for extracting the IMFs which has been introduced by [80]. Finding the IMFs is an iterative process that relies on subtracting the highest oscillation components from the original data in a step by step process, which is called the *sifting process*. It is the core of the EMD algorithm that is applied to iteratively filter the different oscillatory components of the signal, starting with the fastest and ending with the slowest component. Hence, the sifting algorithm decomposes a data set $x(t)$ into $j = 1,...,J$ individual IMFs symbolized by $c^j(t)$ and $r(t)$, the residuum which is the remaining non-oscillating trend of the data.

The sifting process can be summarized in the following steps:

1. Identify the extrema (both maxima and minima) of the registered signal $x(t)$.
2. Construct the upper and lower envelopes $env_{max}(t)$ and $env_{min}(t)$ using a cubic spline interpolation scheme.
3. Calculate the mean of the two envelopes as $m(t) = \frac{[env_{max}(t)+env_{min}(t)]}{2}$
4. Subtract the mean value from the signal $h(t) = x(t) - m(t)$
5. Determine whether $h(t)$ is an IMF or not by checking the two conditions as described above.
6. If $h(t)$ is IMF, set $c^j(t) = h(t)$ and find the $j+1$ - st IMF after updating $r(t) = x(t) - \sum_{j<(j+1)} c^j(t)$. Otherwise, update $x(t) = h(t)$ and repeat steps 1 to 5.

where $r(t)$ is an intermediate signal, initially created with a copy of the original time series $r(t) = x(t)$. The sifting process is straightforwardly illustrated in Figure 3.2.
IMF represents the oscillation mode of signal and because of that it was called intrinsic mode function. Accordingly, the IMF involves only one mode of oscillation, no complex waves are allowed. At the end of the decomposition, the original signal can be represented by an expansion into its underlying modes plus a non-oscillating residuum

$$x(t) = \sum_{j=1}^{J} c^j(t) + r(t) \tag{3.1}$$

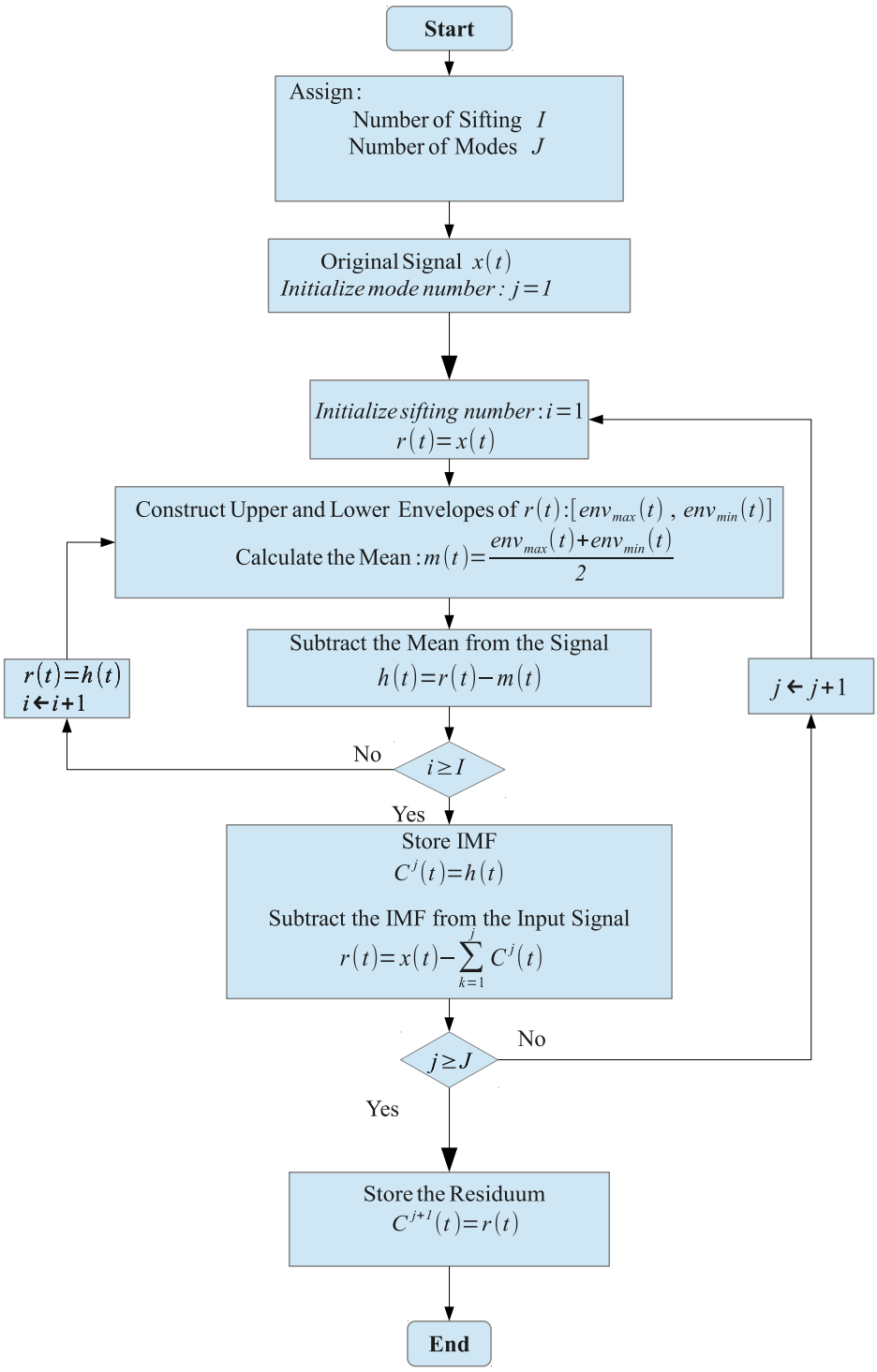

Figure 3.2 **Flowchart diagram of EMD algorithm.**

The sifting procedure will be repeated until all IMFs have been extracted. Figure 3.3 illustrates the complete process of EMD for an example of toy data signal *sig* which consists of two sinusoid components

- $x_1(t_n) = 3sin(20\pi.t_n)$
- $x_2(t_n) = 6sin(60\pi.t_n)$

with $t_n = 0, ..., 1$, a step of $\Delta t_n = 0.0001$ between the samples and a total of $N = 10001$ data points. These two signals are summed up to generate the signal $sig(t_n) = x_1(t_n) + x_2(t_n)$ (Figure 3.3-Top). Figure 3.3 clearly describes how EMD could extract the two IMFs (second and third rows) of the original signal *sig* (first row). The last row shows the trend of the signal.

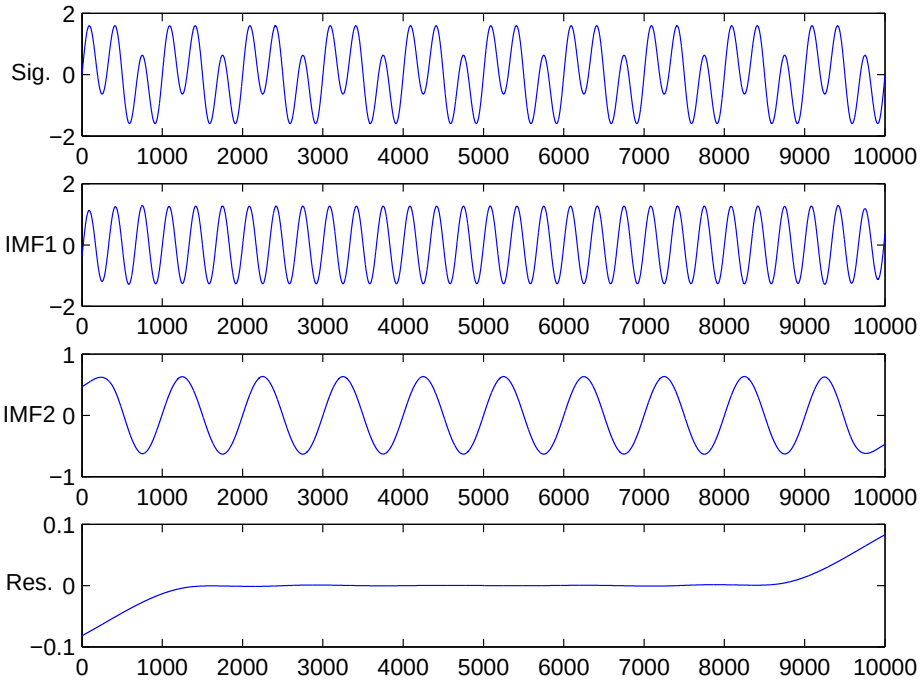

Figure 3.3 **EMD decomposition of a toy data signal.** *Top raw:* toy data signal which consists of two different frequencies sinusoid signals, $x_1(t_n) = 3sin(20\pi t_n)$ (second row) and $x_2(t_n) = 6sin(60\pi t_n)$ (third row). The last row illustrates the monotonic trend of the signal.

3.3 Hilbert-Huang Transform

In the periodic signals, the frequency is defined as the number of occurrences of a repeating event per unit time. It is constant for signals that are completely sinusoidal. But, most signals in the real world are not completely sinusoids. For example a linear chirp signal is a non stationary signal where its frequency increases linearly over time. This has led to the concept of the Instantaneous Frequency (IF) where the changes in the frequency can be represented instantaneously over time. Hence, IF was introduced to describe the frequency

of non-stationary signals at each time point [84].
The Instantaneous Frequency can be easily calculated through the Hilbert Transform. For any time series $c^{(j)}(t_n)$, the IF $\omega(t_n)$ is defined as the derivation of the phase $\theta(t_n)$ of the analytic signal $z(t_n)$

$$\omega(t_n) = \frac{d\theta(t_n)}{dt} \tag{3.2}$$

The analytic signal $z(t_n)$ can be defined as

$$z(t_n) = c^{(j)}(t_n) + iy(t_n) = a(t_n)\exp(i\theta(t_n))$$

with instantaneous amplitude $a(t_n)$ given by

$$a(t_n) = \sqrt{(c^{(j)})^2(t_n) + y^2(t_n)} \tag{3.3}$$

and $y(t_n)$ is the Hilbert Transform of the signal $c^{(j)}(t_n)$, and can be calculated as

$$y(t_n) = \frac{1}{\pi} P\left\{\int_{-\infty}^{\infty} \frac{x(\tau)}{t_n - \tau} d\tau\right\} \tag{3.4}$$

where P indicates the Cauchy principle value of the integral.
However, in some situations calculating IF using this way will give a negative value that has no meaning in the real word. In other words, IF define the variation of the frequencies over the time. That means, it may be represented as the frequency of Sine wave that locally suits the signal under analysis. Therefore, the Instantaneous Frequency is meaningful only for mono-component signals, where there is only one frequency or a narrow band of frequencies varying over time [80][194]. In principle, it is difficult to represent the IF of multicomponent signals, thus a separation into components is required. So, to apply the concept of IF to any signal, EMD can be used as a separation method that decomposes a signal into series of mono-components IMFs. Then the derivation of IF for each IMF can give meaningful physical information. Using the EMD method to decompose signals to IMFs followed by applying Hilbert spectral analysis to each IMF to obtain IF is called Hilbert-Huang transform (HHT).
After performing the Hilbert-Huang transform, each IMF can be represented as

$$c^{(j)}(t_n) = Re\left\{a_j(t_n)\exp\left(i\int_{-\infty}^{t_n} \omega_j(t_n)dt\right)\right\} \tag{3.5}$$

and the original signal $x(t_n)$ can be written as

$$x(t_n) = Re\left\{\sum_j a_j(t_n)\exp\left(i\int_{-\infty}^{t_n} \omega_j(t_n)dt\right)\right\} + r(t_n) \tag{3.6}$$

Figure 3.4 displays a linear chirp signal that increases in frequency over time (upper plot). This signal is generated using a frequency range from $1-10Hz$, a duration of $5ms$. The

lower plot shows the related Hilbert spectra for the signal which presents the instantaneous frequencies.

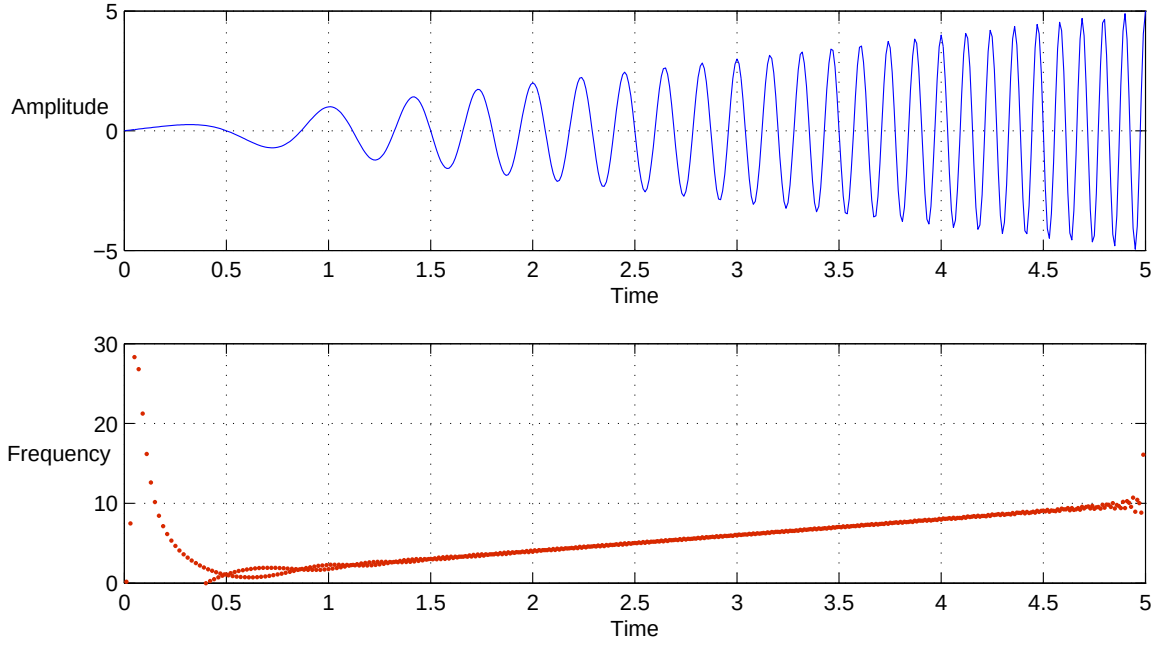

Figure 3.4 **Hilbert spectra of a linear chirp waveform.** *Top:* a linear chirp cosine wave that increases in frequency linearly over time. *Bottom:* the related Hilbert spectra for the signal at the top.

3.4 Some Issues with Applying EMD

A main feature of the EMD algorithm is its simplicity of application and robustness across a wide range of data processing methods. However, a number of issues come up which need further consideration for successful application of EMD. The decomposition is based on these critical issues which have to be managed by the user. This makes the uniqueness of decomposition not guaranteed. Among these issues are stopping criteria, envelope construction and boundary adjustment. In the following section, an overview of these issues is introduced.

3.4.1 Envelopes Estimation

The method of estimating the envelopes is crucial to the success of the EMD algorithm. It is based on first identifying all extrema (maxima and minima). Once these extrema are identified, all the maxima are connected by a cubic spline line as the upper envelope $env_{max}(t_n)$. The procedure is repeated for the local minima to generate the lower envelope $env_{min}(t_n)$.

All the sample points should now be covered by the upper and lower envelopes. The mean of the two envelopes $m(t_n)$ is computed as follows

$$m(t_n) = \frac{\left(env_{max}(t_n) + (env_{min}(t_n)\right)}{2} \tag{3.7}$$

which should represent the pointwise local extreme mean of the signal as accurate as possible. The envelopes are required to estimate the local mean at each sample point. In addition to that, it is necessary to precisely localize all extrema (maxima and minima). There are several interpolation methods used to create the envelopes. Most widely used is the spline interpolation. Splines are piecewise polynomial functions of degree l. The pieces connected in the so called *knots* with certain continuity conditions for the function itself and its first $l-1$ derivatives. Cubic splines are most commonly used to interpolate local maxima and local minima. The basic idea of the cubic spline is that the function is represented by a different cubic polynomial on each interval between data points. This piecewise cubic function has continuous first and second derivatives at the *knots*. Cubic spline is a fast, efficient and stable method used for interpolation. Furthermore, it gives good results compared to other types of interpolation but on the other side, its computational cost is high.
Figure 3.5 shows an example of an IMF, where the blue curve represents the actual IMF, the green line its upper envelope, the red line its lower envelope, red and cyan stars illustrate the local maxima and minima, respectively, and the black line represents the mean of the envelopes. In this case, the IMF has 26 zero crossing and 29 local extrema, and the symmetry of the two envelopes leads to mean value that is close to zero.

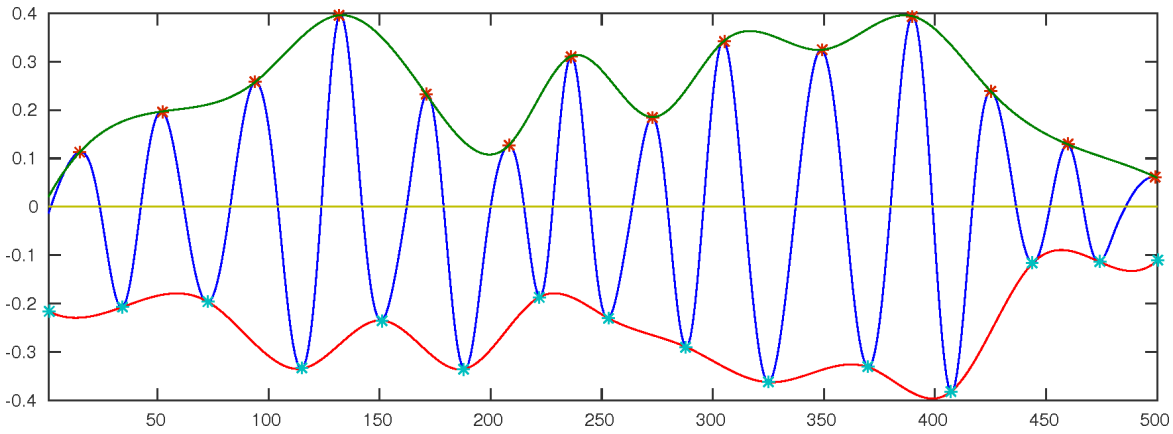

Figure 3.5 **An example of IMF with corresponding envelopes.** The blue curve represents the input signal, green and red lines are the upper $env_{max}(t_n)$ and lower $env_{min}(t_n)$ envelopes, respectively, represented by cubic spline interpolation. Red and cyan stars represent the local maxima and minima, respectively, and the black line is the mean envelope $m(t_n)$.

In the standard EMD algorithm [80], a cubic spline interpolation method is used to estimate the envelopes. Several alternative interpolation methods have been introduced to improve the performance of the EMD algorithm. For example, tau [80] and rational [164] splines

have been used as interpolation technique which is based on an extra parameter and offers transmitting between a linear and a cubic spline smoothly. Although these studies show lower covariance terms (more orthogonal) of the resultant IMFs and residual relative to the cubic spline, they increased the number of IMFs and the number of sifting iterations required to generate the IMFs. Rilling *et.al* [178] tried to use linear or polynomial splines, but they result to a large number of sifting iterations and to *over-decomposition* of signals. Also, B-splines were tried and gave similar results as cubic splines, but they increase the number of IMFs. Furthermore, optimizing the quadratic cost functions was used to estimate the envelopes in [224], but it shows low improvement in relation to the large cost. Accordingly, cubic splines were to be preferred to linear or polynomial interpolation. Further methodology is proposed in [102][103] based on optimizing the interpolation points *IP* (maxima and minima) to the ones with the highest frequency and interpolating them using Hermit interpolation. Recently, new approaches were proposed to generate the local mean of the signal directly without the need to use envelopes [113][139]. The obtained results were similar to the ones obtained by the standard algorithm, but the method requires further research and development. In this thesis, the cubic spline interpolation is used for the EMD algorithm applied to all decompositions.

3.4.2 Stopping Criteria

In EMD, the stopping criteria determine the required number of sifting steps to produce an IMF. In other words, they decide when the sifting process should stop. Stopping criteria have a direct influence on the result, since they play an important role for the successful implementation of the EMD. As described in EMD methodology, the sifting process has to be repeated as long as there exist local segments with means not yet close to zero. Accordingly, the more times the sifting is iterated, the closer the mean will be to zero. Although that is good to eliminate the riding waves and force a local zero, but it leads to over-sifting and tends to split physical meaningful IMFs into meaningless fragments. Based on the above, the stopping criteria must be chosen carefully to avoid over iterating.
The most common stopping criteria are:

Cauchy-like Convergence Criterion

This criterion was used when an EMD algorithm has been introduced in [80]. The sifting process is performed until the sifted result is smaller than a predetermined limit θ. If two components from consecutive iterations are close enough to each other, it is assumed that the last extracted component is an IMF. It is based on calculating the standard deviation of two successive sifting results

$$\sigma_{i,j} = \sqrt{\sum_{n=0}^{N} \frac{\left(h_{i,j-1}(t_n) - h_{i,j}(t_n)\right)^2}{h_{i,j-1}^2(t_n)}} \tag{3.8}$$

where $\sigma_{i,j}$ is the difference between two successive results $h_{i(j-1)}$ and $h_{i,j}$ The first IMF is extracted whenever $\sigma_{i,j}$ is smaller than the appropriate predefined value θ. Usually the

typical value of σ is between 0.2 and 0.3. Using a predetermined threshold is to compel the envelope mean signal being closer to zero which will ensure the symmetry of the two envelopes between the number of zero crossings and number of extremes. This threshold should be small in order to allow separating all the oscillations. But on the other hand, it should be also large enough to avoid losing the meaningful components. However, a smaller threshold could lead to over-sifting and mixing of IMF modes, and a larger threshold could lead to an early termination of the sifting process [80]. This Cauchy-like convergence criterion, however, is often not a trustworthy stopping criterion because it does not test or check the two IMF conditions, and can be satisfied without achieving the latter.

Evaluation Function Criterion

In 2003, Rilling *et al.* [178] proposed an alternative stopping criterion which uses two thresholds δ_1 and δ_2. The first threshold δ_1 is defined to guarantee globally fluctuations in the mean of the cubic splines, while the second δ_2 allowing small regions of locally large excursions. Besides the original mean $m(t_n) = (env_{max}(t_n) + env_{min}(t_n))/2$, it is based on introducing the mode amplitude $a(t_n)$ and the evaluation function $\sigma(t_n)$

$$a(t_n) = \left(\frac{env_{max}(t_n) - env_{min}(t_n)}{2} \right) \tag{3.9}$$

$$\sigma(t_n) = \left| \left(\frac{m(t_n)}{a(t_n)} \right) \right| \tag{3.10}$$

where $env_{max}(t_n)$ and $env_{min}(t)(t_n)$ are the upper and lower envelopes respectively. The sifting process is stopped when $\sigma < \delta_1$ for a setting fraction $(1-\alpha)$ of the total duration, and $\sigma < \delta_2$ for the remaining fraction. Typical values of those thresholds are $\alpha \approx 0.05$, $\delta_1 \approx 0.05$ and $\delta_2 \approx 10\delta_1$ [178]. However, Rilling's method introduces three new parameters that have to be fixed which might have an affect on the resulting IMFs.

Fixing the Number of Sifting Iteration

This criterion that was proposed by [81][85] is based on predetermining the number of sifting iteration I. The sifting process is stopped when the number of zero crossings and the extrema is the same number for I sequential sifting steps. Wu and Huang in [235] found that about 5 iterations are enough to achieve the stopping criterion proposed by Huang *et al.* in [80].
In this thesis, the latter stopping criterion of EMD algorithm is used.

3.4.3 Boundary Adjustment

In the EMD algorithm, interpolating extremes is achieved using splines to construct the upper and lower envelopes. However, using the spline interpolation induces overshoots

and undershoots. Accordingly, the resulting IMF does not accurately ensure symmetric envelopes [80]. These problems occur when the end points are not extrema which causes the spline to oscillate widely. Furthermore, and because of the sifting iterations, these effects could propagate inwards and progressively corrupt the low frequency IMFs. The first procedure to deal with the problem proposed by [80] and modified by [37] is to pad the signal in the beginning and at the end with typical waves. These waves are based on the two closest maxima and minima [80], while in [37], it is based on the closest maximum and minimum. A simple technique introduced by [178] is to *mirror* the extreme closest to the data edge, rather than padding with extra data. Another alternative is using the average of the two closest maxima and minima for the maximum and minimum splines respectively [31]. In addition, Peel *et.al* [163] have presented an alternate methodology called *SZero* for handling the spline end artifacts which is based on the assumption that the slope of the cubic spline is equal to zero at the end points. For long data series, the simplest way to control the results corruption is to remove some data at each end of the signal. However, this becomes complicated when there are not enough data to remove. The standard EMD algorithm applied in this thesis handles the boundaries of the time series as described in [238]. In the beginning, the first sample point of the data is defined as first maximum and minimum $m_1 = t_1$. Then the slope between the second $(m_2|x_{m2})$ and third $(m_3|x_{m3})$ maximum is estimated

$$\delta_{23} = \frac{x_{m2} - x_{m3}}{m_2 - m_3} = \frac{\triangle x_{m23}}{\triangle m_{23}} \tag{3.11}$$

During estimating the slope, a straight line is built crossing the second and third maximum. After that, the intersection point $\delta_{23}(m_1 - m_2) + x_{m2}$ between the straight line and vertical line is calculated

$$x_{m_1} = max[\delta_{23}(m_1 - m_2) + x_{m2}, x(m_1)] \tag{3.12}$$

This value x_{m_1} will be defined as the new first maximum $(m_1|x_{m1})$, if it is larger than the x-value of the first sample $x(m_1)$. The same procedure is done for the minima at the beginning and the extreme at the end of the time series data.

3.4.4 Data Requirements

There are some demands related to the data which should be taken into account to ensure a satisfactory signal decomposition. One of these requirements is the sampling rate of the time series. EMD results depend highly on sampling conditions [203][174]. Since the EMD algorithm operates practically on discrete-time signals, a special attention has to be paid to the fact that extrema has to be correctly detected which requires a fair amount of oversampling.

The Nyquist sampling theorem must be followed to provide a sufficient condition for the sampling of the signal. Also, the number of extrema in a digitalized signal and its continuous version should be equal. Furthermore, at least 5 samples per period are required to obtain good results from the Hilbert transform [80]. Further details about the influence of different sampling rates on the decomposition outcomes are provided in [174][176]. An-

other key point which plays an important role in detecting the extreme is the amplitude of the signal. Since it is not possible to detect the extrema of small amplitude oscillations, the EMD method collapses to extract the components with such very small amplitude compared to the other modes contained in the signal, especially if there is additional noise. Finally, a third issue that has to be taken into account is related to the frequencies of the signal, which have only been characterized by numerical experiments, and no theory has been created yet. EMD acts as a dyadic filter bank with white noise [59][177][235] and the number of extrema will be decreased by one half from one IMF to the next. Rilling *et al.* [178][175] concluded that for a given signal frequency f_1, there is a frequency band $\mathscr{B}(f_1) = [\alpha_\rho f_1, f_1], \alpha_\rho < 1, \rho = a_1/a_2$, for each amplitude ratio ρ ,such that f_1 and $f_2 \in \mathscr{B}(f_1)$ cannot be separated. This supports an interpretation of EMD as filter bank. Using the same filter for two frequencies will lead to represent them by the same IMF.

3.5 EMD Characteristic Features

Since there is no mathematical basis behind the EMD method, its performance has been studied empirically using numerical solutions. This has enabled a clear understanding of its decomposition behavior and defined the issues with applying the method, which in turn, could help researchers to make a decision about applying the method to different types of signal. In this section, some mathematical properties of EMD which have been obtained mostly through numerical expressions are explained.

3.5.1 Completeness

One important feature of EMD is that the original signal can be reconstructed by summing up all IMFs components and the residuum. Hence, the completeness is fulfilled according to the reconstruction equation

$$x(t_n) = \sum_{j=1}^{J} c^j(t_n) + r(t_n) \tag{3.13}$$

Completeness can be evaluated numerically using this equation. The error between the reconstructed signal and original signal is estimated by subtracting sum of all extracted IMFs from the original signal

$$\varepsilon = \left(x(t_n) - \left(\sum_j c^{(j)}(t_n) + r(t_n)\right)\right)^2 / n \simeq 10^{-30} \tag{3.14}$$

In practical experiments, the order of magnitude of the reconstruction error is approximately between $10^{-15} \sim 10^{-16}$.

3.5.2 Orthogonality

The orthogonality for the decomposition method is important to ensure that the extracted components are not overlapping with each other. Mathematically, if two functions $x(t)$ and $y(t)$ satisfy

$$\int_{t1}^{t2} x(t)\, y(t)\, dt = 0, \qquad t_1 < t < t_2 \tag{3.15}$$

then $x(t)$ and $y(t)$ are orthogonal.

The orthogonality of the EMD method still is not guaranteed theoretically, however the extracted IMFs are locally orthogonal [80]. Huang *et al.* [80] tried to prove the EMD's orthogonality by investigating several decomposed data in different research areas. In the equation Equation 3.1, if $r(t_n)$ is considered as an IMF, the data decomposition can be rewritten simply as

$$x(t_n) = \sum_j c^{(j)}(t_n) + r(t_n) = \sum_j X^{(j)}(t_n) \tag{3.16}$$

The square of the signal is

$$x^2(t_n) = \sum_j \left(X^{(j)}(t_n)\right)^2 + 2\sum_j \sum_k X^{(j)}(t_n) X^{(k)}(t_n) \tag{3.17}$$

Now, the decomposition is orthogonal when the second part of the right side of the equation is equal to zero. The overall index of orthogonality IO can be defined as follows

$$IO = \sum_{t_n} \left(\sum_j \sum_k X^{(j)}(t_n) X^{(k)}(t_n) / x^2(t_n) \right) \tag{3.18}$$

According to a study of analyzing decomposed wind data by Huang *et al.* [80], the value of IO is only 0.0067. The orthogonality of two IMF components, c_i and c_j can be also defined as

$$IO_{i,j} = \sum_t \frac{c_i c_j}{c_i^2 + c_j^2} \tag{3.19}$$

It should be noted that the orthogonality mentioned here refers to local orthogonality, not global.

3.5.3 Uniqueness

The results of the EMD decompositions of a data set are the same as long as this decomposition is subject to the same conditions implementation. Changes in the EMD implementation such as stopping criterion will lead to quantitative and no qualitative change in the resulting Intrinsic Mode Functions.

3.5.4 Linearity and Stationarity

Linear systems fulfill the property of superposition [28]. Given two valid inputs: $a_1(t)$, $a_2(t)$ and their respective outputs are $y_1(t) = H\{a_1(t)\}$, $y_2(t) = H\{a_2(t)\}$, where H is the operator that maps an input, $a(t)$ as a function of t to an output, $y(t)$, then a linear system must satisfy

$$\alpha y_1(t) + \beta y_2(t) = H\{\alpha a_1(t) + \beta a_2(t)\} \tag{3.20}$$

for any scalar values α and β.
Most real world signals, like biomedical time series, are nonlinear and can approximately be re-formed as a linear system. However, EMD as a decomposition technique is able to deal with nonlinear data. Recently there have been attempts to prove the non-linearity of EMD [208].
For stationarity property, the time series $X_t, t \in Z$ (where Z is the integer set) is said to be strongly stationary if the joint probability of $(X_{t_1}, X_{t_2}, ..., X_{t_k})$ is the same as that of $(X_{t_1+\tau}, X_{t_2+\tau}, ..., X_{t_k+\tau})$ [28]

$$F_X(x_{t_1+\tau}, ..., x_{t_k+\tau}) = F_X(x_{t_1}, ..., x_{t_k}) \tag{3.21}$$

In other words, strongly stationary means that the joint probability does not depend on the time itself $(t_1, ..., t_k)$ but only on the time differences τ. A weaker form of stationarity called weak-sense stationarity, wide-sense stationarity (WSS) is used in signal processing. The time series $X(t), t \in Z$ is said to be weakly stationary if the variance is finite, i.e. $E(X(t)^2) < \infty \, \forall \, t \in Z$, the mean is constant, i.e. $E(X(t)) = \mu \, \forall \, t \in Z$, and the covariance only depends on τ, i.e. $cov(X(t_1), X(t_2)) = cov(X(t_1), X(t_1 + \tau)) = cov(X(0), X(\tau))$. Weak stationarity only requires that the first (mean) and second (variance) moment of the data distribution P(X(t)) do not vary with respect to time.
Unfortunately, in most real systems, the data are mostly to be nonstationary. The data from such a system is not easy to analyze. The main feature of EMD is that it can be used to decompose nonstationary data into a finite number of Intrinsic Mode Functions without any difficulties. These resulting IMFs used to define the local characteristics of nonstationary signal through its instantaneous frequency.

3.6 EMD Limitation

Despite of its worthwhile success in many practical applications (see for example [122][123] [234][37][223][36]), EMD still has some drawbacks. The major drawback of EMD method is the lack of theoretical framework which leads to difficulties for the characterization and evaluation of the performance of this approach. Consequently, in practice, EMD can be efficiently evaluated by simulating the decomposition process using toy data sets and investigate the effect of various parameters.
In addition to the mathematical model, EMD is an empirically based data-analysis method which means any physical meaning of the resulting IMFs can not be reliable. However, the

extracted IMFs maintain their amplitude modulation and changing frequency. As mentioned above, EMD can not guarantee uniqueness of the decomposition. The variation in choosing the optimal parameters in EMD leads to the loss of physical uniqueness of the extracted IMFs which makes it difficult to interpret their physical significance.
One of the major drawbacks of the original EMD is the repeated occurrence of so-called *mode mixing* which means a consequence of signal intermittency. Mode mixing appears when either a single IMF composed of signals of widely different scales, or different IMFs contain a signal of a similar scale. The intermittency of signal causes aliasing in the time-frequency distribution, and furthermore, it makes the individual IMF losing of physical meaning [80][81]. Figure 3.6 shows an example which illustrates how mode mixing problem occurs when EMD is applied. The signal used in the example is composed of the sum of two signals $sig = Comp1 + Comp2$ (see Figure 3.6-Left).

- $Comp1 = 0.1sin(2\pi t_n + 5sin(\pi t/100))(exp(-(t_n - 25)^2/10))$
- $Comp2 = sin(0.1\pi t_n)$

$Comp1$ is high frequency intermittent oscillations, whereas $Comp2$ is a simple sinusoidal signal with a larger scale. Figure 3.6-Right shows the final decomposition of the signal into IMFs and a residual (Res). As can be shown, there are still some oscillations of small scale mixed with large scale in $IMF1$. In addition, oscillations of large scale also exist in both $IMF1$ and $IMF2$. To alleviate this problem, a new noise-assisted data analysis (NADA) method is proposed by Wu *et al.* [236], called Ensemble Empirical Mode Decomposition.

3.7 Evaluation of EMD Performance

In fact, EMD has no mathematical background yet which would allow to evaluate the performance of the algorithm. But EMD could be, in practice, evaluated using toy data sets efficiently. Interpretation of Intrinsic Mode Function is a major issue in evaluating the EMD algorithm. EMD is a completely empirical method which make it difficult to ensure the physical meaning of the extracted IMFs. These IMFs could be different in their appearance and characteristics depending on the parameters used in the algorithm. Moreover, all IMFs except the first one are sums of the spline which used to estimate the envelopes. This assumes that all oscillations parts of the original signal can be represented as a sum of splines. EMD is, further, very sensitive to the sudden changes in the signal e.g. losing the time series signal in specific time intervals. This can simply result to *mode mixing* which prevents interpretation of the extracted IMFs correctly.The second key issue of EMD evaluation is the statistical significance of the extracting IMFs. When the data contains noise, how can the noise be isolated surely from the information? These questions were tackled by [59][58][235] through a study of noise. Flandrin *et al.*'research which is based on fractional Gaussian noise suggested that EMD acts as a dyadic filter [59]. Wu and Huang [235] confirmed Flandrin's results through studying white Gaussian noise instead of fractional Gaussian noise. They also tried to evaluate the statistical significance of an extracted IMF

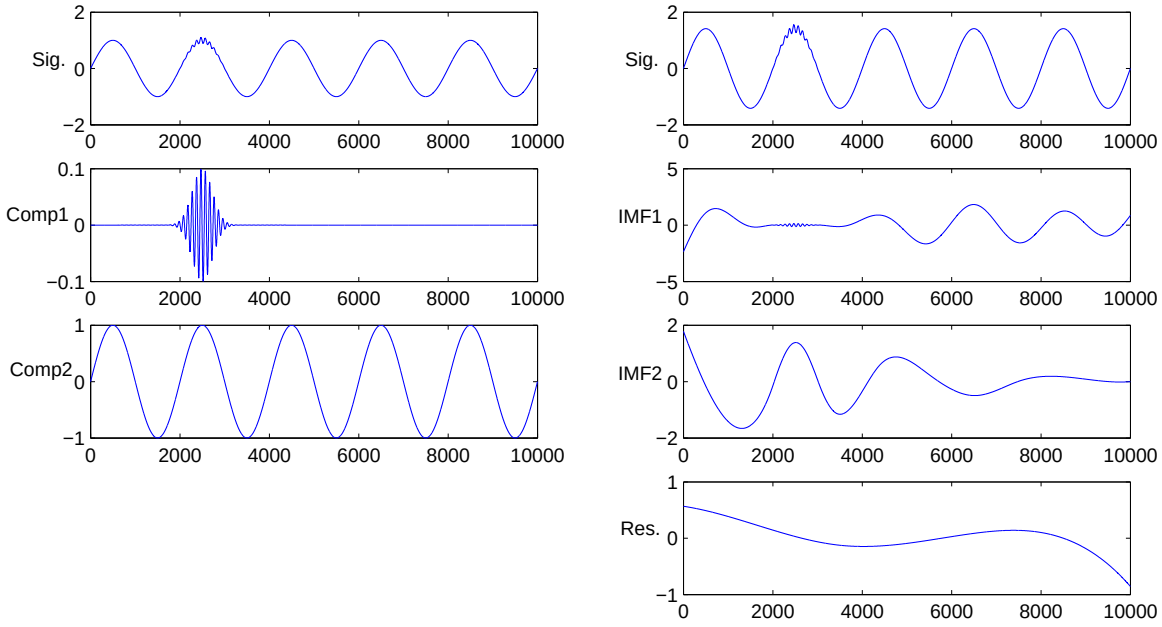

Figure 3.6 **EMD mode mixing problem.** *Left:* the first row is a superposition of the signals in the second row, $Comp1 = 0.1sin(2\pi t_n + 5sin(\pi t/100))(exp(-(t_n-25)^2/10))$ indicated by *Comp1* and the third row, $Comp2 = sin(0.1\pi t_n)$ indicated by *Comp2* to generate the intermittent signal, $sig = Comp1 + Comp2$. *Right:* the intermittent signal *sig* followed by its modes (IMFs) which extracted using plain EMD.

based on the observation that the IMFs of white noise are normally distributed. They assumed that the IMF is informative when its energy density exceeds a noise bound. Energy density of the nth IMF can be calculated by a mathematical expression. Thus, with the study of noise, the method provides a way to separate noise from informative signal.
The sifting process is the core of EMD method, and therefore its quality plays an important role in the performance of EMD method. The quality of a sifting process may be estimated by the number of sifting steps that is required to extract an IMF. In [82], Huang *et al.* investigated the stoppage criterion by changing the number of sifting steps. A confidence interval of sifting steps in the range of 4 to 8 for each extracted IMF was concluded. The latter is done by forcing the number of IMFs to be the same for different sifting steps for different stopping criterion or the way of constructing envelopes.

3.8 EMD Extension

Recently, plain EMD has been extended to improve the algorithm, address problems, adapt to types of data or extend the application areas. In this context, a short overview about some of these extensions, namely Ensemble Empirical Mode Decomposition, weighted Sliding EMD, Multivariate EMD and Green's function-based EMD will be given briefly.

3.8.1 Ensemble EMD

One of the major drawbacks of plain EMD is the occurrence of mode mixing which could happen during the sifting process. It describes a situation where a single mode appears in different IMFs or local oscillations with widely disparate frequency scales show up in a single IMF (see Figure 3.6, $IMF1$ for example). In general, mode mixing can be defined as a consequence of signal intermittency. Additionally, often boundary artifacts result from the sifting process due to improper envelope estimation at the boundaries. To overcome these problem, a noise assisted data analysis method, called *Ensemble Empirical Mode Decomposition* (EEMD), was proposed by [236]. The basic idea is to exploit the self-compensating property of white noise by applying EMD to an ensemble of noisy versions of the original signal. Final IMFs are obtained as averages over the corresponding modes extracted from each member of the ensemble. The approach is based on studies of the statistical properties of fractional Gaussian noise, a versatile model for broadband noise including white noise, reported by Flandrin [59] and Wu and Huang [235]. They showed that EMD operates as an adaptive dyadic filter bank when applied to fractional Gaussian noise. Thereby the mean IMFs keep the natural dyadic filter windows. Thus, mode mixing is significantly reduced and the dyadic property is preserved.
First white noise of finite amplitude is added to the data, and then the EMD algorithm is applied. This procedure is repeated many times, and the IMFs are calculated as an ensemble average, consisting of the signal and added white noise. As an ensemble number increases, the IMF converges to the true IMF [236][237]. Adding white noise to the data can be considered a physical experiment which is repeated many times. The added noise is treated as random noise, which appears in the measurement. In this case, the $m-th$ noisy observation will be

$$x_m(t_n) = x(t_n) + \varepsilon_m(t_n) = \sum_j c_m^{(j)}(t_n) + r_m(t_n), \tag{3.22}$$

where $x_m(t_n)$ is the true signal, $\varepsilon_m(t)$ is the random noise and $c_m^{(j)} = c^{(j)} + \varepsilon_m(t_n)$ represents the IMF obtained for the m-th noise observation. Therefore the resultant IMF $c^{(j)}$ and residua $r(t_n)$ is obtained by averaging all the $c_m^{(j)}$ of the ensemble.

$$c^j(t_n) = \frac{1}{M}\sum_{m=1}^{M} c_m^j(t_n) \tag{3.23}$$

$$r(t_n) = \frac{1}{M}\sum_{m=1}^{M} r_m(t_n) \tag{3.24}$$

where M represents the number of ensembles.

By averaging the respective IMFs, noise contributions will be removed leaving only the true IMFs. However, in practical applications, the white noise is not eliminated completely which leads to extract components with more high frequency. Additionally, EEMD needs to prescribe two parameters, namely the size M of the ensemble and the standard deviation

σ_{noise} of added Gaussian noise. The ensemble number M should be large while noise amplitudes can be selected relatively high. An added white noise of $0.2 \sim 0.4$ amplitude of the standard deviation of the original signal is suggested by Wu *et al.* [236].
However, since there is no method to help selecting the right white noise amplitude, there exist some basic rules which are possible to follow. For data with high frequency, the noise amplitude could be smaller, and in case of low frequency signal, the noise amplitude can be high. Additionally, the amplitude of the intermittency can be used as a reference for tuning noise amplitude. Signals with high intermittency amplitude require higher white noise. It is worth mentioning that, when the noise amplitude is growing for the decomposition, the ensemble number also should be higher to decrease the impact of the white noise in the final result. Furthermore, because of the need to compare the extracted IMFs truly, the number of IMFs into which the signals are decomposed has been fixed in advance. In this case, the sifting process does not care about achieving the IMF criteria. However, the decomposition using EEMD leads to alleviate mode mixing and improve splitting the modes with similar frequencies. The studied time series contains more local extrema because of the added noise which demands too much estimation to the envelopes computationally. Hence, EEMD is computationally costly but it is considered as a further worth enhancement for the EMD technique.
Figure 3.7 shows the EEMD decomposition for the same signal presented in Figure 3.6. The signal is decomposed into a series of IMFs by EEMD method using $M = 20$ and $\sigma_{noise} = 0.0001$, which is shown in Figure 3.7-Right. Adding white noise into the targeted signal facilitates the separation of its different scales with no appearance of a mode mixing problem. EEMD has more concentrated and band limited IMFs components compared to the plain EMD. It represents a significant improvement over the original EMD.

3.8.2 Weighted Sliding EMD

One of the shortcomings of plain EMD is its need of the complete time series before the analysis can start. Many practical applications record biomedical data over long time spans thus producing an amount of data which cannot be handled in one stroke because of limited computational resources. A time version of EMD was proposed by [48], called Sliding Empirical Mode Decomposition (SEMD). SEMD algorithm is based on decomposing a time series of arbitrary length into a residuum and a certain number of IMF-like functions called sliding intrinsic mode functions (SIMFs). It considers sub-segments (windows) of the original time series of length M. These data windows overlap each other in accordance with the step size K of the sliding window mechanism. EMD (or EEMD) is applied to each window separately. Therefore, as each sample makes part of $E = \frac{M}{K}$ consecutive subsegments, the final value of an IMF sample results from combining corresponding samples from E subsegments. Because of the above-mentioned boundary problems of EMD, the step size k should be selected much smaller than m, otherwise discontinuities would occur. In addition to that, the estimated values of E_i for each sample of $x(t)$ might be different. These results values of SEMD represent the mean value of all estimates $x(t)$.

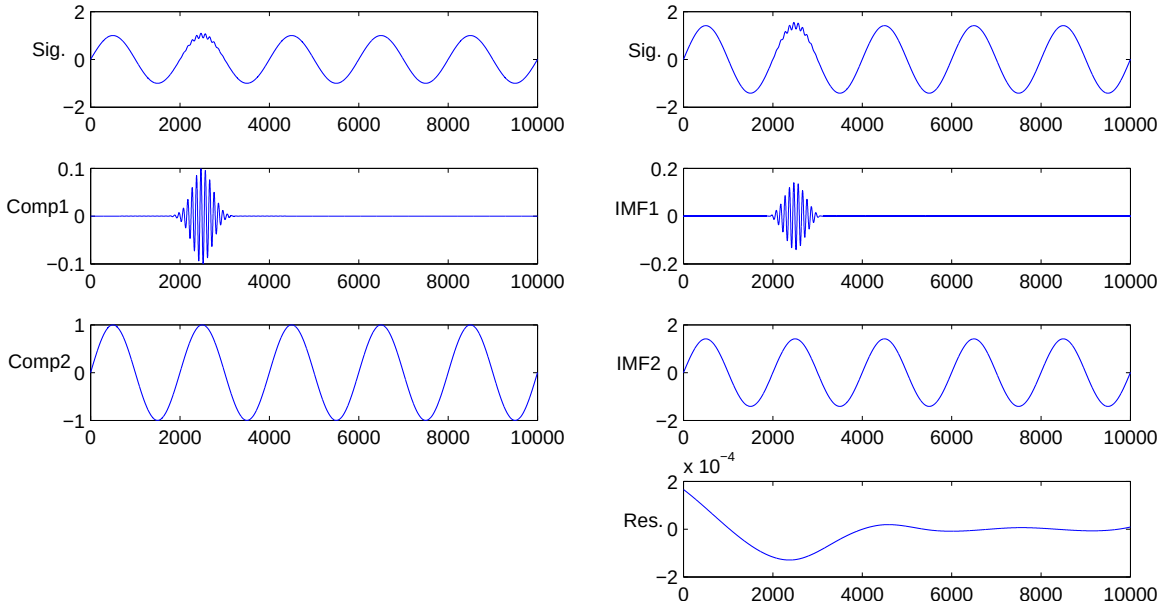

Figure 3.7 **EEMD decomposition for eliminating mode mixing problem.** *Left:* the intermittent signal (sig) and its components as presented in Figure 3.6-Left. *Right:* the intermittent signal (sig) and its extracted modes (IMFs) by applying EEMD.

Eventually, EMD decomposes the segment m_i of the original signal into j different IMFs $x_{m_i j}(t)$ and a local residuum $r_{m_i}(t)$ according to

$$x_{m_i}(t) = \sum_j x_{m_i j}(t) + r_{m_i}(t), \tag{3.25}$$

where the number of sifting steps is fixed equally for all segments.

All the resulting IMFs are gathered in a matrix with corresponding sample points in which the estimated values of every sample represent a column of the matrix with E entries. The columns for the beginning or end of the time series are incomplete, and consequently they are ignored in the next steps of processing. This in turn guarantees that all columns contain the same amount of information which will be used to estimate the average IMF amplitudes at every time point t in each segment. Finally, this results for $t > m$

$$x_j(t) = \frac{1}{E} \sum_i^{i+E-1} x_{m_i j}(t), \tag{3.26}$$

$$r(t) = \frac{1}{E} \sum_i^{i+E-1} r_{m_i}(t), \tag{3.27}$$

$$i = \frac{t-m}{k} + 2 \tag{3.28}$$

where $x_i(t)$ are the resulting functions called *SIMFs*, and $r(t)$ is the sliding residuum. Thus, for every sample $x(t)$- the mean value of the E decompositions represents the result of the SEMD decomposition. Note that the number of sifting steps and IMFs should be fixed for all decompositions of all windows, otherwise problems would appear.
Due to computing the mean value of the E estimates, the influence of the boundary artifacts will be reduced when using SEMD. However, it is expected that estimates originating from the boundaries are to be more defective like the ones caused by the middle part of any specific window. To overcome this problem, an extension to SEMD called *weighted Sliding Empirical Mode Decomposition* (wSEMD) was introduced by [47]. wSEMD is based on a weighted sum of the estimates which will be used to reduce the influence of estimates stemming from the border of a window. For every window, the resulting IMFs and residua are multiplied by a vector of rank m that is generated from a Gaussian distribution.

$$w(n) = \exp\Big(-\frac{1}{2}\Big(\alpha\frac{2n}{N}\Big)^2\Big), \tag{3.29}$$

$$-\frac{N}{2} \leq n \leq \frac{N}{2}, \quad \alpha = 2.5, \quad N = m-1, \tag{3.30}$$

Further details about SEMD, wSEMD and their applications for biomedical signals can be found in [48][47][239][241][238][242][240].

3.8.3 Multivariate EMD

Multivariate Empirical Mode Decomposition (MEMD) [170][133] is the multivariate extension to plain EMD introduced above. When interpreting plain EMD as an univariate approach of decomposing one dimensional time course, MEMD can be seen as a multivariate approach by taking the response of a system from several channels as a multi-dimensional signal with each channel – like EEG-channels for instance – representing one dimension in an n-dimensional space. The time course can be seen as a trajectory propagating in this multi-dimensional space and MEMD tries to decompose this signal into multi-dimensional IMFs, which then can rather be seen as rotational than oscillatory modes. The main problem for the multivariate approach is that there is no proper definition of extrema in n dimensions. Rehman and Mandic [170] tackle this issue by generalizing the aspect of creating envelopes around the time course to n dimensions. At first, a set of Hammersly-sequenced n-dimensional direction vectors is introduced sampling the n-dimensional space as uniformly as possible. Afterwards the signal is projected onto each direction vector to get one-dimensional representations of the signal. Then the extrema of those projections are extracted and re-projected into the n-dimensional space resulting in sets of n-dimensional maxima and minima for each one-dimensional projection, which then can be used to construct n-dimensional envelopes. Eventually, the core principle of EMD – averaging envelopes – can be applied to a multivariate signal by averaging these sets of n-dimensional envelopes. Afterwards, the same procedure as in plain EMD is applied. The stopping criterion for a multi-dimensional IMF is similar to that of the plain EMD algorithm, besides the comparison of number of zero crossings and number of extrema does not hold anymore, as there

is no proper definition of zero crossings in n-dimensional space. An additional benefit of doing MEMD to plain EMD is that – besides improvement in avoiding mode mixing – frequency scales of same index IMFs align [170].
As for the plain EMD approach, an *ensemble noise assisted* method is proposed for MEMD. It is important here do distinguish between noise assisted and ensemble approaches. For plain EMD these two approaches are synonymous. In case of a MEMD it has to be mentioned, whether only a noise assisted MEMD (NA-MEMD) [171] or an ensemble noise assisted MEMD (ENA-MEMD) [172] is applied. Compared to MEMD, the NA-MEMD introduces l channels consisting of white Gaussian noise in addition to the signal channels spanning the n-dimensional space of the multivariate signal, since it is suggested not to add noise onto the already existing signal itself in the multivariate case. After EMD is done the l noise channels are discarded. For the noise amplitude $2-10\%$ of the signal amplitude is suggested [172]. The ensemble principle is introduced by creating several realizations of IMFs by using different initializations of noise for several NA-MEMD runs resembling the same principle as for EEMD in the univariate case. The multivariate aspect of MEMD can be exploited in EEG studies by looking for multivariate phase synchrony [148] or several other intrinsic multi-scale measures [124].

3.8.4 A Green's function-based EMD

Recently, Al-Baddai *et al.* [6] has developed a new version of 2 Dimensional Empirical Mode Decomposition (2D-EMD) based on Green's Functions (GFs) in tension. The latter is employed to build surfaces during sifting process instead of using the normal spline interpolation. The main point that GFs forces an envelope or surface to pass through a given number of the data constraints. Consequently, unwanted oscillations between data points are avoided. Generally, the general solution of any point on the envelope based on N given data constraints can be expressed using GFs as follows

$$s(\mathbf{x}_u) = \sum_{n=1}^{N} w_n \Phi(\mathbf{x}_u, \mathbf{x}_n) \tag{3.31}$$

where x_u are the points at which the envelope is unknown, x_n is the $n-th$ data constraint (in case of the EMD it represents the extracted extremum during sifting process), $\Phi(x_u, x_n)$ is the Green's function and w_n are the associated unknown weights in the envelope representation. It was proven by Sandwell [187] that the Green's function $\Phi(\mathbf{x})$ satisfies the following relation at any data constraint $\mathbf{x}_n$, $n = 1, \ldots, N$

$$\left[D\Delta_{op}^2 - T\Delta_{op}\right] \Phi(\mathbf{x}_u, \mathbf{x}_n) = \delta(\mathbf{x}_u - \mathbf{x}_n) \tag{3.32}$$

where, Δ_{op}^2 and $\Delta_{op} = \nabla^2$, denote the bi-harmonic, the Laplace and the Nabla-operator, respectively, D is the flexural rigidity of the envelope and the tension parameter T. The latter must be between 0 and 1 (when T =0, GFs is considered as normal spline interpolation and when T=1 is considered as linear interpolation). Now, to solve Equation 3.32 for data constraints, the weights of known data constraints is evaluated first as

$$s_m = \sum_{m=1}^{N} w_m \nabla\Phi(\mathbf{x}_m - \mathbf{x}_n) \cdot \hat{\mathbf{n}}_m \qquad m = 1,\ldots,N.$$

which results in a quadratic linear system

$$\mathbf{Gw} = \mathbf{c}$$

where the Green's matrix $\mathbf{G}$ collects all Green's functions $\Phi(\mathbf{x}_m - \mathbf{x}_n)$ at the data constraints $m,n = 1,\ldots,N$. Corresponding slopes s_m in directions $\hat{\mathbf{n}}_m$. To compute the GFs, the curvature of GF is introduced

$$\Psi(\mathbf{x}) = \nabla^2\Phi(\mathbf{x}) \tag{3.33}$$

When Fourier transform is applied, the result will be

$$\left[\Delta_{op} + \frac{p^2}{k^2}\right]\Psi(\mathbf{k}) = -\frac{1}{T}\frac{p^2}{k^2}. \tag{3.34}$$

Now, when Fourier transform is computed again, the general solution becomes

$$\Psi(\mathbf{k}) = -\frac{1}{T}\left(\frac{p^2}{k^2+p^2}\right) \tag{3.35}$$

where k is the wavenumber and $\mathbf{k}$ is the Fourier transform of $\mathbf{x}$. The exact solutions, however, depend on the dimension of the problem. For the case $p > 0$ which corresponds to $T > 0$, the solutions are [187]

$$1D : \phi(x) = e^{-p|x|} + p|x| - 1 \tag{3.36}$$

$$2D : \phi(x) = log(p|x|) + K_0(p|x|). \tag{3.37}$$

where K_0 is the Bessel function. Exact solutions for even higher dimensional problems exist. However, they are not relevant for the scope of this thesis. Recently, the 2D version, called GiT-BEMD, has been successfully applied to fMRI images [5]. The latter was jointly collected with our EEG data. Exact solutions for even higher dimensional problems exist. However, they are not relevant for the scope of this thesis.

Chapter 4

Contour Integration Task

4.1 Perceptual Learning

An essential task of visual system is to identify shapes and borders of a visual scene that belong together as meaningful objects. In the early visual system, neurons carry local image attributes of the visual scene. Visual integration is defined as the process of combining these attributes into a a unique structure more suitable for the guidance of behavior [162]. This combination which is classified under the term "perceptual grouping" requires some kind of grouping process. The human visual system performs such grouping processes in a hierarchy of serial processing steps, depending on spatial, temporal, and chromatic features of the stimulus [19][161][69][114]. There is a set of rules which was elaborated by Gestalt psychologists, that manages these grouping processes in order to control the principles of perceptual organization [100][227]. These rules aim to formulate the regularities according to which perceptual input is organized in a regular, simple, and meaningful form. The Gestalt rules of perceptual organization include (see Figure 4.1):

- *Proximity*: stimulus elements that are near each other are inclined to be perceived as a group.
- *Similarity*: stimuli that are perceived similar will be perceived as a group.
- *Closure*: stimuli are likely to be grouped into complete figures.
- *Common Fate*: objects are seen as lines that move along the smoothest path.
- *Figure Ground*: it is known as separating figures from their background.
- *Continuity*: people connect individual forms so they tried to minimize discontinuity.

One special case of perceptual grouping is contour integration where local parts of an intersected contour are re-integrated to form a continuous contour line, following the Gestalt rule of good continuation. The latter has been known for a long time ago, see [226], and it helps to recognize a number of geometric illusions as an object or just as a specified path of elements in visual perception [54]. Hence, Gabor elements can represent rather the receptive field properties of orientation selective simple cells in the primary visual cortex. Consequently, such Gabor elements are used as a favorable stimuli for the examination of

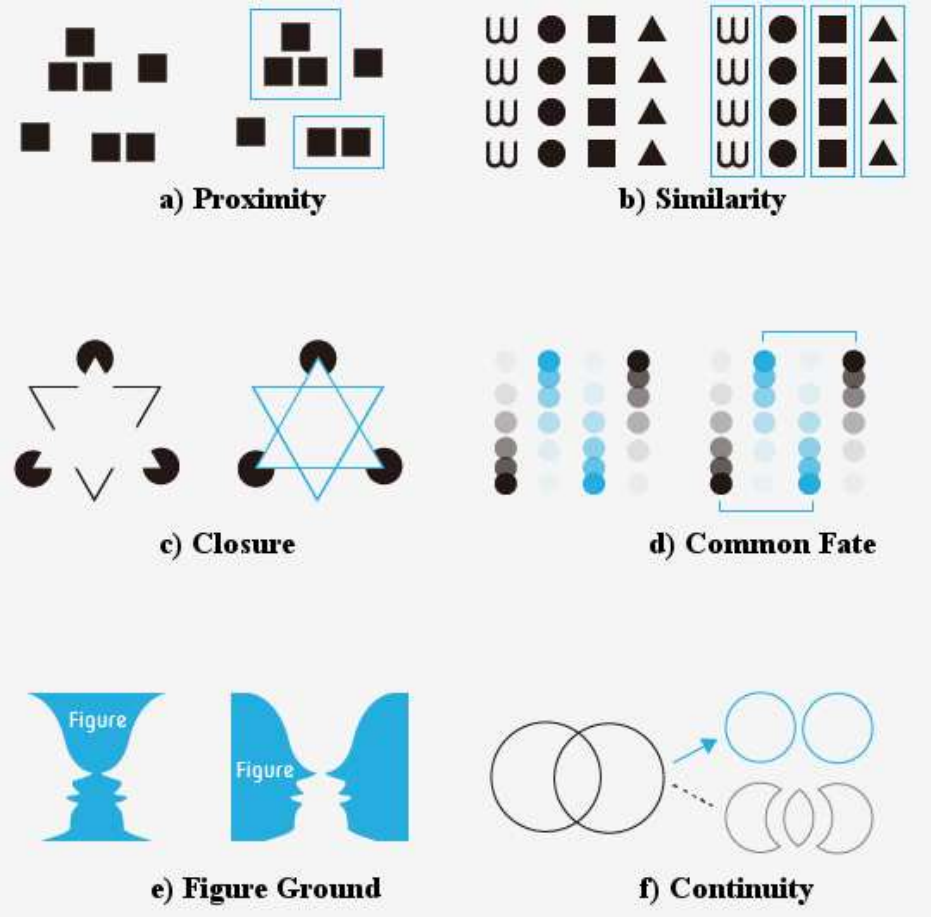

Figure 4.1 **Examples of Gestalt rules for perceptual grouping** (adapted from [166]).

these small spatial filters and their interactions [108]. Using Gabor elements with different orientation angles in psychological experiments is due to a physiological background.

4.1.1 Contour Integration

One such perceptual grouping process is a contour integration which is one of the most elementary tasks during visual feature integration. It is the main visual process that creates representations of continuous borders and shapes on the basis of the related orientations of multiple edge elements. Contour integration is commonly measured as the ability to detect the shape, position, or existence of a closed contour created from non-adjacent elements, included within a display of randomly oriented elements. Contours make the boundaries of objects which are considered as the first stage in shape perception. First attempts to introduce a descriptive basis for contour integration considered the task is so complicated for being implemented by local feature processing units early in the visual area. So, they tried to use a globally mechanism that combines information from multiple feature dimensions in order to recognize the visual object [209][20]. However, this concept was challenged by many researchers in neuroimaging [12][106][13], computational

[65][165][120][33][110][191], neurophysiological [118][18][134][186] and psychophysical studies [54][107][138][180][50][143]. The task of contour integration can be outlined by a series of three processing stages at different levels of the visual hierarchy according to how it is achieved by the visual system. *Filtering stage* is the first stage which would be concerned with extracting local features of stimulus elements that belong to the same contour. In the next stage *linking stage*, connections of similar elements are modeled based on local features like orientation, proximity or contrast. The final stage *integration stage*, is concerned with grouping individual elements into an entire contour based on the connections models and consequently, constructing a global perceived object [63]. The ability to integrate the individual elements (Gabor) into a contour depends on their spacing and orientation with regard to the path orientation [54][119]. Some stimulus characteristics appear to have an effect on connecting contour elements: closed contours are more easily detected than open ones [109][165]. Similarly, symmetric contours are also easier to detect than asymmetric ones [128]. Actually, contour integration gets better when Gabor elements are oriented in perpendicular direction to the contour within a closed area, and gets worse, when these elements are oriented parallel to the contour [38]. In this thesis, we used exclusively Gabor arrays as visual stimuli. It could thus be objected that the results are not specific for contour integration, but reflect some general visual processes under conditions of low stimulus visibility.

4.2 Experiment Materials

4.2.1 Subjects

The subjects participating in the study encompassed 5 male and 13 female volunteers between $20-29$ years old, i. e. (22.79 ± 2.7) $[years]$. All subjects were right-handed and had normal or corrected-to-normal vision. Based on self-reports, the subjects had no neurological or psychiatric disorders, brain injuries or drug dependencies. This study also was approved by the local ethics committee (study number $10-101-0035$). Subjects were treated according to the principles laid down in the Helsinki declaration.

4.2.2 Gabor Stimuli

The stimuli were generated with a procedure similar to that of [135]. Stimulus displays contained odd symmetric Gabor elements arranged in an invisible 10 by 10 grid subtending 16.6 deg $\times$ 16.6 deg of visual angle. The corresponding stimulus protocol is illustrated in Figure 4.2. The luminance distribution $L(x,y)$ of a single Gabor element is defined by the equation

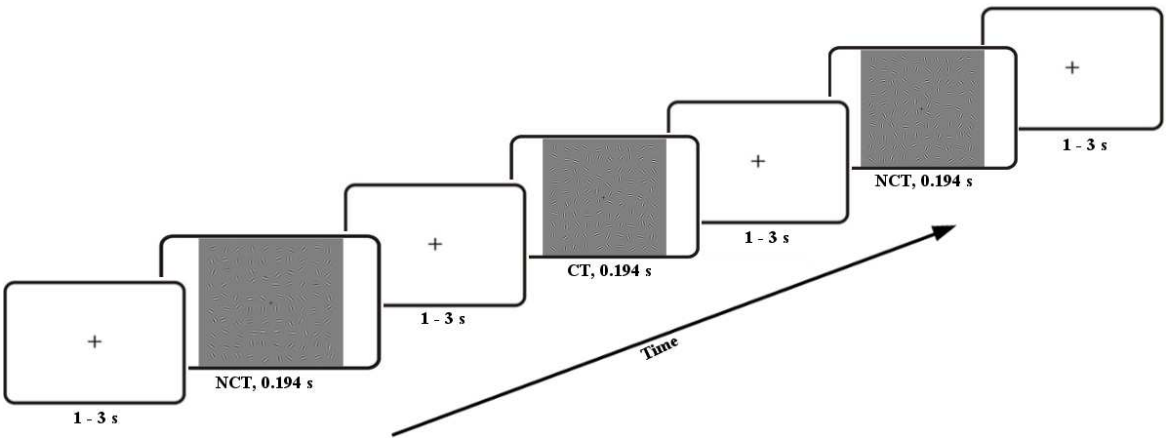

Figure 4.2 **Stimulus protocol including Gabor patches either forming a contour (CT) or none (NCT).**

$$L(x,y) = L_0(1 + s(x,y) \cdot g(x,y)) \tag{4.1}$$

where $L(x,y)$ $[cd/m^2]$ is the luminance at point (x,y) and L_0 is the background luminance. The function $s(x,y)$ represents a 2D - sinusoid, describing the carrier wave, and $g(x,y)$ the related Gaussian envelope, describing the amplitude modulation. These functions are given by

$$s(x,y) = C \sin[k_x \cdot x \cos(\theta) + k_y \cdot y \sin(\theta)] \tag{4.2}$$

where $C = 0.9$ is the Michelson contrast, $\| \mathbf{k} = (k_x, k_y)^T \| [rad/m] = 2\pi f [cpd]$ is the angular wave number with $f = 3$ $[cpd]$ the corresponding spatial frequency in $[cycles/deg]$, and θ is the orientation from vertical which depends on the experimental condition. Furthermore,

$$g(x,y) = \exp\left(-\frac{x^2+y^2}{2\sigma^2}\right) \tag{4.3}$$

where $\sigma = 0.25$ deg is the standard deviation of the Gaussian envelope, measured in degrees of visual angle.

For contour displays, a path of 10 invisible line segments was constructed and placed at a random location within the stimulus area, with the restrictions that none of the segment centers, where the Gabor elements were finally placed, fell into the inner 2×2 grid cells, and that at least 4 segment centers fell into the inner 6×6 grid cells. This ensured that the Gabor path did not cross the central fixation mark, and that the eccentricity of the path was not too large. The angle between adjacent line segments was the path angle α plus an orientation jitter $\Delta\alpha$ drawn from a uniform distribution $p(\Delta\alpha) \in [-1, +1]$. Gabor elements were placed at the center of each line segment and aligned to the segments orientation. The separation s between neighbouring elements depended on the length of the corresponding line segments. It was chosen as $\alpha \pm \delta\alpha = 2 \pm 0.55$ degrees of visual angle. After setting up the Gabor path, empty grid cells were filled with randomly oriented Gabor elements. The size of the grid cells was set to $2s/(1+\sqrt{2}) = 1.66$ degrees of visual angle. This ensured that mean distance between distracting Gabor elements was close to the mean distance between the elements making up the Gabor path. The distracting Gabor elements were placed in the center of each grid cell and jittered vertically and horizontally by $\pm$ 0.55 degrees of visual angle. New Gabor elements were not drawn if their visible part overlapped with an already existing Gabor element by more than 5 pixels. The whole stimulus was withdrawn if more than 10 Gabor elements could not be drawn. Thus, each stimulus contained $90-100$ Gabor elements. For constructing non-contour displays, the same algorithm was used as for the construction of contour displays but rotating adjoining Gabor elements by $\pm$ 45 deg. Thus, non-contour displays resembled contour displays with respect to spacing, positioning and the number of elements, but did not contain a Gabor path.

For the experiment, a set of 150 non-contour stimuli was generated, which was the same for all subjects. Then a set of 150 contour stimuli was generated separately for each subject, where the path angle α was adjusted to the individual maximum tolerable path angle. These angles were obtained during behavioral pre-testing and ranged from 21 deg $\rightarrow$ 34 deg.

4.2.3 Experimental Procedure

Subjects were positioned supine in the scanner. The visual stimuli were back projected onto a translucent circular screen (LCD video projector, JVC DLA-G20, Yokohama, Japan) and was seen on a mirror reflecting the projected image. A standard PC running Presentation 12.0 (Neurobehavioral Systems Inc., Albany, Canada) was used for stimulus presentation. The projector had a resolution of 800 by 600 pixels at a refresh rate of 72 $[Hz]$. The viewing distance to the projection screen was 64 $[cm]$.

The trials started with the presentation of a central fixation cross that remained visible throughout the experimental block. After a random interval from $1000-3000$ $[ms]$, a stimulus was presented for 194 $[ms]$, followed by a blank screen. The next trial started after the response, or after a time-out of 3000 $[ms]$ if the subject did not respond. The behavioral responses were recorded with two fiber-optic response boxes (Lumitouch, Photon Control, Ltd, Burnaby, BC, Canada) where one key was provided for each finger of the left and the right hand, respectively. The subjects were instructed to detect contour stimuli. One half of the subjects used the left hand for a *contour* response and the right hand for a *non-contour* response. For the other half of the subjects the response mapping was reversed. Altogether, the subjects were presented with 300 stimuli in a random order, partitioned into 15 blocks with 20 trials each.

4.2.4 EEG Data Acquisition

The EEG was recorded concurrently with fMRI in a Siemens Allegra 3 Tesla Head Scanner. In this thesis, we focus on the EEG data. The fMRI results are reported in a separate work [4]. The EEG was recorded with an MR-compatible 64 channel EEG system (BrainAmp MR plus, Brain Products, Gilching, Germany). The scalp EEG was obtained from 62 equidistant electrodes that were mounted in an elastic cap (EasyCap, Herrsching-Breitbrunn, Germany) and were referenced to FCz during recording. Impedances were kept below 20 $[k\Omega]$. The signals were amplified between 0.1100 $[Hz]$, with a notch filter at 50 $[Hz]$ in order to cancel out mains hum. The sample rate was at the maximum resolution of 5000 $[Hz]$. To control for eye-movement artifacts, the vertical electrooculogram was recorded from an electrode placed below the left eye. An electrocardiogram (ECG) electrode was placed below the left scapula in order to facilitate the off-line removal of cardioballistic artifacts. The clock of the EEG amplifier was synchronized with the clock output of the MR scanner using a *SynchBox* manufactured by Brain Products (Gilching, Germany). Electrode locations are presented in Figure 4.3.

4.2.5 EEG Data Preprocessing

MR gradient switching produces large artifacts in the EEG each time a new slice is collected. A second source of artifacts is the movement of electrodes and conductive blood inside the MR scanner due to the cardiac cycle. The continuous EEG data were cleaned from both gradient and cardioballistic artifacts by means of artifact template subtraction as implemented in the FMRIB plug-in for EEGLAB [40][150].

- Gradient artifact onsets were determined relative to the MR volume onset marker that was recorded along with the EEG. With respect to gradient artifacts, a template was constructed for each slice artifact and for each channel separately and then subtracted from the actual artifact. The template consisted of a moving average of 21 neighboring slices and a linear combination of the major principal components describing the residual artifacts that remain after artifact subtraction. These were determined automatically by means of sorted eigenvalues. The corrected data were down - sampled to 500 $[samples/s]$ and

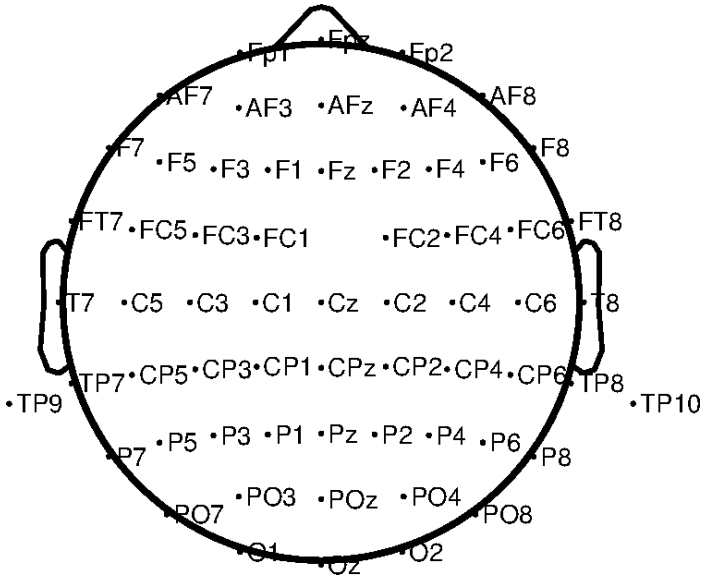

Figure 4.3 **Position of** 62 **EEG electrodes.**

highpass-filtered (FIR) at 0.5 $[Hz]$. Bad stretches of data in the continuous EEG, due to incomplete gradient artifact removal or other idiographic artifacts, were identified and removed by visual inspection.

- Cardioballistic artifacts occur around heartbeats which show a characteristic deflection in the ECG electrode denoted as *QRS complex*. The FMRIB plug-in provides a reliable algorithm for the detection of *QRS onsets*. For removing cardioballistic artifacts, a temporal principal component analysis (PCA) was performed on each EEG channel. The first three components were taken as an optimal basis set for describing shape, amplitude and scale of the artifact. This set was fit to, and then subtracted from, each artifact instance. As for the removal of gradient artifacts, this was performed for each channel separately.

Preprocessed EEG data subsequently were subjected to an independent components analysis (ICA) using the extended INFOMAX algorithm [115]. Components related to artifacts were identified by visual inspection of the component topographies and power spectra. Main sources of artifacts were eye blinks, eye movements, tonic muscle activity, as well as residual pulse and gradient artifacts. Components identified as artifact-related were removed, and the remaining components were back-projected into the EEG signal space. The data was then segmented into intervals of 3 $[s]$ duration, centered around the stimulus onset, and baseline-corrected within the whole interval. Single trials were again inspected and rejected if they contained artifacts. The overall rejection rate was between 6.7 % and 42 % across subjects (mean 22.5 %), i. e., between $174 - 280$ trials per subjects (on average 232.5 for both conditions) were available for the analysis.
EEG data were analyzed using custom code and the EEGLAB toolbox developed at the Swartz Center for Computational Neuroscience (SCCN), USA [40]

(http://sccn.ucsd.edu/eeglab/). For signal analysis, the segmented data were further reduced to intervals of 1000 $[ms]$ duration, each containing an onset of a Gabor stimulus. The epochs (trials) to be analyzed extended from $t_0 - 150\ [ms] \ \rightarrow\ t_0 + 850\ [ms]$ relative to stimulus onset at t_0, corresponding to 500 samples.
Hence, these single trial signals are denoted as

$$x^{(ch)}(t_n, s) \qquad \text{with} \qquad n = -B, -B+1, \ldots 0, 1, \ldots M-1, \qquad ch = 1, 2, \ldots C$$

where ch denotes the index for the recording position (channel), $s \in SC = \{CT, NCT\}$ denotes the stimulus condition and $n_t = 1, \ldots N_t$ with N_t the total number of trials. The index t_n is related to discrete time and t_0 indicates the time of stimulus presentation, meaning that the segment starts $B = 75$ samples before stimulus onset t_0 and lasts more $M = 425$ samples. In brain studies, evoked potentials are extracted from single trial recordings by averaging single-trial signals, corresponding to a particular stimulus, over all trials. In this study, two different stimulus conditions, either contour true (CT) or non-contour true (NTC), were randomly presented. Then, for each condition, average signals $x_{avg}^{(ch)}(t_n, s \in SC)$ were estimated

$$x_{avg}^{(ch)}(t_n, s \in SC) = \frac{1}{N_{SC}} \sum_{s \in SC} x^{(ch)}(t_n, s) \quad n = -B, -B+1, \ldots, 0, \ldots, M-1$$

resulting, for each participant, in two sets of ERP signals $x_{avg}^{(ch)}(t_n, CT)$ and $x_{avg}^{(ch)}(t_n, NCT)$ using N_{CT} and N_{NCT} trials, respectively.
Responses to Gabor stimuli exhibited a large biological variability as can be seen from Figure 4.4. There, for the purpose of illustration only, global ERPs are shown of all subjects as averages over all channels. Such global averages provide a rough idea about the extent of biological variability between individual stimulus responses.

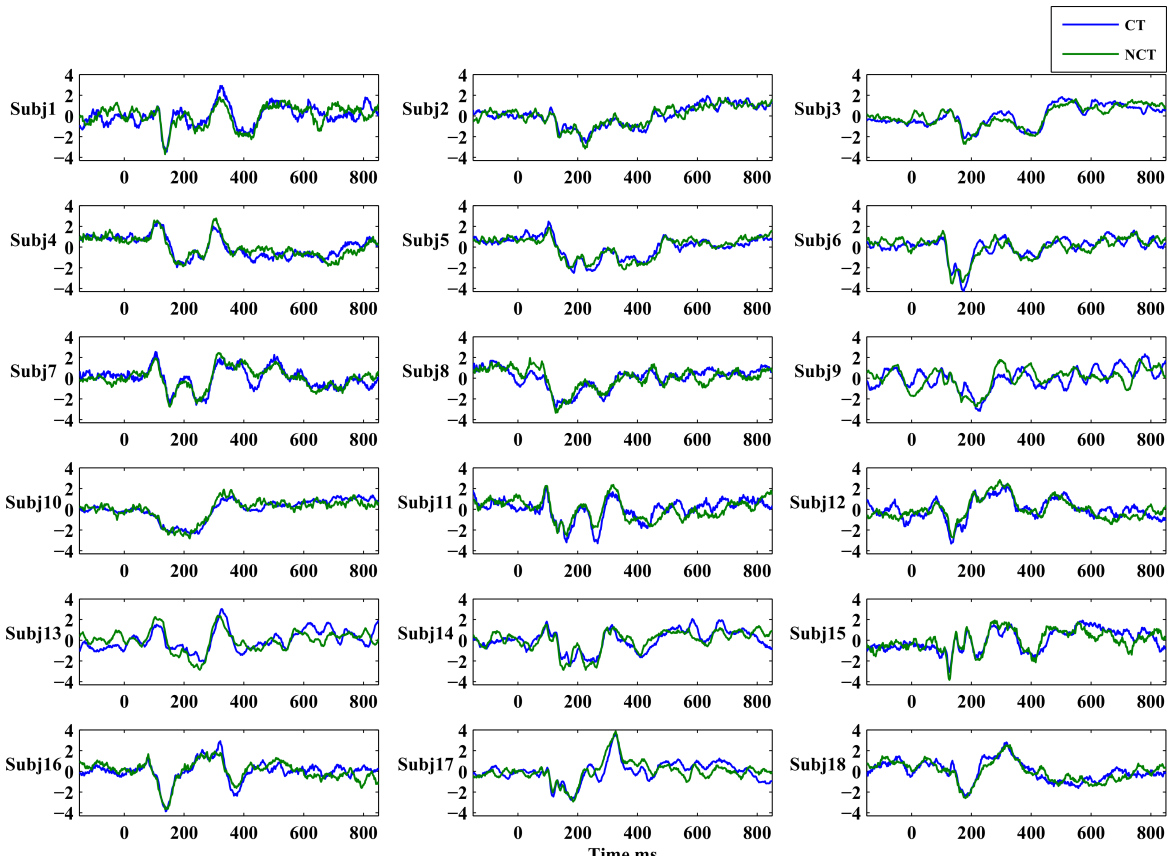

Figure 4.4 **Global averages of individual ERPs elicited by the two stimulus conditions CT and NCT.** The ERP amplitudes are normalized to zero mean and unitary standard deviation. ERPs for both conditions are superimposed onto each other, *blue*: Contour condition and *green*: Non-contour condition.

Chapter 5

Forward Modeling of the EEG Data based on EEMD

The goal of electroencephalogram (EEG) source localization is to find the brain areas that are responsible for generating the interesting EEG waves. It consists of solving two main problems, forward and inverse. The EEG forward problem involves calculating the electrical potentials for specific source locations, orientations and signals which is the first step towards the reconstruction of the spatio-temporal activity of the neural sources of EEG. In this chapter, a new method to calculate these potentials depending not directly on the raw data is introduced. First the recorded EEG data are analyzed using a data-driven analysis method, EEMD. This analysis discusses characteristic features of event related modes (ERMs) resulting from the decomposition. We investigate whether an EEMD analysis can provide underlying characteristic modes which show differences between stimulus conditions with clear statistical significance. This chapter is organized as follows, Section 5.1 is devoted to setting the optimal way for the analysis which includes estimating: EEMD parameters, ERP components and ERMs of interest. Estimating EEMD parameters such as sifting iterations, noise amplitude and ensemble size could affect the characteristic features of modes which will be extracted next. EEGs are investigated at the level of event related potentials (ERPs) which represent averages over a sufficiently large number of single trial recordings. Typical ERP components and their related latencies are then compared for different stimulus conditions. This section tries to explore the interesting ERP components. Furthermore, this section presents a detailed description of the EEMD analysis applied. It explains how EEG signals are decomposed by applying EEMD method. The latter will be done in two different ways: *Approach A* and *Approach B*. Several different investigations and tests will be implemented in this chapter, in *Results* Section 5.2. The latter accounts for details of the EEG analysis and summarizes the main findings. It presents and quantifies the results obtained. Component time courses and related head topographies further illustrate these results. Finally, the chapter will end with *Discussion* Section 5.3 which offers a thorough discussion of these results.

5.1 The Optimal Configuration for the Analysis

The optimal analysis of any data entails choosing the "best" between various alternatives. The goodness of the alternatives has an affect on the performance index. This section discusses selecting the best structure, method, and parameters for the analysis. EEMD is used as an analysis tool that allows to extract component signals which contain decisive information about responses to contour and non-contour stimuli. EEMD has been selected instead of plain EMD to avoid problems like mode mixing, boundary effects and so on .

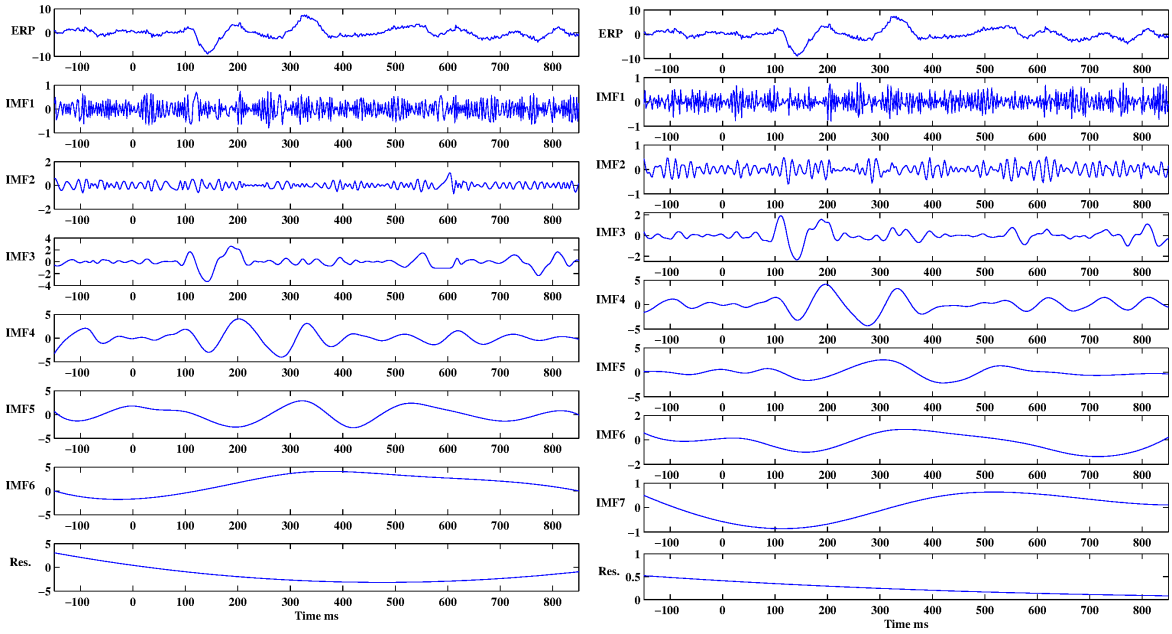

Figure 5.1 **Extracted modes when applying EMD and EEMD.** *Left:* EMD decomposition on ERP of EEG signal. *Right:* EEMD decomposition on the same EEG signal in the left.

An example of using EMD and EEMD methods to decompose EEG signals is given in Figure 5.1, where the two methods were applied to the same EEG signal presented in the first row. As can be seen, $IMF2$ of EMD decomposition in the left side is a consequence of signal intermittency. In addition, boundary artifacts resulted from the sifting process at the boundaries. For example $IMF3$ and $IMF4$ of EMD decomposition (left side) can be alleviated when applying EEMD (right side). Note that the number of extracted modes by EEMD has increased because of the added noise.

5.1.1 EEMD Preparation

EEMD needs to prescribe two parameters, namely the size E of the ensemble and the standard deviation σ_{noise} of added Gaussian noise. Those two parameters were chosen empirically after several attempts which indicated an optimal ensemble number $E = 20$ and a proper standard deviation $\sigma_{noise} = 0.2 \cdot \sigma_{signal}$, where σ_{signal} denotes the standard deviation of the signal amplitude distribution. Figure 5.2 shows EEMD decompositions of EEG signal

which were implemented with different levels of noise $\sigma_{noise} = [0.001, 0.01, 0.1, 0.2] \cdot \sigma_{signal}$ and an ensemble size of $E = 20$. As can be seen in the figure, there are no big differences between the extracted IMFs, however, a slight improvement has been observed in $IMF2$ and $IMF3$ when EEMD was implemented with noise 0.2.

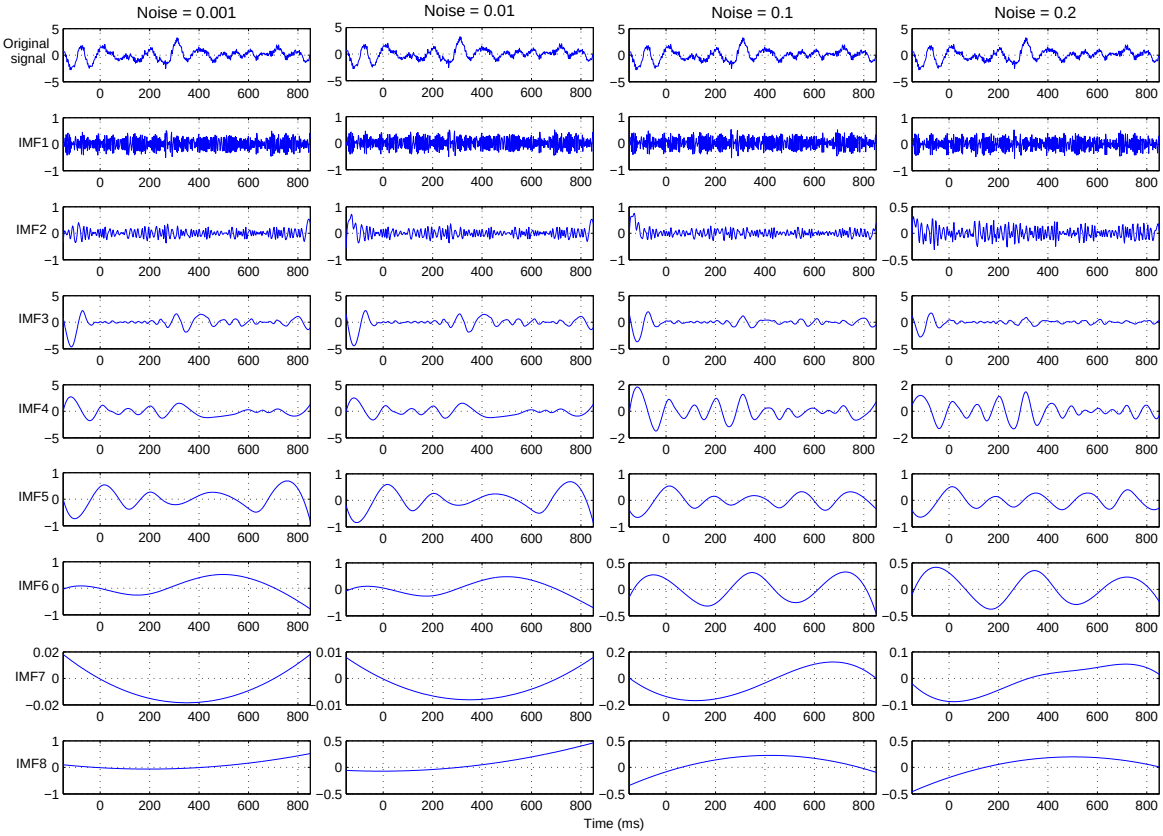

Figure 5.2 **EEMD decomposition on ERP of EEG signal.** In the EEMD, an ensemble size of $E = 20$ is used with different added white noise in each ensemble member which has a standard deviation of $\sigma_{noise} = (0.001, 0.01, 0.1, 0.2) \cdot \sigma_{signal}$.

To determine the ensemble size E, several EEMD decompositions of EEG signal with different ensemble sizes $E = (5, 10, 20, 50)$ are done using a fixed noise of $\sigma_{noise} = 0.2 \cdot \sigma_{signal}$ as illustrated in Figure 5.3. The differences between extracted modes when increasing the ensemble size are only tiny, hence less noticeable. Furthermore, a large ensemble size leads to increasing the computation time.
Furthermore, because of the need to average corresponding IMFs over several trials, the number of IMFs into which the signals are decomposed has been fixed in advance. Empirically, after systematically varying the number of modes, a decomposition into 7 IMFs plus a residuum was considered most appropriate (see Figure 5.12 and 5.13). Slightly abusing the definition of a residuum, by integrating the latter as an additional IMF, all signals were decomposed into 8 IMFs finally. Additionally, the sifting process was implemented with a fixed number of iterations instead of verifying the IMF condition [240].

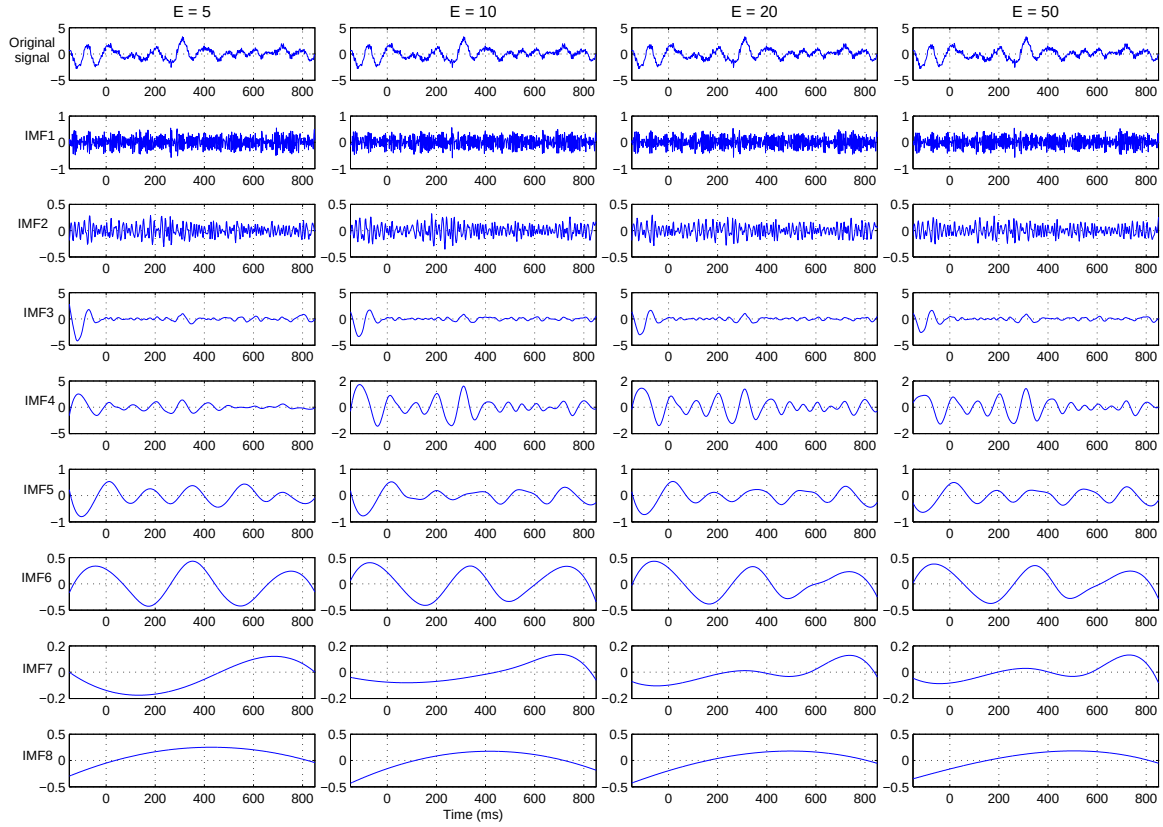

Figure 5.3 **EEMD decomposition on ERP of EEG signal.** The decomposition is implemented with different ensemble sizes of $E = (5, 10, 20, 50)$ and an added white noise which has a standard deviation of $\sigma_{noise} = 0.2 \cdot \sigma_{signal}$.

5.1.2 Event-Related Modes from EEMD Decomposition

A more informative way to analyze ERPs concerns the application of signal decomposition techniques which offer a principled way of extracting characteristic features from the recordings which in turn, reveal significant response differences between both stimulus conditions. In this work, EEG signals are decomposed by applying ensemble empirical mode decomposition. The latter will be applied to the set of signals in two different ways. Approach A preserves phase-locked modes and disregards non-phase-locked modes, while approach B considers both, phase-locked as well as non-phase-locked, modes during mode decomposition:

- Approach A: EEMD after averaging over trials.

  After averaging over trials, EEMD is applied to all single channel ERPs, i. e. to $x_{avg}^{(ch)}(t_n, CT)$ and $x_{avg}^{(ch)}(t_n, NCT)$, respectively, thus yielding *event-related modes* (ERMs) which contain only those parts of the response signals that are phase-locked to the stimuli. Averaging has been performed for each stimulus condition separately and EEMD decomposition was performed for each ERP signal. Then IMF (ERM) amplitudes have been estimated

within intervals centered at the characteristic peaks of the corresponding ERMs, i. e. for $P100, N200$ etc. as was explained above.

- Approach B: EEMD before averaging over trials.

  Alternatively, EEMD is applied to each single trial response signal $x^{(ch)}(t_n, s)$ at each channel separately. Then all corresponding IMFs become, for each of the two stimulus conditions, averaged over all trials to yield related ERMs. The latter now also contain information about signal components non-phase-locked to the stimuli. The further analysis for estimating mean peak amplitudes of ERM components has been done in the same way as already discussed for approach A.

Before applying an EEMD decomposition, all signals were standardized to zero mean and unit variance (z-score). The following Figure 5.4 illustrates ERMs, obtained from a grand average of global ERPs, and their related Hilbert - Huang Transforms. Especially $ERM3 - ERM6$ show rather pronounced oscillations with stable frequencies (see the related Hilbert - Huang Transforms) ranging from $3\ [Hz] - 30\ [Hz]$ roughly. Thus these oscillations represent characteristic EEG bands like theta - or alpha - bands.
The intrinsic mode ERM5, as can be seen in Figure 5.4 and more clearly in Figure 5.5, most closely reflects the prominent ERPs of the raw data set. The latter corresponds to a grand average over 18 subjects of the signals recorded at all channels (see Figure 5.6).

5.1.3 The Studied ERP Components

Figure 5.6 illustrates a typical global ERP response, obtained as a grand average over all channels and over all subjects. Such a grand average ERP exhibits four prominent ERP peaks after stimulus onset, which will be denoted according their latencies as $P100, N200$, $P300$ and $N400$, respectively [96]. As can be seen, typically one observes a positive peak occurring roughly at 100 $[ms]$ (maximal response amplitude usually occurring between 70 $[ms]$ and 180 $[ms]$) after stimulus onset, called $P100$. This is followed by a negative peak, called $N200$, with maximal amplitude between 150 $[ms]$ and 260 $[ms]$). $P300$ identifies the next positive peak occurring usually between 270 $[ms]$ and 370 $[ms]$, followed by a late negative potential, denoted $N400$, at 370 $[ms]$ to 450 $[ms]$. Note that the Gabor stimuli last for almost $\Delta t_{st} = 200\ [ms]$ after stimulus onset t_0, hence encompasses $P100$ and part of $N200$.
In the grand average ERP, differences between stimulus conditions mostly appear for the early responses, i. e. for $P100$ and most notably for $N200$, $N400$, and seemingly also between 600 $[ms]$ and 800 $[ms]$. Mean amplitudes have been estimated therefore within intervals centered at these characteristic peaks.

5.1.4 Pooling of Electrodes

Our main objective is to investigate the contribution of each brain region in response to contour stimuli. In addition to that, it is important to determine a unique set of brain areas that generates scalp-recorded components of interest. Consequently, signals have been

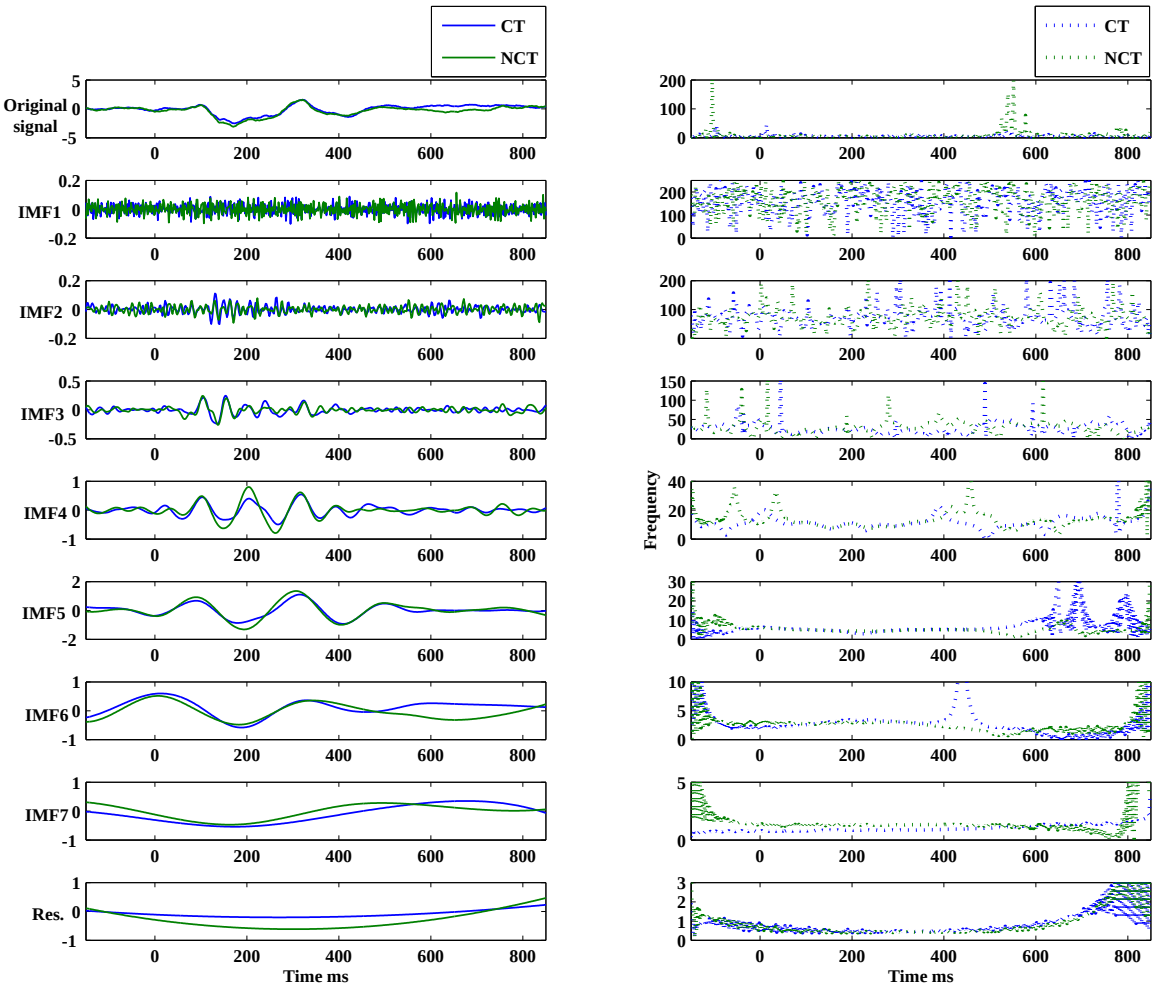

Figure 5.4 **EEMD decomposition on grand average ERPs.** Single subject ERPs were averaged over 18 subjects and are shown for two stimulus conditions: Contour and Non-contour. This signal is generated by averaging all signals from Figure 4.4 for the two conditions separately. Plots in the left column represent the averaged signal (on top) followed by its event-related intrinsic modes (ERMs). Plots in the right column present related Hilbert spectra for each of the corresponding ERMs in the left column.

pooled according to a clustering scheme proposed by Aftanas [2] which divides each hemisphere of the brain into six electrode clusters. This procedure led to six regional means for each hemisphere which were named according to their spatial positions: Anterior Temporal (AT), Frontal (FR), Central (CE), Parietotemporal (PT), Parietal (P), and Occipital (OC). The grouping of electrodes on the left and right hemispheres are depicted in Figure 5.7-Left. The difference on the latency of the peaks of global average ERPs related with the ERP components is clearly visible on the ERP averages of the pooled electrodes. Figure 5.8 illustrates that those peaks show an earlier response in the parietal -occipital regions (OC, P, PT) and later on the frontal regions (FR, AT). The differences in latencies of ERPs, corresponding to the pooled signals of the right hemisphere, are marked in Figure 5.8 by the straight lines.

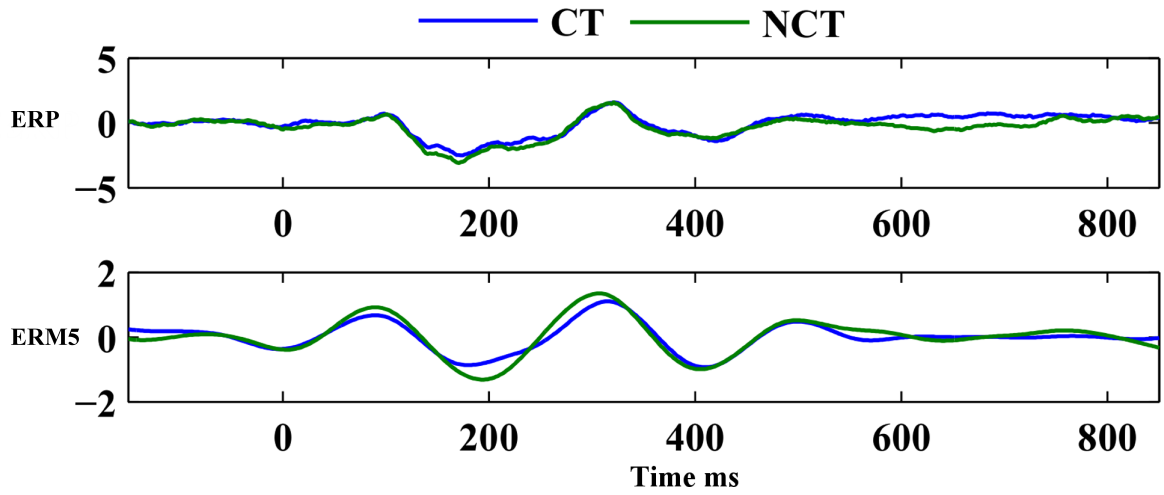

Figure 5.5 **ERP signal and its** *ERM5***.** Comparison of the original EEG recording (grand average over 18 subjects of all channels) with *ERM5*.

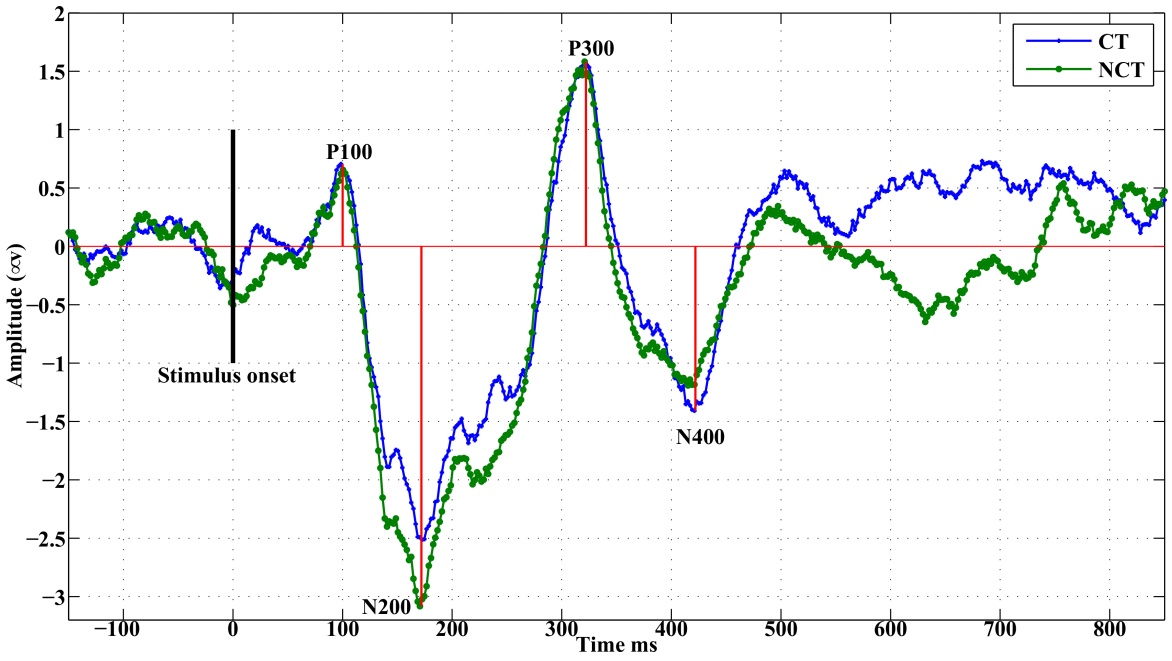

Figure 5.6 **Grand average ERPs, obtained as a result from averaging individual global ERPs from** 18 **subjects.** Such a grand average ERP exhibits four prominent ERP peaks after stimulus onset, which will be denoted according their latencies as $P100$, $N200$, $P300$ and $N400$, respectively.

By visual inspection, it can be seen that for the ERP $P100$, in the occipital brain area an early response occurs during the time interval 60 $[ms]$ – 120 $[ms]$ while in the frontal brain area the corresponding $P100$ peak shows up in the interval 120 $[ms]$ – 180 $[ms]$. Correspondingly,

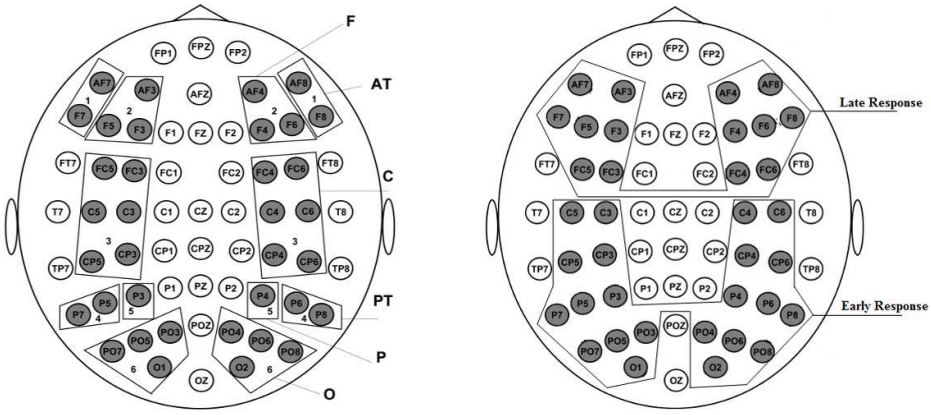

Figure 5.7 **Pooling schemes.** *Left*: Pooling of electrodes into 6 clusters according to a scheme proposed by [2]. *Right*: It shows the two groups of electrodes related with early and late responses.

for the ERP $N200$ two intervals were considered corresponding to an early response at $150\ [ms] - 210\ [ms]$ and a late response at $200\ [ms] - 260\ [ms]$, respectively.
However, the ERPs of the CE cluster clearly exhibits a double peak structure of the $N200$ ERP component showing early and late response components simultaneously. This is justified by the average of the two kind of signals, e.g, early and late responses. To determine the early and late response signals of electrodes, CE region was divided into three sub-regions: CE-R1 which consists of $FC3, FC5$ and $FC4, FC6$, CE-R2 consists of $C3, C5$ and $C4, C6$, and CE-R3 consists of $CP3, CP5$ and $CP4, CP6$ electrodes in the left and right hemisphere, respectively. Figure 5.9 illustrates that electrodes in the CE-R1 region show later response signals while electrodes in CE-R2 and CE-R3 regions present early response signals. Consequently, electrodes in CE cluster can be classified as early response signals for CE-R2 and CE-R3 regions while late response in CE-R1. Given the discussion above, electrodes have been grouped into early and late response signals as presented in Figure 5.7-Right.

5.2 Results

The following section will present results obtained from the EEMD analysis of EEG recordings of 18 subjects during a contour integration task. Results concerning raw data are presented at the level of event -related potentials (ERPs). Data is then decomposed with EEMD either using single trial recordings or ERPs.

5.2.1 Raw Data

As explained above, for the ERP $P100$ in the occipital brain area an early response occurs during the time interval $60\ [ms] - 120\ [ms]$ while in the frontal brain area the corresponding $P100$ peak shows up in the interval $120\ [ms] - 180\ [ms]$. Similarly, for the ERP $N200$ two intervals were considered corresponding to an early response at $150\ [ms] - 210\ [ms]$ and

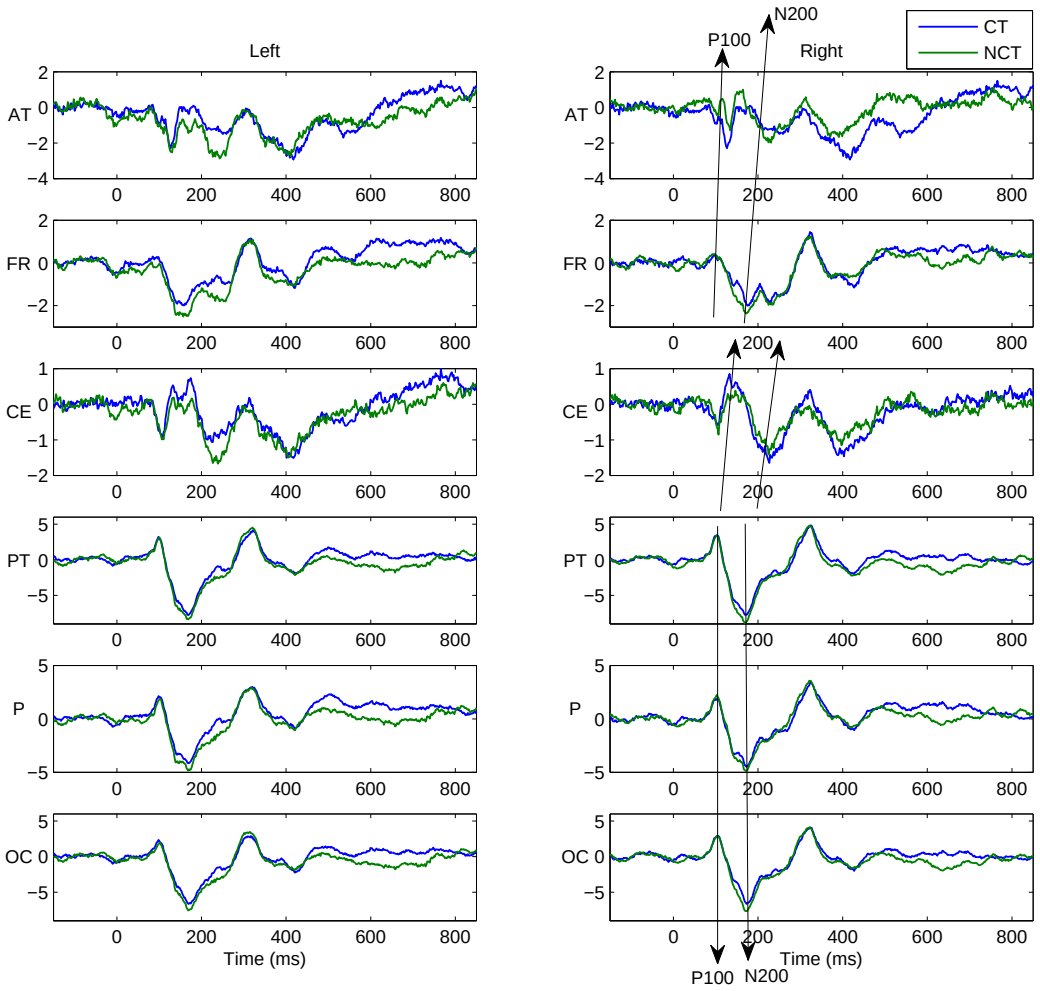

Figure 5.8 **The pooled ERPs responses.** The ERPs are averaged in pools of electrodes located on different regions.

a late response at 200 $[ms]$ – 260 $[ms]$, respectively. Next, the difference of the absolute values of these mean response amplitudes, estimated at each channel and for each stimulus condition, has been computed. Finally, these differences have been averaged over the population of 18 subjects. A paired t-test identified the channels with the most significant differences in signal responses. The resulting values have been used to generate corresponding head topographies as illustrated in Figures 5.10 and 5.11. The topograms (see Figure 5.10) illustrate early and late response differences resulting from mean response amplitudes around the ERP $P100$. Obviously, early as well as late response differences appear to be insignificant at a confidence level of $\alpha = 0.05$. On the contrary, early and late response differences estimated around the ERP $N200$ (see Figure 5.11) appear to be significant for the same confidence level. Early response differences are located in occipital areas of the brain, while late responses are found in frontal brain areas only. Additionally, such significant differences are detected only in the right hemisphere. Table 5.1 summarizes p - and

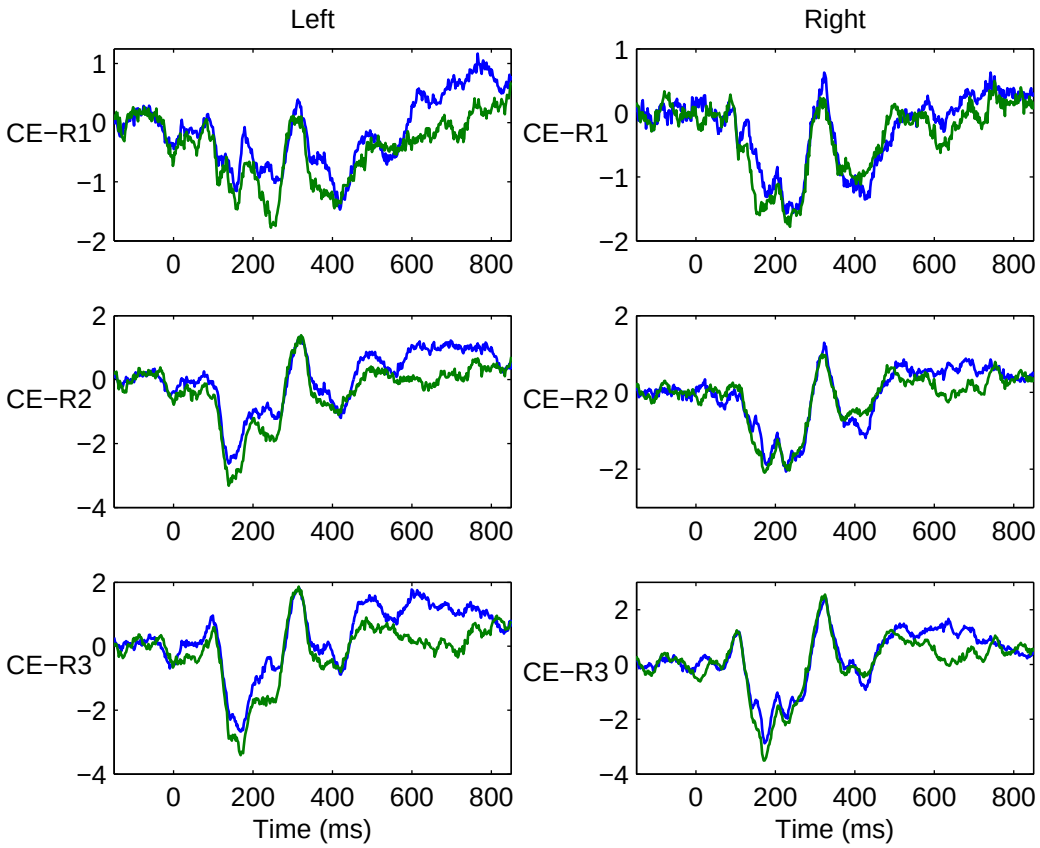

Figure 5.9 **The pooled ERPs responses of CE region divided into three sub-regions.** The ERPs are averaged in pools of electrodes located on different CE sub-regions.

T - values for significant early and late responses at various locations (channels) and for different confidence levels in case of ERP *N*200.

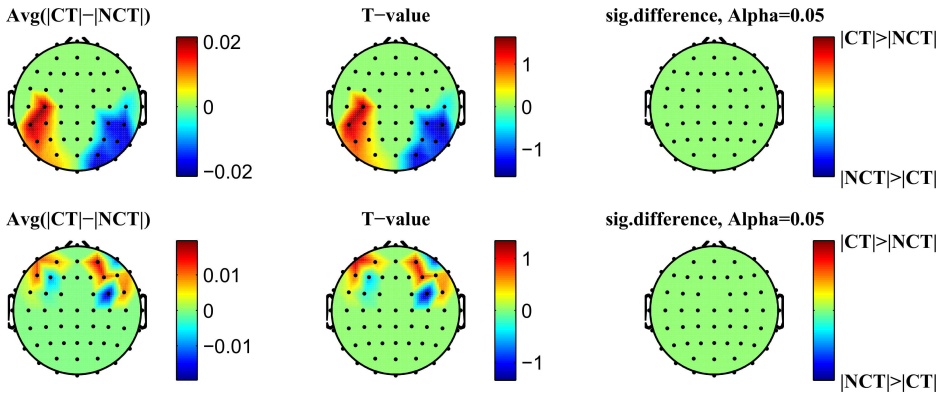

Figure 5.10 **Head topography of the significant difference of the** *P*100 **signals.** *Top*: Early response, *Bottom*: Late response

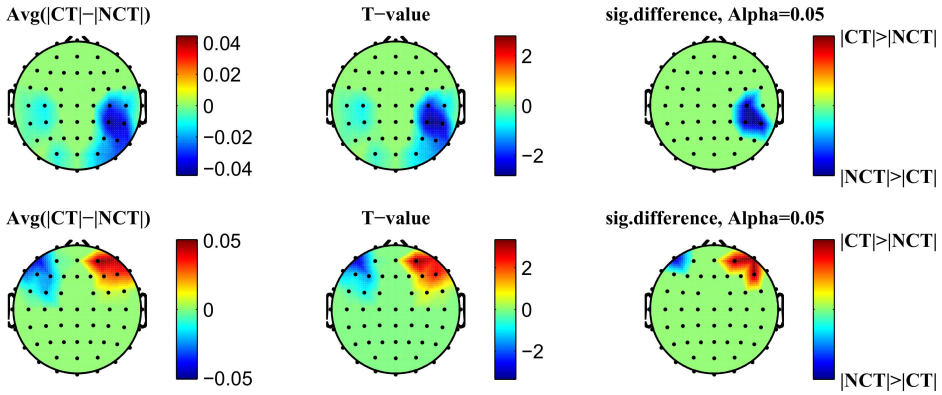

Figure 5.11 **Head topography of the significant difference of the** $N200$ **signals.** *Top*: Early response, *Bottom*: Late response

Table 5.1 **Test statistics for ERP** $N200$**.** Results of statistical tests of differences in mean ERP amplitudes for the event related potential $N200$ in early and late response areas. P - and T - values are reported for different significance levels: $(*) : \alpha = 0.05, (**) : \alpha = 0.01, (***) : \alpha = 0.001$

Early response			Late response		
p-value	T-value	Channel	p-value	T-value	Channel
0.042*	-2.199	C4	0.003**	3.417	AF4
0.015*	-2.720	CP6	0.022*	2.511	F6
0.012*	-2.830	CP4	0.005**	-3.255	AF7
			0.023*	2.500	AF8

5.2.2 ERMs

Approach A: EEMD after averaging over trials.

Averaging has been performed for each stimulus condition separately and EEMD decomposition was performed for each ERP signal. Then IMF (ERM) amplitudes have been estimated within intervals centered at the characteristic peaks of the corresponding ERMs, i. e. for $P100, N200$ etc. as was explained above. Again, a subsequent paired t-test identified the channels with the most significant differences in signal responses. The resulting values have been used to generate corresponding head topographies. The latter are very similar to the ones obtained by approach B, but show lower significance levels. These results are summarized in Table 5.2 and Table 5.3. As can be seen from Table 5.2, early responses have been observed only for channels located in the occipital and parietal areas of the brain, while a highly significant late response has been observed for a channel in the frontal area of the brain. A similar observation holds for the entries of Table 5.3. Significant early response differences are more numerous for the different $N200$ ERM components, while again only a single frontal channel exhibited a significant response difference. Note that even the original ERP shows significant late response differences for the $N200$ ERP component.

Table 5.2 **Approach A: Test statistics for $ERM4$ and $ERM5$ from $P100$.** The table summarizes parameters of the test statistics (p-value, T-value) for $ERM4$ and $ERM5$ extracted from the ERP $P100$. An EEMD has been applied after averaging over trials to extract ERMs. P- and T-values are given for different confidence levels: $(*) : \alpha = 0.05, (**) : \alpha = 0.01$.

	Early response			Late response		
ERM	**p-value**	**T-value**	**Channel**	**p-value**	**T-value**	**Channel**
ERM 4	0.046*	-2.155	C6			
ERM 5	0.009**	-2.969	P8	0.002**	3.747	F4
	0.025*	-2.460	CP6			
	0.036*	-2.276	P6			

Table 5.3 **Approach A: Test statistics for $ERM5, ERM6$ and $ERM7$ from $N200$.** The table summarizes parameters of the test statistics for $ERM5$, $ERM6$ and $ERM7$ extracted from the $N200$ ERP. An EEMD has been applied after averaging over trials to extract ERMs. P- and T-values are given for different confidence levels: $(*) : \alpha = 0.05, (**) : \alpha = 0.01$.

	Early response			Late response		
ERM	**p-value**	**T-value**	**Channel**	**p-value**	**T-value**	**Channel**
ERM 5	0.010*	-2.884	P4	0.026*	2.438	F4
	0.008**	-3.034	P8			
	0.003**	-3.552	CP6			
	0.013*	-2.784	CP4			
	0.015*	-2.693	P6			
ERM 6	0.040*	-2.226	CP6			
	0.047*	-2.141	CP3			
ERM 7	0.008**	2.998	O1			
	0.002**	3.613	P7			

Approach B: EEMD before averaging over trials.

Approach B consisted in performing an EEMD of all single trial signals separately. Then an average over trials has been performed for each IMF, each stimulus condition and each channel, resulting in corresponding ERMs. The further analysis for estimating mean peak amplitudes of ERM components has been done in the same way as already discussed for approach A. Figure 5.12 illustrates differences in early $P100$ responses for both stimulus conditions. The top row presents on the right the component $ERM5$ for both stimulus conditions. It represents an average over all channels which exhibit a significant response difference at a confidence level of $\alpha = 0.05$. On the left, the corresponding raw signal is presented for comparison. In the component $ERM5$, clear differences are seen in response amplitude for both stimulus conditions. In the bottom row, the topography resulting from differences in $ERM5$ amplitudes related to the ERP $P100$ at a significance level of $\alpha = 0.05$ is shown. The rightmost topogram exhibits those brain regions where significant signal differences could be detected. As can be seen, early responses are localized in occipital and parietal areas of the right brain hemisphere only. There, the amplitude of the $P100$ component of $ERM5$ is larger for the stimulus condition NCT than for condition CT (see Figure 5.12). Furthermore, remember that for the raw $P100$ ERPs (Figure 5.12, top left) no statistically significant differences in response amplitude could be found. Note that the $P100$ peak maximum, both in

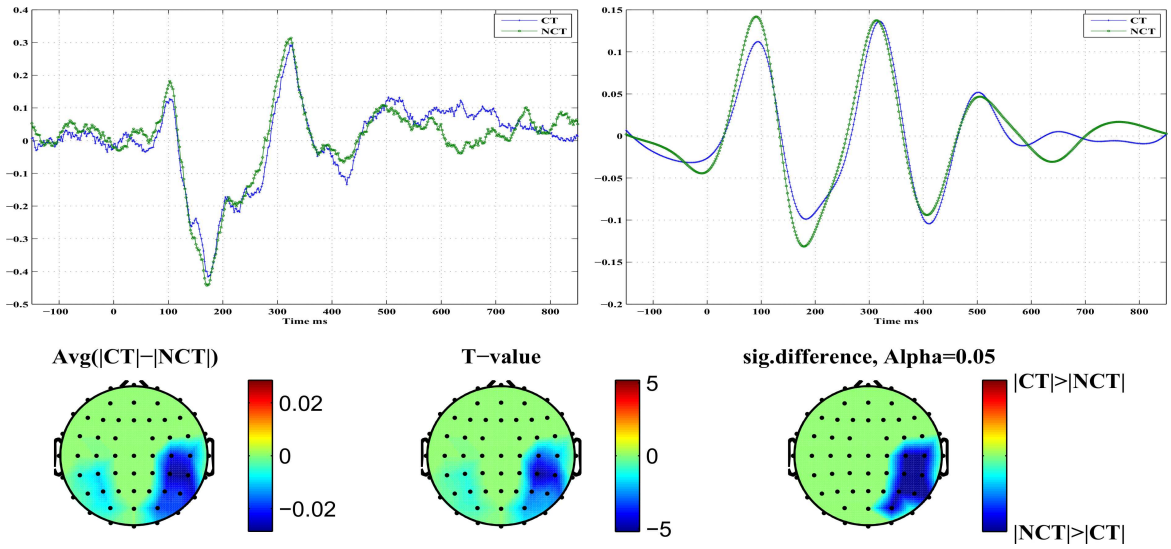

Figure 5.12 **Early stimulus response at ERP** *P*100**.** *Top Left*: Standardized original ERPs for both stimulus conditions. *Top Right*: *ERM*5 for both stimulus conditions. *Bottom*: Head topographies showing locations of significant differences in *ERM*5 amplitudes for both stimulus conditions.

the raw signal as well as in the *ERM*5, occurs shortly before $t = 100\ [ms]$, hence represents what we call an *early* stimulus response.
Figure 5.13 illustrates differences in what we call *late* *P*100 responses for both stimulus conditions. The top row presents to the right the component *ERM*5 for both stimulus conditions. It represents an average over all channels which exhibit a significant response difference at a confidence level of $\alpha = 0.05$. On the left, the corresponding raw signal is presented for comparison. In the component *ERM*5, the differences in response amplitude for both stimulus conditions are even more pronounced than in case of the early response. On the left, an average of the raw signals of all those channels which exhibit significant response differences is shown. In the bottom row the topography resulting from differences in *ERM*5 amplitudes measured for the ERP *P*100 at a significance level of $\alpha = 0.05$. The rightmost topogram exhibits those brain regions where significant signal differences could be detected. As can be seen, late responses are localized in frontal and medio-temporal areas in the right hemisphere only. There the *ERM*5 amplitude for the stimulus condition CT is larger than for condition NCT (see Figure 5.13) contrary to what has been observed for the early *P*100 response in occipital areas. Note that the peak maximum occurs roughly at $t \simeq 150\ [ms]$. Again for the raw *P*100 ERP signal, no statistically significant differences between both stimulus conditions could be found. Table 5.4 summarizes, for approach B and the *P*100 ERP, parameters (p- and T-values) of the test statistics for *ERM*4 and *ERM*5 at different confidence levels. Note that an early response has been observed only for channels located in the occipital and parietal areas of the brain, while a late response is observed for a channel in the frontal area of the brain.

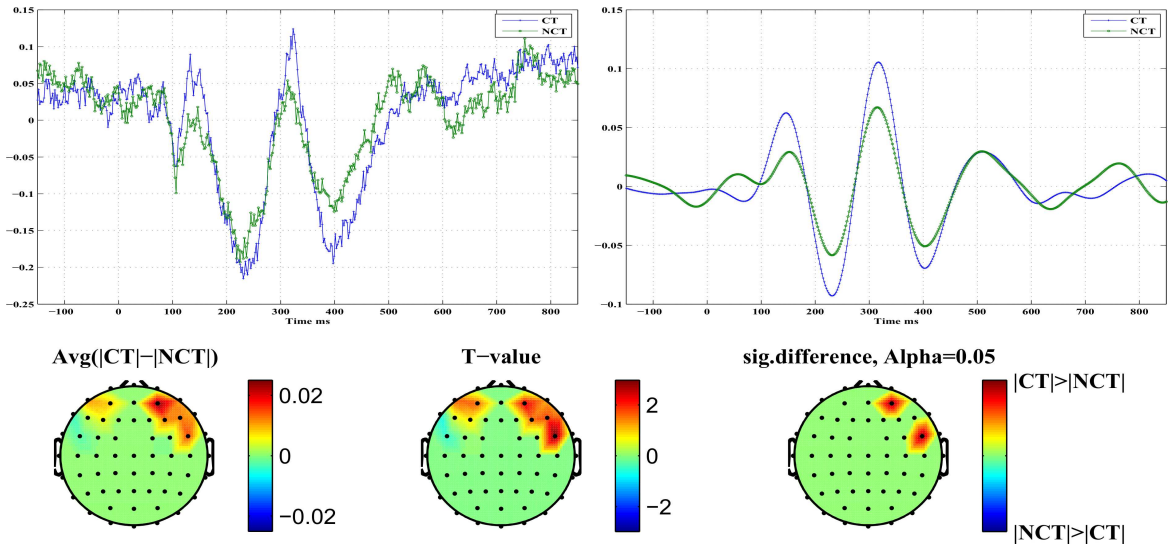

Figure 5.13 **Late stimulus response at ERP** *P*100**.** *Top Left*: Standardized original ERPs for both stimulus conditions. *Top Right*: *ERM*5 for both stimulus conditions. *Bottom*: Head topographies showing locations of significant differences in *ERM*5 amplitudes for both stimulus conditions.

Table 5.4 **Approach B: Test statistics for** *ERM*4 **and** *ERM*5 **from** *P*100**.** The table summarizes parameters of the test statistics (p-value, T-value) for *ERM*4 and *ERM*5 extracted from the ERP *P*100. An EEMD has been applied *before* averaging over trials. P- and T-values are given for different confidence levels: $(*) : \alpha = 0.05, (**) : \alpha = 0.01, (***) : \alpha = 0.001$.

	Early response			Late response		
ERM	**p-value**	**T-value**	**Channel**	**p-value**	**T-value**	**Channel**
ERM 4	0.015*	-2.705	O2	0.025*	2.464	F3
	0.038*	-2.256	CP6	0.015*	2.695	F5
ERM 5	0.004**	-3.329	C4	0.006**	3.124	FC6
	0.009**	-2.902	P4	0.031*	2.354	AF4
	0.009**	-2.906	P8			
	0.000***	-4.384	CP6			
	0.000***	-5.311	CP4			
	0.031*	-2.345	PO4			
	0.049*	-2.123	C6			
	0.027*	-2.416	P6			

Figure 5.14 illustrates differences in early *N*200 responses for both stimulus conditions. The top row presents on the right the component *ERM*5 for both stimulus conditions. It represents an average over all channels which exhibit a significant response difference at a confidence level of $\alpha = 0.05$. On the left, the corresponding raw signal is presented for comparison. In the component *ERM*5, differences in response amplitude for both stimulus conditions are seen clearly. On the left, an average of the raw signals of all those channels which exhibit significant response differences is shown. The bottom row shows the topography resulting from differences in *ERM*5 amplitudes measured for the ERP *N*200 at a significance level of $\alpha = 0.05$. The rightmost topogram exhibits those brain regions

where significant signal differences could be detected. As can be seen, early responses are localized in occipital and parietal areas in the right hemisphere mainly but also in the left hemisphere, contrary to the $P100$ response. In the indicated brain areas, the $ERM5$ amplitude for the stimulus condition NCT is again larger than for condition CT (see Figure 5.14). Note that the negative peak occurs shortly before $t = 200\ [ms]$ and exhibits a clear shoulder shortly after $t = 200\ [ms]$.

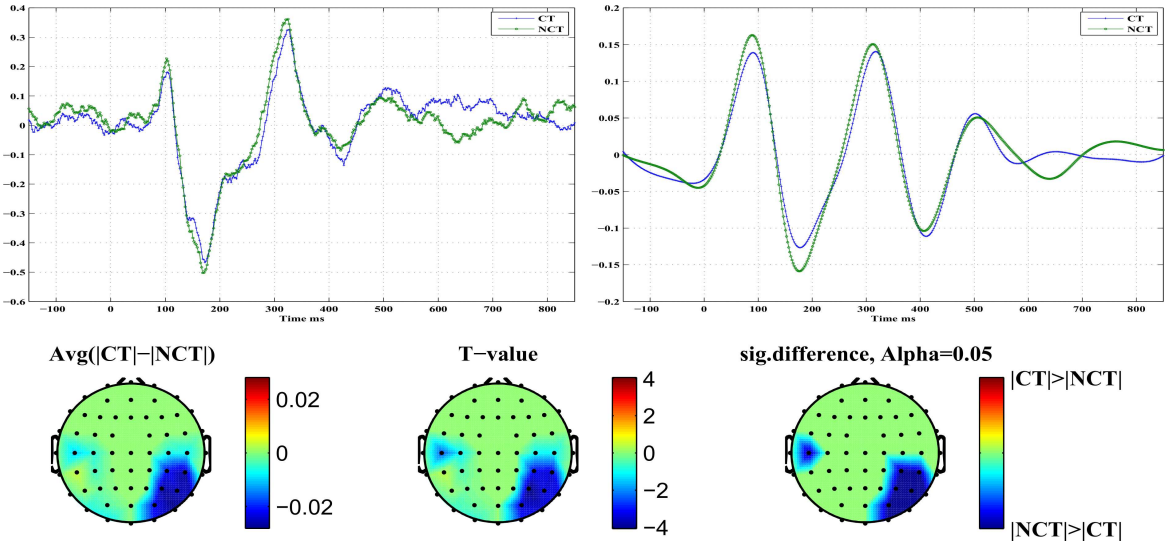

Figure 5.14 **Early stimulus response at ERP** $N200$**.** *Top Left*: Standardized original ERPs for both stimulus conditions. *Top Right*: $ERM5$ for both stimulus conditions. *Bottom*: Head topographies showing locations of significant differences in $ERM5$ amplitudes for both stimulus conditions.

Figure 5.15 illustrates differences in late $N200$ responses for both stimulus conditions. The top row presents on the right the component $ERM5$ for both stimulus conditions. It represents an average over all channels which exhibit a significant response difference at a confidence level of $\alpha = 0.05$. On the left, the corresponding raw signal is presented for comparison. In the component $ERM5$, again very pronounced differences are seen in response amplitude for both stimulus conditions. The bottom row shows the topography resulting from differences in $ERM5$ amplitudes measured for the ERP $N200$ at a significance level of $\alpha = 0.05$. The rightmost topogram exhibits those brain regions where significant signal differences could be detected. As can be seen, late responses are localized in frontal and medio-temporal areas in the right hemisphere only. There the $ERM5$ amplitude for the stimulus condition CT is again larger than for condition NCT. Note that for the late response, the negative peak occurs shortly after $t = 200\ [ms]$. Table 5.5 summarizes, for approach B and the $N200$ ERP component, parameters (p- and T-values) of the test statistics for $ERM5 - ERM7$ at different confidence levels. Early responses were obtained again from channels in the occipital and parietal regions of the brain, while late responses were located at channels in frontal regions. Note that the difference between early and late responses is most clearly shown in $ERM5$.

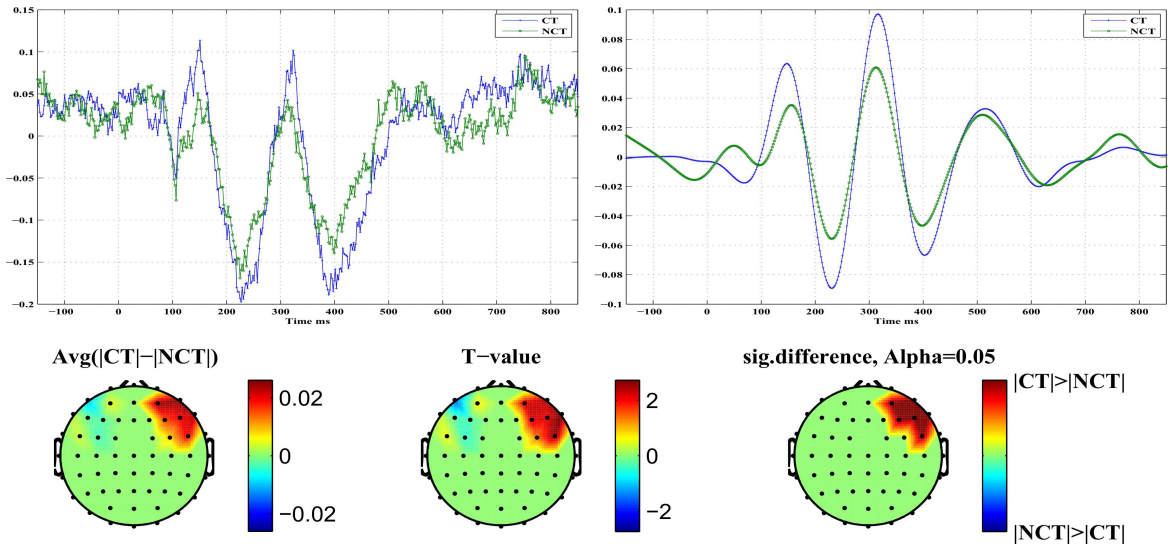

Figure 5.15 **Late stimulus response at ERP** *N*200**.** *Top Left*: Standardized original ERPs for both stimulus conditions. *Top Right*: *ERM*5 for both stimulus conditions. *Bottom*: Head topographies showing locations of significant differences in *ERM*5 amplitudes for both stimulus conditions.

The *ERM*5 is the mode that consistently has peaks with latencies similar to the studied ERP components. Concerning the component *P*100 of the mode *ERM*5, an early response is manifest on electrodes located in the occipital and parietal brain areas with a stronger response amplitude for the NCT - stimulus condition. On the contrary, a late *P*100 response is clearly detected in frontal brain areas with a larger response amplitude for the CT - stimulus condition. The delay of the late *P*100 response component amounts to $\Delta t \approx 70\ [ms] \pm 10\ [ms]$. Furthermore, the response differences appear much more pronounced for the late *P*100 response compared to the early *P*100. A remarkable detail is seen in the *P*100 response for the NCT - stimulus condition. The *P*100 peak corresponding to the NCT - condition, which is visible in the early response (see Figure 5.12, top right), splits in the late response (see Figure 5.13, bottom right) into a double peak with one component at a time of occurrence of the early *P*100 response, and a later *P*100 response, peaking roughly 70 $[ms]$ after the early response. This detail is only visible for the stimulus condition NCT and is absent for the CT - stimulus. The latter only shows the delayed component. Related head topographies indicate the brain areas where statistically significant response differences could be detected. They consistently indicate such differences only for the right hemisphere in broad agreement with recent findings about a right hemisphere specialization of contour integration [214]. They appear more focused in frontal areas while they are more diffuse and spatially extended in occipital, parietal and parieto-temporal areas for the early responses. Clearly, occipital as well as frontal areas are involved in contour integration as early as for the *P*100 response but most notably at the *N*200 level. This seems to support assertions of a top-down control in contour integration [217].

Table 5.5 **Approach B: Test statistics for** $ERM5, ERM6$ **and** $ERM7$ **from** $N200$**.** The table summarizes parameters of the test statistics for $ERM5$, $ERM6$ and $ERM7$ extracted from the ERP $N200$. An EEMD has been applied *before* averaging over trials. P- and T-values are given for different confidence levels: $(*) : \alpha = 0.05, (**) : \alpha = 0.01$.

	Early response			Late response		
ERM	**p-value**	**T-value**	**Channel**	**p-value**	**T-value**	**Channel**
ERM 5	0.001***	-4.148	P4	0.040*	2.222	F4
	0.009**	-2.927	O2	0.014*	2.753	F8
	0.004**	-3.359	P8	0.015*	2.692	FC6
	0.003**	-3.470	CP6	0.039*	2.235	AF4
	0.005**	-3.225	CP4	0.048*	2.132	F6
	0.003**	-3.541	PO4	0.033*	2.329	AF8
	0.026*	-2.442	C5			
	0.003**	-3.440	P6			
	0.003**	-3.465	PO8			
ERM 6	0.032*	-2.339	C3	0.005**	-3.257	F8
	0.009**	-2.931	P7	0.008**	-2.991	FC4
	0.014*	-2.725	CP5			
	0.029*	-2.387	CP4			
	0.006**	-3.114	PO3			
	0.033*	-2.321	P5			
	0.036*	-2.275	P6			
	0.033*	-2.327	PO7			
ERM 7	0.030*	2.374	P3	0.042*	2.204	FC5
	0.010*	2.891	P4			
	0.014*	2.753	O1			
	0.046*	2.155	O2			
	0.014*	2.753	CP5			
	0.008**	2.981	PO3			
	0.022*	2.533	P5			
	0.002**	3.657	PO7			

Similar results are obtained for the $N200$ response. An early $N200$ response prominently appears *before* $t = 200\ [ms]$, while a late $N200$ response is peaking *after* $t = 200\ [ms]$. The response amplitude in the early phase is again larger, i. e. more negative, for the NCT - stimulus condition, while it is weaker in the late phase of the response. Once again, the response difference is more pronounced for the late response. Remarkably, the $N200$ response contour for the early CT - stimulus response exhibits a shoulder at the time where the late $N200$ response amplitude peaks. However, no clear double peak structure appears as for the $P100$ CT - stimulus response. If one compares the $ERM5$ signal structure related to the different electrodes located on a path from occipital to frontal, a clear shift in the time of occurrence of the $N200$ peak from early to late is seen. Thus single *ERMs* allow to follow a precise timing of the $N200$ ERP along the visual processing pathway.

5.3 Discussion

In the study, we presented EEG recordings from 18 subjects which were participating in a perceptual learning task. More specifically, subjects were presented with Gabor stimuli which occasionally formed an open continuous contour. Subjects were asked to indicate the

presence (CT) or absence (NCT) of such contours in their visual field at certain time points. After proper pre-processing, raw data have been averaged over all trials to extract event related potentials (ERPs) at every electrode. A global average of such ERPs is illustrated for all 18 subjects in Figure 4.4. Clearly, there is a large biological variability in the data with mostly little difference between both stimulus conditions. Note that data have been individually standardized to zero mean and unit variance. Relative differences between both stimulus conditions have been preserved that way. Figure 5.6 presents a grand average of individual global ERPs, indicating most clearly four prominent peaks named $P100$, $N200$, $P300$ and $N400$. This grand average suggests that differences in response amplitudes between both stimulus conditions are most probably to be expected at the early ERPs, i. e. at $P100$ and $N200$. But a statistical testing of observed differences in response amplitudes to both stimulus conditions could not proof any significant difference in the $P100$ ERP amplitudes at a significance level of $\alpha = 0.05$ corresponding to $T \geq 2.1$ (see Figure 5.10). For the $N200$ ERP response amplitudes, at the same significance level, statistically significant differences could be found at several electrodes mainly located in the occipital and parietal areas of the brain but also in frontal brain areas. Interestingly, response amplitudes peaked *before* $t = 200\ [ms]$ in the occipital and parietal areas but showed a late response *after* $t = 200\ [ms]$ for the frontal electrodes. Henceforth, these responses are called early and late responses, respectively. Early and late responses show a delay of roughly $\Delta t = 100\ [ms]$ and correlate well with electrode locations in either the occipital or frontal brain areas.

This rough analysis of raw ERP signals has been improved by applying a signal decomposition technique based on an ensemble empirical mode decomposition (EEMD) as proposed by Huang et al. [80][236][237]. The analysis has been performed in two different ways: either EEMD has been applied *before* or *after* averaging over trials. The resulting component signals extracted have been called event related modes (ERMs). EEMD before averaging delivered better results with respect to statistical measures, probably because of unfavorable signal compensations through averaging. Hence, only these results have been presented in detail. For illustrative purposes only, Figure 5.4 presents a grand average EEG signal extending from 150 $[ms]$ before stimulus onset at $t_0 = 0$ to 850 $[ms]$ after t_0. While the original signals exhibit only small differences, mainly around ERP $N200$, some of the extracted ERMs indicate clear differences between both stimulus conditions. The related Hilbert - Huang spectra indicate decent regularities in these ERMs with characteristic frequencies which stay largely constant over the time span considered. Most notable differences are seen for $ERM3, ERM4, ERM5$ and $ERM6$. For example, $ERM3$ shows a dominant frequency around $\nu = 25\ [Hz]$, corresponding to the β - band, $ERM4$ shows oscillations around $\nu = 10\ [Hz]$ which represents an α - activity, $ERM5$ oscillates with roughly $\nu = 5\ [Hz]$ indicating a θ - wave and, finally, $ERM6$ is dominated by an oscillation with $\nu \leq 2\ [Hz]$ corresponding to a δ - wave. $ERM2$ is indicative of some high frequency ($\nu \geq 30\ [Hz]$) activity which might contain γ - wave activities. Note that these spectral characteristics agree between both stimulus conditions.

Even further insight is provided from ERMs resulting from an EEMD application to the single trial signals. The resulting intrinsic mode functions (IMFs) have then been averaged over all trials to result in corresponding ERMs. The largest differences between stimulus

conditions are seen for $ERM4-ERM6$, i. e. in the $\alpha-, \theta-$ and δ - bands, around $P100$ and $N200$. A general characteristic of the ERP components is that a clear transition from an early response to a late response is observable which exhibits a strong correlation to a spatial representation of the stimulus response either in the occipital or the frontal brain areas. Central brain areas show signs of both, early and late responses. The electrodes, where either the early or the late response could be observed, are shown in Figure 5.7-Right. While studying the switching between early and late responses in more detail, signals have been pooled according to a clustering scheme proposed by [2] which divides each hemisphere into six electrode clusters as shown in Figure 5.7-Left. The difference on the latency of the peaks of $ERM5$ related with the ERP components is clearly visible on the ERM averages of the pooled electrodes. Figure 5.16 illustrates that those peaks show an earlier response in the parietal -occipital regions (OC, P, PT) and later on the frontal regions (FR, AT). The differences in latencies of $ERM5$, corresponding to the pooled signals of the right hemisphere, are marked in Figure 5.16 by the straight lines. Similar differences are observed in the left hemisphere though supported by a smaller statistical significance between the conditions (see Tables 5.4 and 5.5). However, the $ERM5$ of the CE cluster clearly exhibits a double peak structure of the $N200$ ERP component showing early and late response components simultaneously. This is justified by the average of the two kinds of signals, e.g, early and late responses. Surprisingly, the pooled $ERM5$ of the frontal region shows a similar double peak structure for the ERP component $P100$.

Because the human head is a volume conductor, the peaks in the ERP and ERM amplitudes observed at frontal and occipital electrodes do not necessarily imply that the brain activity was generated within frontal and occipital sources, respectively. However, a change in topography as seen from the earlier to the later phases of the $P100$ and $N200$ peaks clearly indicates different distributions of neural activity in each phase [116][147]. Thus, the data favor the view that contour processing involves activity within distributed brain networks, rather than focal activity within the lower visual cortex [66]. This notion is broadly compatible with results from recent EEG or combined EEG and fMRI investigations [216][141][73]. On contrast to previous studies, we used a data-driven approach for EEG signal decomposition. The findings thus give an independent proof that contour integration depends on distributed network activity.

The time and frequency ranges where differences between stimulus conditions occurred are comparable to those of previous studies on oscillatory brain responses during contour integration. We found the strongest differences at parietal and occipital sites occurring $< 200ms$ after stimulus onset and in low-to-mid frequencies [217][216][206]. A prominent role for beta oscillations in contour integration, as observed in our previous studies, did not show up in the data. Note, however, that a transient increase in beta power would not necessarily lead to increased amplitudes within one specific ERM. An ERM-based analysis or the EEG is thus not well-suited for validating the results of previous Fourier-based analyses.

In this study we used exclusively Gabor arrays as visual stimuli. It could thus be objected that the results are not specific for contour integration, but reflect some general visual processes under conditions of low stimulus visibility. Indeed, a recent fMRI study revealed that brain activity in visual as well as prefrontal areas increased with the presentation duration

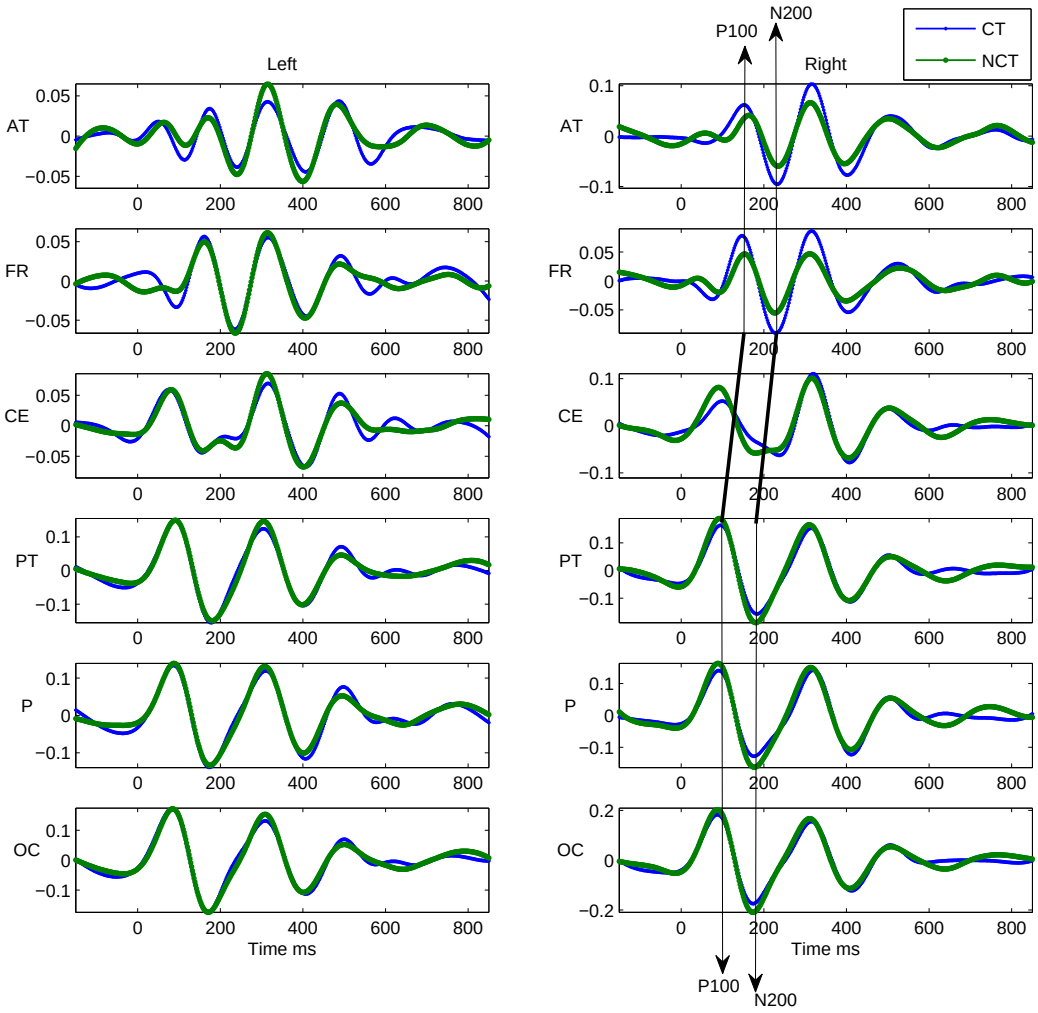

Figure 5.16 **The pooled** *ERM5* **responses.** The *ERM5* are averaged in pools of electrodes located on different regions.

and so with the visibility of shortly presented gratings [87]. The role of the frontal cortex in this and in our study is yet unclear. Previous authors argue that frontal cortical activity is related to a conscious visual experience or to post-perceptual processes like motor preparation [46][14]. On the other hand, the frontal cortex can also be directly involved into the actual stimulus processing [87]. The fact that posterior and frontal activity differences between contour and non-contour conditions occurred very early during processing is more in line with the latter interpretation.
Thus, it seems warranted to conclude that the observed differences in brain activity originate from contour processing per se.

Chapter 6

Inverse Modeling of the EEG Data based on EEMD

Solving the EEG forward problem includes building an electromagnetic model of the subject's head. Once this is done, one can try to identify neural sources by solving the inverse problem. The inverse problem is basically an optimization problem, where the procedure is to work backwards from the scalp recordings in order to locate the current dipoles which best explain the recorded EEG. In this chapter, we propose, for the first time, to combine an EEMD analysis with a source localization scheme, more specifically an sLORETA source estimation. We investigate whether an EEMD analysis can provide underlying characteristic modes which, when fed into an sLORETA analysis, can help to localize sources of neuronal activity reflecting cognitive processing during the contour integration task, employing CT (contour true) and NCT (non-contour true) stimuli. Hence, measured EEG responses are subjected to mode decomposition techniques, more specifically to an EEMD, and sLORETA is applied to the event - related modes (ERMs) extracted to solve the source imaging problem. Although a wealth of source localization procedures meanwhile exist [67][76][21][74][89][45], we considered sLORETA because of its straightforward implementation and its good performance in real applications [159]. As a reminder, the experimental paradigm used in our study was a contour integration task, applied to a group of 18 probands and 300 trials each. A large set of Gabor stimuli was presented repeatedly which occasionally contained a contour made up by a subset of collinearly oriented Gabor patches. The participants had to signal the perception of contour or non-contour stimuli with a manual response. Similarly to the forward modeling in Chapter 5, brain electrodes have been distinguished according to the timing of their stimulus response. Early responses were recorded at electrodes localized in the occipital and parietal areas of the brain, while late responses were located in frontal and medio-temporal areas of the brain. Early and late responses, manifested in ERP components $P100$ and $N200$, turned out most discriminative in detecting significant response differences to contour and non- contour stimuli. These components represent the first and second prominent ERP peaks with latencies of roughly 100 $[ms]$ and 200 $[ms]$ after stimulus onset. It has been shown in [10] that the event-related modes ERM5 most closely reflected the dominant oscillation of the grand average EEGs of the various subjects.

6.1 Results

The following section will present results obtained from a combined EEMD-sLORETA analysis of EEG recordings from 18 subjects during a contour integration task. Results related to raw data are presented at the level of event-related potentials (ERPs). Raw data is then decomposed with EEMD using single trial recordings. Based on the analysis of Chapter 5, source localization results obtained with raw data are compared with results obtained from the most informative event-related mode $ERM5$. As can be seen in Figure 5.5, the intrinsic mode ERM5 most closely reflects the prominent ERPs of the raw data set. The latter corresponds to a grand average over 18 subjects over all channels. Within each average time series, the two most prominent potentials of each ERM, denoted, according to their related ERPs and their latencies after stimulus onset, as $P100$ (positive response roughly $100[ms]$ after stimulus onset) and $N200$ (negative response roughly $200[ms]$ after stimulus onset), will be considered. These response amplitudes were most clearly seen in ERM5 and showed statistically significant differences in response to contour versus non-contour Gabor stimuli. The EEMD analysis further revealed a delay which amounts to $70[ms]$ when comparing response latencies at occipital and frontal brain areas. Early $P100$ and $N200$ responses occurred at electrodes located in the occipital, parietal and parieto-temporal areas of the brain, while late $P100$ and $N200$ responses appeared at electrodes located in frontal and fronto-temporal brain areas. The same potentials, when appearing at electrodes in central brain areas, showed bimodal early/late response signatures. Note that ERPs have been pooled as illustrated in Figure 5.7-Right. Note further that the potentials $P300$ and $N400$ did not show any difference in latencies between early and late responses. A statistical paired T -test of differences in reconstructed response amplitudes to both stimulus conditions resulted in a series of paired T-test values. The latter served to compare, between the two stimulus conditions, CT and NCT, and for selected latencies, the response amplitudes which were reconstructed, employing sLORETA, from both the ERP and the intrinsic mode $ERM5$.
This section is concerned with estimating the localization of the spatial sources related to these ERPs in the raw data as well as in the ERMs. For simplicity we confine our discussion to potentials appearing in mode $ERM5$. The inverse problem was solved by employing the sLORETA software package [156]. The related sLORETA values according to the Brodmann area (BA) per brain map are given for the sources identified.

6.1.1 Early Response

6.1.1.1 ERP component P100 at 60-120 [ms]

Figure 6.1 illustrates results of an sLORETA analysis of response differences in early stimulus responses for both stimulus conditions. Mean response amplitudes have been estimated for the interval $60-120$ $[ms]$ around the ERP $P100$ peak. Shown are significant paired t-test values for the differences, for both stimulus conditions, of potential readings from all 62 electrodes, as shown in Figure 5.7-Right, have been used as entries to the data matrix Φ. The graphic illustrates significant differences for the raw ERP Figure 6.1-Top and the mode

*ERM*5 Figure 6.1-Bottom. Blue and red colors thereby indicate negative or positive paired t-test values, respectively.
As can be seen in Figure 6.1-Top, differences of the raw ERP appear in the occipital and parietal brain areas of the left hemisphere at a significance level of $\alpha = 0.01$. Also some weaker positive activity differences are detected in the temporal regions of the both hemispheres at significance level $\alpha = 0.05$.

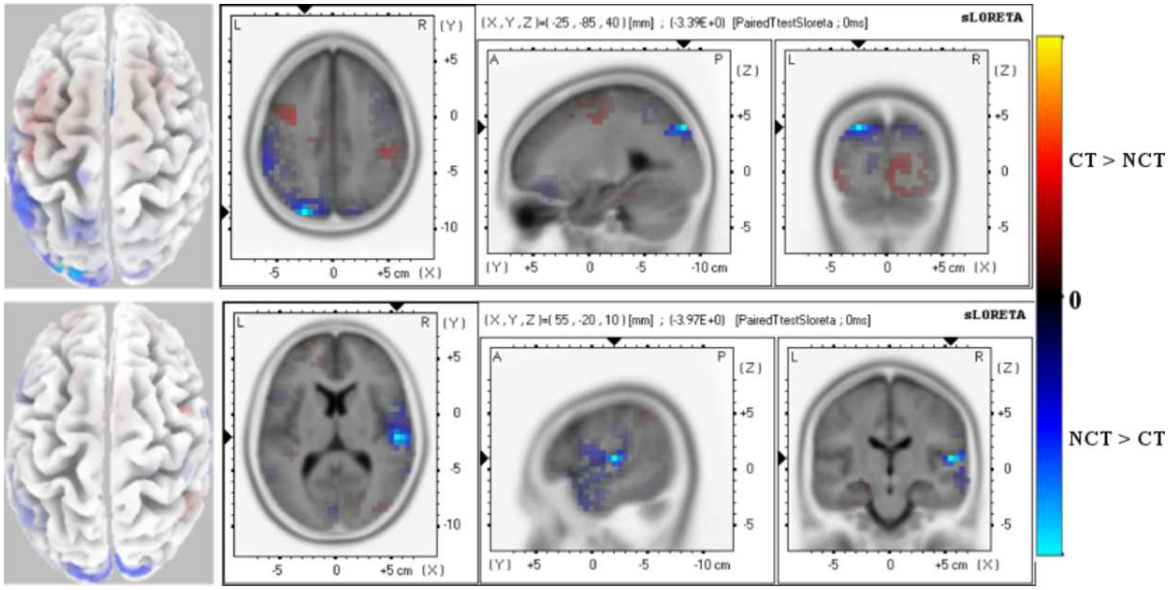

Figure 6.1 **Early Response (60-120 ms) P100 ERP.** Paired t-test values of significant potential amplitude differences at electrodes are illustrated at a significance level as specified. Views are axial, saggital and coronal. The left column shows the distribution on the scalp. All 62 electrodes were used as entries to the data matrix Φ. *(Top):* Raw ERP $P100$ with significance level $\alpha = 0.01$. *(Bottom):* ERM5 extracted from the ERP $P100$ with significance level $\alpha = 0.001$. Red color (positive paired T-test values) indicates that the ERP amplitude for the stimulus condition CT is larger than for condition NCT while blue color (negative paired T-test values) indicates that the ERP amplitude for the stimulus condition NCT is larger than for condition CT .

These results should be contrasted to those obtained from studying the mode $ERM5$ $P100$ of the EEMD analysis as it appears in the ERP potential. The most noticeable difference is that $ERM5$ shows highly localized, significant differences mainly in the temporal, occipital and parietal regions. There, the amplitude of the early $P100$ component of $ERM5$ is larger for the stimulus condition NCT than for condition CT. The highest differences appear in the temporal lobe at significance level $\alpha = 0.001$. Table 6.1 illustrates the significant differences results of the early $P100$ response of raw ERP and mode $ERM5$, respectively, in detail. The table summarizes the Brodmann areas (BA), MNI coordinates and the neuroanatomical lobe of the voxels for the $P100$ early response that showed statistically the most significant differences of Brodmann area clusters.

Table 6.1 **T-test statistics for early *P100* ERP and *ERM5* response**. The table shows coordinates of the most significant voxel of clusters. The sign of T-test values indicates the differences between stimuli ($'-'NCT > CT, '+'CT > NCT$). T-values are given for different confidence levels: $(*) : \alpha = 0.01, (**) : \alpha = 0.001$.

		ERP				
X	Y	Z	T-value	Voxels-No	BA	Brain Lobe
-25	-85	40	-3.39	14	19*	Parietal
5	15	25	-3.17	8	24*	Limbic
		ERM5				
X	Y	Z	T-value	Voxels-No	BA	Brain Lobe
55	-20	10	-3.97	21	(41**,22*,42*)	Temporal
10	-90	25	-3.15	79	(18*,19*)	Occipital
-20	-80	35	-3.01	18	(19*,40*)	Parietal

6.1.1.2 ERP component N200 at 150-210 [ms]

Next, Figure 6.2 illustrates paired t-test values for the ERP $N200$ as resulting from an analysis of the raw data Figure 6.2-Top and the mode $ERM5$ Figure 6.2-Bottom. Shown are significant differences in early stimulus responses. $N200$ early response differences of ERP $N200$ are mainly located in limbic lobe and parietal regions of the left hemisphere with significance level $\alpha = 0.001$. There are also significant differences in the frontal and occipital regions at confidence level $\alpha = 0.01$. Comparing these results with the outcome of an analysis of mode $ERM5$, a much more focused significant difference in response activities to both stimulus conditions is located in the parietal and occipital cortexes of both hemispheres at a confidence level of $\alpha = 0.001$. Some positive activity differences also show up in frontal areas of the right hemisphere where the amplitude of the early $N200$ component of $ERM5$ is larger for the stimulus condition CT than for condition NCT.
These results of early $N200$ response of raw ERP and mode $ERM5$ are summarized in Table 6.2 . As can be seen from the table, all the results show negative significant differences where the amplitude for the condition NCT is larger than for the condition CT. Early responses of raw ERP have been mainly observed for channels located in the limbic, parietal and frontal areas of the brain, while a highly significant early response of $ERM5$ has been observed for channels in the occipital, parietal and frontal areas of the brain.

6.1.2 Late Response

6.1.2.1 ERP component P100 at 120-180 [ms]

When it comes to consider late stimulus responses as seen in raw data sets (see Figure 6.3-Top), a $P100$ response peak appears delayed by 70 $[ms]$. Corresponding source activity differences between both stimulus modalities mainly show up in central areas. But if mode

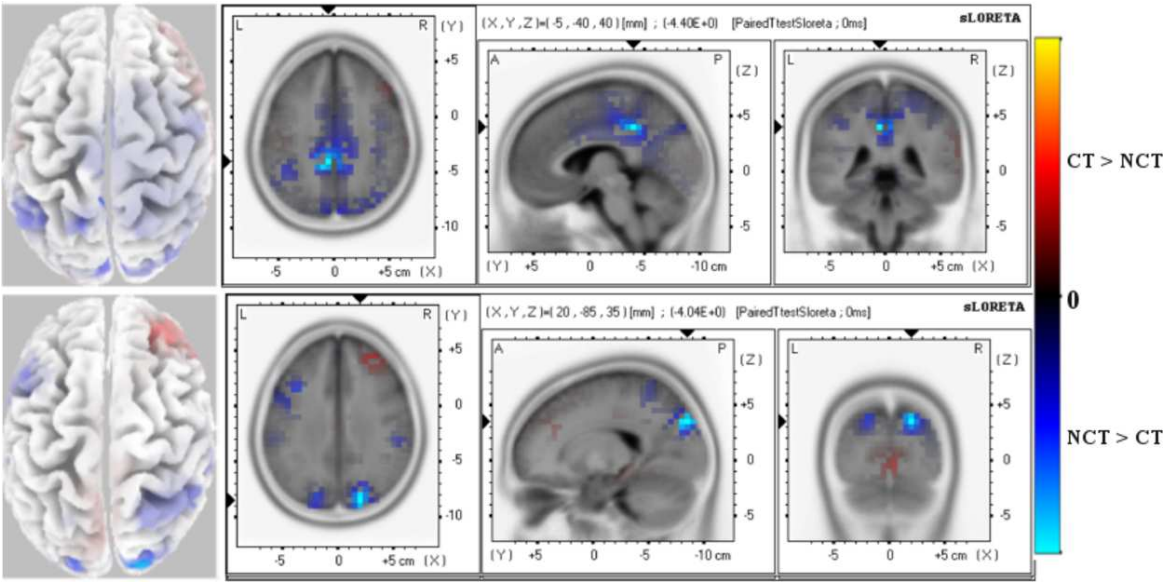

Figure 6.2 **Early Response (150-210 ms) N200 ERP.** Paired t-test values of significant potential amplitude differences at electrodes are illustrated at a significance level as specified. Views are axial, saggital and coronal. The left column shows the distribution on the scalp. All 62 electrodes were used as entries to the data matrix Φ. *(Top):* Raw ERP *N*200 with significance level $\alpha = 0.001$. *(Bottom):* ERM5 extracted from the ERP *N*200 with significance level $\alpha = 0.001$. Red color (positive paired T-test values) indicates that the ERP amplitude for the stimulus condition *CT* is larger than for condition *NCT* while blue color (negative paired T-test values) indicates that the ERP amplitude for the stimulus condition *NCT* is larger than for condition *CT* .

Table 6.2 **T-test statistics for early *N200* ERP and *ERM5* response**. The table shows coordinates of the most significant voxel of clusters. The sign of T-test values indicates the differences between stimuli ($'-'NCT > CT$, $'+'CT > NCT$). T-values are given for different confidence levels: $(*) : \alpha = 0.01, (**) : \alpha = 0.001$.

		ERP				
X	Y	Z	T-value	Voxels-No	BA	Brain Lobe
-5	-40	40	-4.40	99	(31**,24*)	Limbic
-15	-50	55	-4.35	127	(7**,19*,31*,40*)	Parietal
-20	-45	50	-3.90	40	(5*,31*)	Frontal
10	-60	30	-2.91	8	31*	Occipital
		ERM5				
X	Y	Z	T-value	Voxels-No	BA	Brain Lobe
20	-85	35	-4.04	32	(7**,19**)	Parietal
20	-90	35	-3.76	22	(7*,19*)	Occipital
-40	10	40	-2.99	18	9*	Frontal

ERM5 is considered instead, highly focused activity differences appear (see Figure 6.3-Bottom). The significant activity differences are only seen in visual cortex of the right hemisphere. Again, mode *ERM5* shows a much more focused activity distribution than the raw data set.

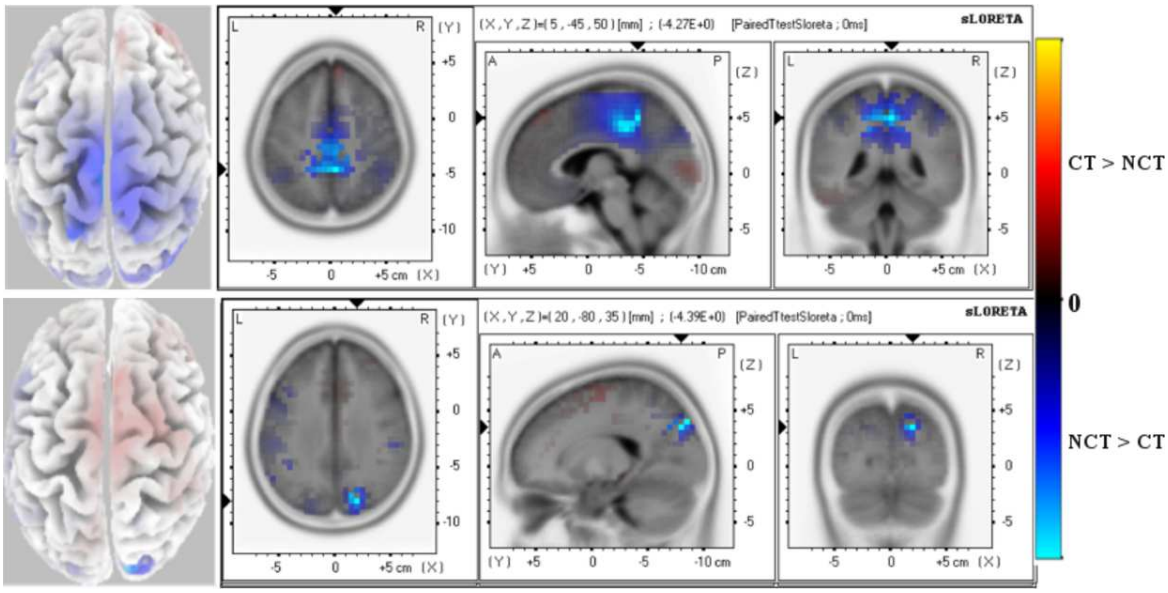

Figure 6.3 **Late Response (120-180 ms) P100 ERP.** Paired t-test values of significant potential amplitude differences at electrodes are illustrated at a significance level as specified. Views are axial, saggital and coronal. The left column shows the distribution on the scalp. All 62 electrodes were used as entries to the data matrix Φ. *(Top):* Raw ERP $P100$ with significance level $\alpha = 0.001$. *(Bottom):* ERM5 extracted from the ERP $P100$ with significance level $\alpha = 0.001$. Red color (positive paired T-test values) indicates that the ERP amplitude for the stimulus condition CT is larger than for condition NCT while blue color (negative paired T-test values) indicates that the ERP amplitude for the stimulus condition NCT is larger than for condition CT .

Table 6.3 summarizes, for late response of the $P100$ ERP, coordinates, T-values of the test statistics at different confidence levels, the Brodmann area and the anatomical area where the significant differences are. The highly significant differences are located at frontal and parietal regions ($\alpha = 0.001$) while sub-lobar and limbic regions show significant differences of ($\alpha = 0.01$). When $ERM5$ is considered, significant results can be summarized in Table 6.3. As can be noted in the table, the significant results are focused in the occipital and parietal regions at significance level ($\alpha = 0.001$).

6.1.2.2 ERP component N200 at 200-260 [ms]

Considering the ERP $N200$ at the late response electrodes, significant activity differences show up in occipital and parietal regions of the left hemisphere with negative paired t-test values, but activity differences with slightly positive paired t-test values also appear in pre-

Table 6.3 **T-test statistics for late *P100* ERP and *ERM5* response**. The table shows coordinates of the most significant voxel of clusters. The sign of T-test values indicates the differences between stimuli ($'-'NCT > CT, '+'CT > NCT$). T-values are given for different confidence levels: $(*) : \alpha = 0.01, (**) : \alpha = 0.001$.

			ERP			
X	Y	Z	T-value	Voxels-No	BA	Brain Lobe
5	-45	50	-4.27	199	(5**,31**,4*,6*)	Frontal
5	-35	40	-4.21	146	(31**,23*,24*)	Limbic
5	-35	45	-4.14	80	(7**,4*,31*,40*)	Parietal
-45	-25	20	-2.97	9	13*	Sub-lobar
			ERM5			
X	Y	Z	T-value	Voxels-No	BA	Brain Lobe
20	-80	35	-4.39	18	(7**,19**)	Parietal
20	-80	30	-3.32	13	(7*,19*)	Occipital

frontal regions of the right hemisphere (see Figure 6.4-Top). Positive t-test values have been observed for channels located in the frontal areas of the brain, while negative t-test values have been observed for channels in the occipital and parietal area of the brain. Both positive and negative t-test values of the ERP are slightly different at a significance level $\alpha = 0.05$. Again, if it comes to compare these results with those obtained by using only amplitudes of mode $ERM5$, highly focused significant activity differences are located in frontal and occipital areas with strongly positive paired t-test values while a clear focus of weakly negative paired t-test values also appears in parietal areas (see Figure 6.4-Bottom). These results are summarized in Table 6.4. As can be seen in the Table 6.4, positive differences of the conditions responses are located in the parietal and occipital regions of the brain while negative differences are detected in the frontal region.

Table 6.4 **T-test statistics for late *N200 ERM5* response**. The table shows coordinates of the most significant voxel of clusters. The sign of T-test values indicates the differences between stimuli ($'-'NCT > CT, '+'CT > NCT$). T-values are given for confidence level: $(*) : \alpha = 0.01$.

			ERM5			
X	Y	Z	T-value	Voxels-No	BA	Brain Lobe
60	-10	45	-3.18	69	(4*,6*,10*,45*,47*)	Frontal
-5	-95	-10	3.46	59	(17*,18*)	Occipital
-20	-40	70	3.21	6	3*	Parietal
-10	50	0	3.14	13	(10*,32*)	Limbic

These results generally comply, in terms of activated regions, with results from an analysis of fMRI data which was taken jointly with our data [6][4]. This means that these neurons are more active than others which also responded to the contour integration task. In [6][4], the significant activation differences are highlighted in different regions like occipital, bilateral

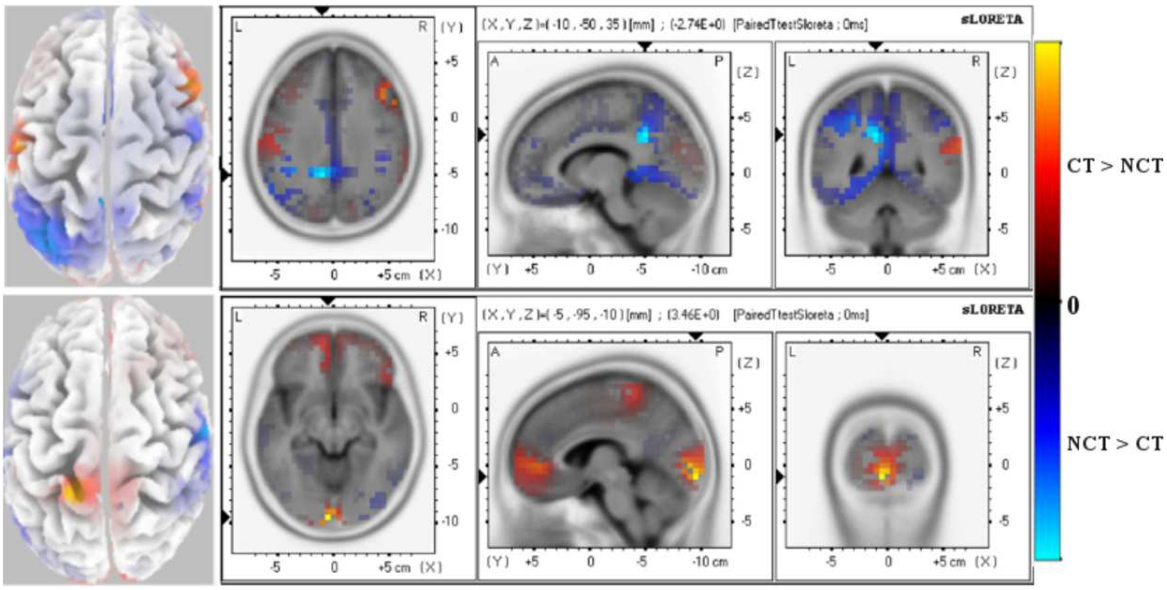

Figure 6.4 **Late Response (200-260 ms) N200 ERP.** Paired t-test values of significant potential amplitude differences at electrodes are illustrated at a significance level as specified. Views are axial, saggital and coronal. The left column shows the distribution on the scalp. All 62 electrodes were used as entries to the data matrix Φ. *(Top):* Raw ERP *N*200 with significance level $\alpha = 0.05$. *(Bottom):* ERM5 extracted from the ERP *N*200 with significance level $\alpha = 0.01$. Red color (positive paired T-test values) indicates that the ERP amplitude for the stimulus condition *CT* is larger than for condition *NCT* while blue color (negative paired T-test values) indicates that the ERP amplitude for the stimulus condition *NCT* is larger than for condition *CT* .

parietal, temporal and frontal regions (the test has been done using the same p-value, $\alpha = 0.001$, for all). The fact that, comparing both modalities, occasionally different brain regions are involved in contour and non-contour processing renders the comparison suitable for further analysis. Here, for example, with *ERM*5, the late response *N*200 is pronounced in occipital, temporal and frontal regions, precisely as was found with an fMRI analysis in case of volume intrinsic mode functions (VIMF1, VIMF2, VIMF3 and VIMF4) [4]. Figure 6.5 presents an illustrative comparison of a saggital view of VIMF1 and *ERM*5 extracted from the late ERP *N*200. The VIMFS were extracted by using a new variant of a two dimensional empirical mode decomposition called GiT-BEEMD [5]. Hence, the superior precision in spatial localization of activity blobs corroborates the potential of EEMD/2DEEMD when analyzing functional neuroimages.

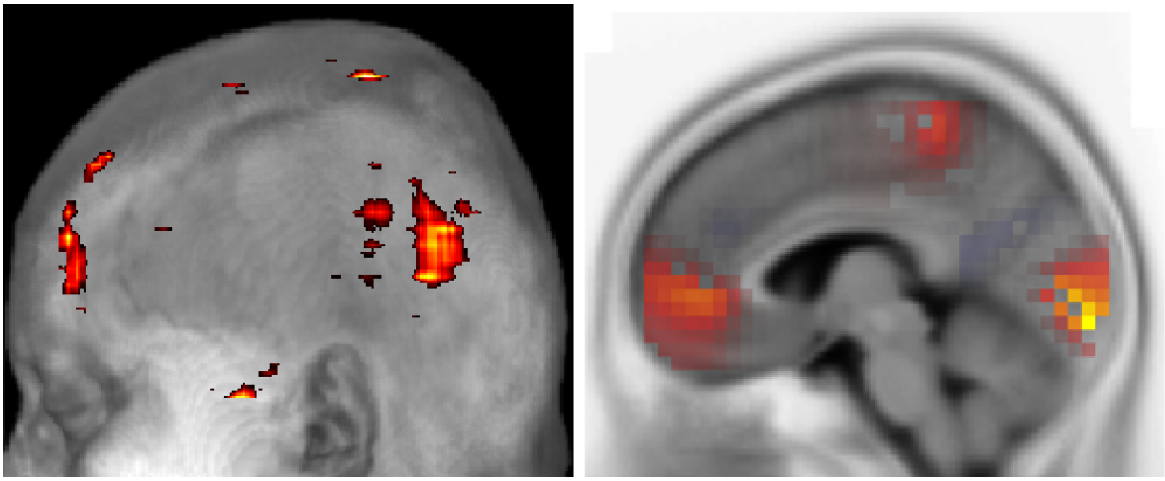

Figure 6.5 **EEG compared to fMRI.** Saggital view of *left:* the intrinsic mode VIMF1, as extracted with GiT-EEMD from fMRI data, and *right:* data reconstructed from *ERM*5. The latter was obtained from EEG data. The comparison concentrates on the late ERP *N*200.

Chapter 7

EMDLAB Toolbox

To serve the growing interest of the signal processing community in applying Empirical Mode Decomposition (EMD) as a decomposition technique, a new toolbox, called EMDLAB, has been introduced. Traditionally, EEGs are studied at the level of event related potentials (ERPs) which represent averages over a sufficiently large number of single trial recordings. In case of multi-trial data, EMD is applied to data either trial by trial or as single-trial response signal at each channel separately. Then all corresponding IMFs become averaged over all trials to yield *event-related modes* ERMs. The main goal of EMDLAB toolbox is to extract characteristics of either the EEG signal by IMFs or ERMs. Since IMFs reflect characteristics of the original EEG signal, ERMs reflect characteristics of ERPs of the original signal. In EMDLAB, data structure and visualization of the extracted modes is adopted from the EEGLAB MATLAB toolbox [40], therefore it is suggested to use EMDLAB as a plug-in for EEGLAB. Similarly, the toolbox is primarily designed for EEG data, although both EEGLAB and EMDLAB can process MEG data as well. EMDLAB toolbox offers a comprehensive range of EMD methods, including many popular designs like EMD, Ensemble EMD (EEMD), weighted Sliding EMD (wSEMD), and Multivariate EMD (MEMD). The latter three are extensions of the original EMD algorithm. All these methods have been discussed in detail in Chapter 3. Contrary to other toolboxes dedicated to the analysis of ERPs, EMDLAB is used to analyze the characteristic of ERPs based on the extracted modes. This Chapter is organized as follows: Section *EEGLAB and EMDLAB* represents an overview of EEGLAB toolbox and the developed toolbox, EMDLAB. Next, in Section *Simulation and Result* we provide an example of EEG data trials drawn from an experiment of a contour integration task [10][73] in order to illustrate the utility of EMDLAB. In this section, the toolbox components, together with some screenshots from the graphical user interface (GUI) are described.

7.1 EEGLAB and EMDLAB Toolboxes

7.1.1 EEGLAB Toolbox

EEGLAB is an interactive toolbox, running under MATLAB, for processing continuous and event-related EEG, MEG and other electrophysiological data [40]. It provides a graphical user interface (GUI) which enables users to flexibly and interactively process their EEG and other brain data using independent component analysis (ICA) and/or time/frequency analysis (TFA). This GUI allows users processing their data and tuning their parameters. EEGLAB provides plenty of methods for importing, visualizing, preprocessing data and modeling event-related brain dynamics. Using the GUI of EEGLAB, users can apply advanced signal processing techniques to their data [40] such as:

- Multiformat data importing.
- Data visualization through interactive plotting functions.
- Data processing such as artifact removal, event and channel localization, component extraction, time/frequency analysis and forward/inverse source modeling.
- Open source plug-in facility.

One of the strengths of EEGLAB is offering a programming environment which allows users to distribute newly developed tools and algorithms through EEGLAB *plug-in* functions. The latter can be downloaded and installed by other users and are available to them within EEGLAB menus. The toolbox also has an important merit by providing an easy-to-follow path to write flexible scripts. Each time a user performs any operation in the GUI, the called function is automatically appended to the EEGLAB command history.

7.1.2 EMDLAB Toolbox

The proposed EMDLAB toolbox can be closely implemented into the EEGLAB toolbox via the plug-in facility of the GUI. EMDLAB relies largely on the functions of EEGLAB for importing data and visualizing results. EMDLAB offers additional signal processing modalities – more specifically EMD and its derivates – to be integrated into EEGLAB for the analysis of biomedical signals opening up the possibility to extensively process extracted modes – comparable to the processing of independent components resulting from an ICA, which is traditionally done with EEGLAB. EMDLAB also provides a GUI, which helps the user to handle his data and perform signal processing tasks fitted to the EMD analysis. It renders all implemented options immediately available without the need to resort to the documentation. The GUI of EMDLAB is designed in such a way that it also can be used as a teaching tool for beginners. EMDLAB uses the same approach as EEGLAB in a sense that each time the user selects an operation from the menu the function called by MATLAB - including all input parameters - is saved to the command history of the EEGLAB session.

7.2 Simulation and Result

The basic functionality of the EMDLAB toolbox is to provide a plug-in to the EEGLAB toolbox for analyzing EEG data with EMD or one of its variants implemented in the EMDLAB toolbox. The latter includes a group of matlab functions for applying EMD [80], EEMD [236], wSEMD [47] and MEMD [170]. All these methods have been described in detail in Chapter 3. EMDLAB relies heavily on EEGLAB's functions for importing recorded EEG data. Additionally, EMDLAB uses functions of EEGLAB to analyze and visualize the modes resulting from an EMD analysis. Corresponding code has been modified to include, for example, plotting EEG waveforms of each mode or obtaining *Event Related Modes* (ERMs) and related topographies, so-called *scalp maps*. Much like *Event-Related Potentials* (ERPs), ERMs are obtained as an average of corresponding IMFs over a set of trials.
Figure 7.1 shows a screen shot of the *graphical user interface* of the EEGLAB toolbox which now contains an EMDLAB menu in case EMDLAB toolbox has been installed already. As illustrated in the figure, the EMDLAB menu includes two main parts:

- The first part is used to decompose signals using EMD or one of its variants.
- The second part contains various methods to analyze and visualize the extracted modes.

7.2.1 Run EMD

Figure 7.2 presents the main window of the EMDLAB toolbox. It is used to perform the decomposition using different types of EMD. The system will automatically recognize if the data set is epoched or continuous. In the former case, an information saying *trial-by-trial* will show up in the main window. Otherwise, the information given will be *continuous*. Before being decomposed into IMFs, data can be normalized to zero mean and unitary standard deviation by checking the *Normalize* box. Normalization is advisable as it helps to have the same scale for all single trial signals to be compared. Also through this window, users are able to select any of 4 available EMD algorithms, namely EMD [80], EEMD [236], wSEMD [47] and MEMD [170]. Any of these algorithms can be applied directly to each single-trial EEG data set.
EMDLAB asks users to assign the *number of modes J* which the signal will be decomposed into. This is needed for the EEMD algorithm to assure comparability of the extracted modes. However, it also allows the user to deliberately integrate slow modes into the "residuum", i. e. the component $J+1$. Additionally, this GUI allows the user to easily enter and tune parameters of each EMD variant such as the variance of the *added noise* and the *ensemble number* in case of EEMD, the *window size* and the *step size* in case of wSEMD and the variance of the *added noise* and *number of noise channels* as well as the *ensemble number* in case of MEEMD. Furthermore, the studied channels can be selected simply by clicking the *channels* button, otherwise all channels will be considered by default.

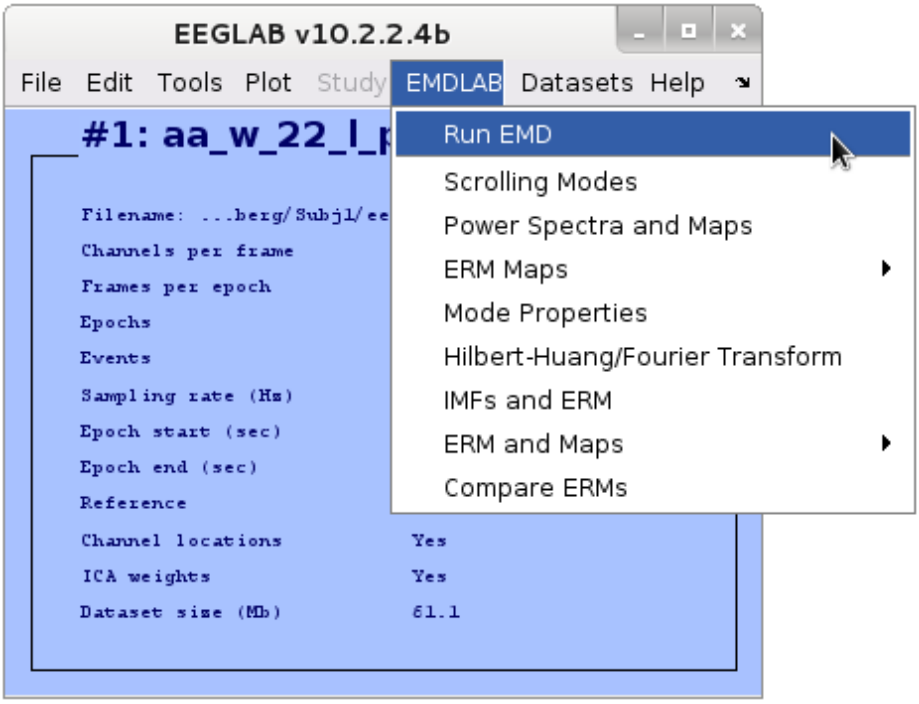

Figure 7.1 **The main EEGLAB graphical user interface (GUI), with the EMDLAB menu activated.** The datasets menu presents a list of currently active EEG sets, and the EMDLAB menu shows a list of currently active sets.

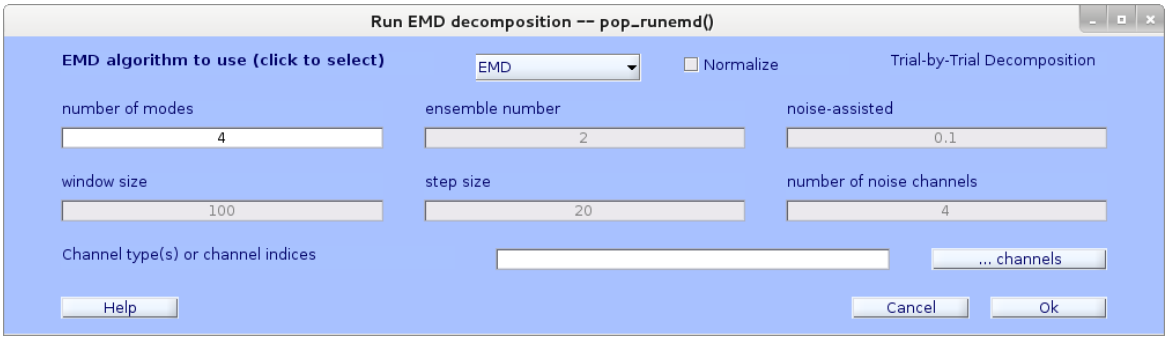

Figure 7.2 **The EMDLAB main user interface.** This window is used for EMD decomposition. Through this window, user can choose the data, algorithm and appropriate parameters for the decomposition.

7.2.2 Analyze and visualize modes

After the signal decomposition has been performed, the resulting modes can be analyzed further using the additional choices of the main EMDLAB menu:

- *Scrolling Modes*: allows the user to visualize the extracted modes (IMFs). The user can simply move between the different modes by using the drop-down menu of the combo box aside of the "Select Mode" label (see Figure 7.3).

- *Power Spectra and Maps*: here the power spectra of the extracted ERMs can be plotted as well as scalp maps of the power within chosen frequency bands. However, first the ERM of interest should be selected as well as additional required inputs (see Figure 7.4).

- *ERM Maps*: here the dynamics of topographic maps of the ERMs can be visualized in either 2D or 3D (see Figure 7.5).

- *Mode Properties*: single trial IMFs, related ERMs and their activity power spectrum can be plotted directly by selecting the mode of interest first (see Figure 7.6).

- *Hilbert-Huang / Fourier Transform*: plotting the Hilbert-Huang spectrum as well as the Fourier spectrum of a selected mode (see Figure 7.8).

- *IMFs and ERM*: it offers, for any chosen mode of interest, a color-coded image of all single-trial IMFs and the related ERM (see Figure 7.12).

- *ERM and Maps*: this option allows plotting all channels of an ERM of interest plus their topographic representation (scalp maps) at selected latencies (see Figure 7.13).

- *Compare ERMs*: this allows the user to compare ERMs of different datasets, i. e. recorded under different conditions, using simple statistics (see Figures 7.14 and Figure 7.15).

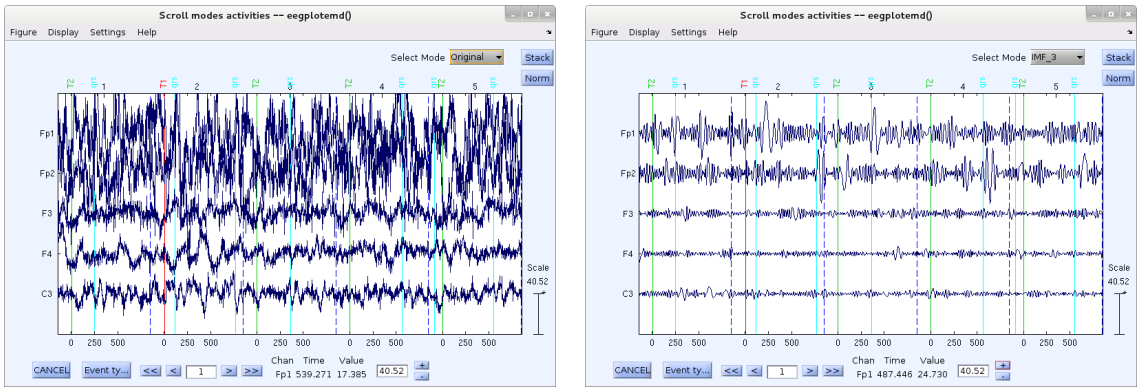

(a) **Data scrolling.** (b) **IMF3 scrolling.**

Figure 7.3 **Data and its extracted mode (IMF3) scrolling.** Here, five data epochs (separated by dashed lines) are plotted at 5 electrode sites (channel names on the left). The arrow buttons scroll horizontally through the data.

In order to demonstrate the utility of the EMDLAB toolbox, we employ a small set of EEG data trials collected during a contour integration task which have been explained in detail in Chapter 4. In this sample data, only one stimulus condition with correct answer, *contour true (CT)*, was selected.

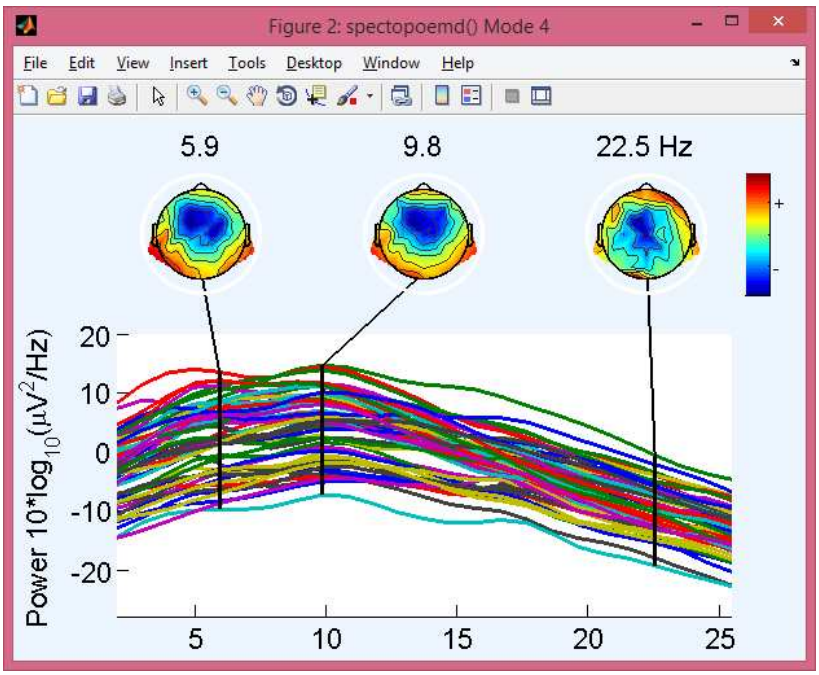

Figure 7.4 **The mode spectra and associated topographical maps.** The figure shows the power spectrum of the 62 channels and the scalp power maps at specific frequencies. Each colored trace represents the spectrum of the activity of IMF4 of one data channel. The scalp maps indicate the distribution of power at specified frequencies 5.9, 9.8 and 22.5 Hz.

7.2.2.1 Scrolling Modes

Figure 7.3 represents 5 epochs of 5 EEG channels and their $IMF3$ after applying EMD. This scrolling data figure allows users to review data by visual inspection and navigate their different modes.

7.2.2.2 Power Spectra and Maps

Here the user can exhibit the power spectra, and the related topographic maps, of all or selected channels at specific frequencies. Figure 7.4 exemplifies the power spectra of all channels for three different frequencies specified. Note that this offers the possibility to illustrate the power spectra of pooled electrodes in certain brain areas like the occipital or frontal regions of the brain, for example.

7.2.2.3 ERM Maps

Figure 7.5 exhibits a series of scalp maps representing activity distributions of $ERM4$ at a selected series of trial latencies, i. e. every 20 $[ms]$ from 50 $[ms]$ to 270 $[ms]$. These topographies represent the mapping of electrical activity across the surface of the brain at different latencies. They show the brain regions which act in response to a stimulus.

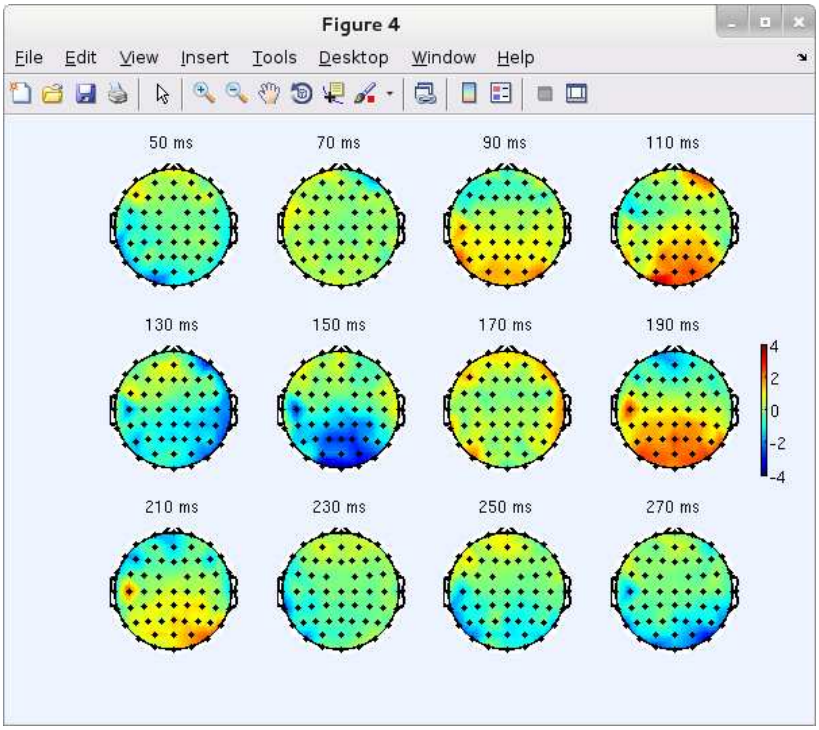

Figure 7.5 **Topographical 2-D scalp maps of ERM4 at different latencies.** They represent distribution of the activity (given by the scaled color bar) over the head. Dots overlaid on the scalp maps indicate channels.

7.2.2.4 Mode Properties

Figure 7.6 illustrates the properties of a specific mode, $IMF4$ for a specific channel $O2$. This plot includes a scalp location of $O2$ channel, its activity power spectrum, and an ERP-image plot of its activity in single-epochs. The leftmost topogram exhibits the scalp location of channel $O2$. On the right, single trial EEG signals composing $ERM4$ of the EEG signal recorded at channel $O2$ is illustrated. Channel signals are color-coded and the resulting $ERM4$ signal is added at the bottom of the subfigure. Such a plot can be used to analyze single trial IMFs of single channel data within an epoch across latencies. These data can be plotted in any sorting order of interest. The bottom row in Figure 7.6 shows the activity power spectrum of $IMF4$ of $O2$ channel at a frequency range between 2 and $50Hz$.

7.2.2.5 Hilbert-Huang / Fourier Transform

Figure 7.7 presents the window which offers tools for spectral analysis of the extracted modes. As EMD is most useful for non-stationary time series, time - frequency analysis is most appropriate. As explained above, Hilbert - Huang spectra are obtained from a combination of an EMD of a non-stationary time series with concomitant Hilbert transform of the real valued signal. Note that the resulting IMFs represent wide-sense stationary sig-

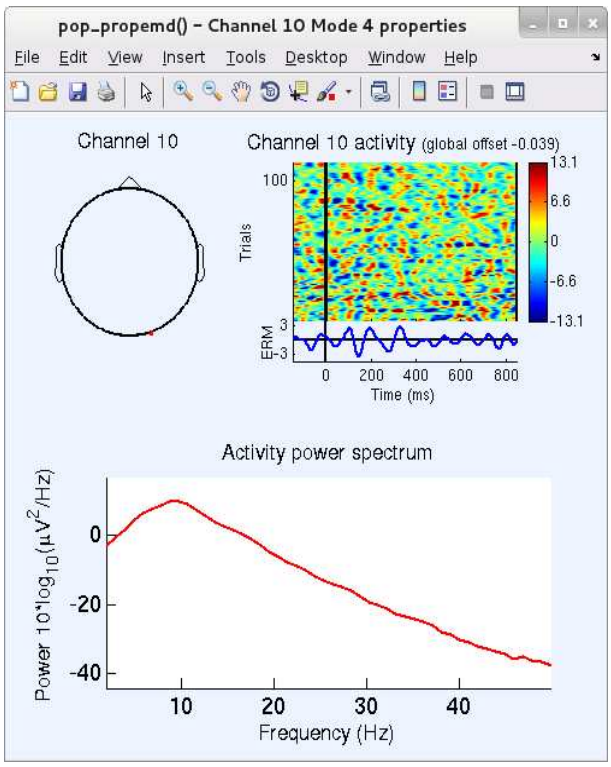

Figure 7.6 **IMF4 properties of channel 10 (O2).** *Top left:* The head plot (top left) containing a red dot indicates the position of the selected channel. *Top right:* ERP image of $IMF4$, each horizontal line in this colored image representing $IMF4$ of a single trial in an event-related dataset. The trace below the ERM image shows the average of the $IMF4$ of a single-trial activity, i.e. the ERM average of the imaged data epochs. *Bottom panel:* the activity power spectrum of $IMF4$ for channel 10.

nals, hence can be Fourier - transformed as well. EMDLAB has implemented both spectral modalities. Figure 7.8 illustrates the use of these modalities employing the EEG signal used throughout this discussion. While Hilbert - Huang spectra allow to track temporal changes of each local mode, Fourier spectra represent their spectral content. Both modes of analysis are shown within one window to ease visual comparison. Figure 7.8 illustrates Hilbert and Fourier spectrum of several ERMs for an EEG single channel, *top:* Hilbert spectrum explains the instantaneous frequency over the time and the different colors refers to the instantaneous amplitude. *Down:* the Fourier spectrum for the same EEG single channel. Fourier spectrum of each ERM was represented in different color. It is observed that first ERMs in Hilbert and Fourier spectrum have high frequencies than the last ERMs which may reveal that these ERMs mainly describes noise. It is not easily apparent from the plot of the ERMs in time whether the function is likely to contain meaningful information. Taking the Hilbert spectrum of the ERMs individually is helpful in identifying which of the modes contributes most strongly to the overall signal energy. Also temporal changes in frequency of the ERMs can be followed easily, while their Fourier spectrum only displays the spread

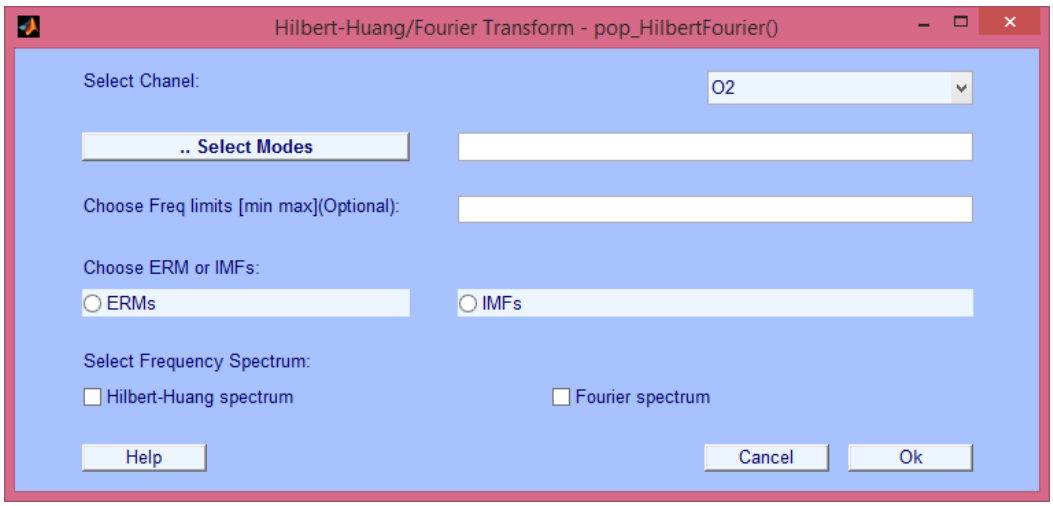

Figure 7.7 **Hilbert-Huang and Fourier spectrum user interface.**

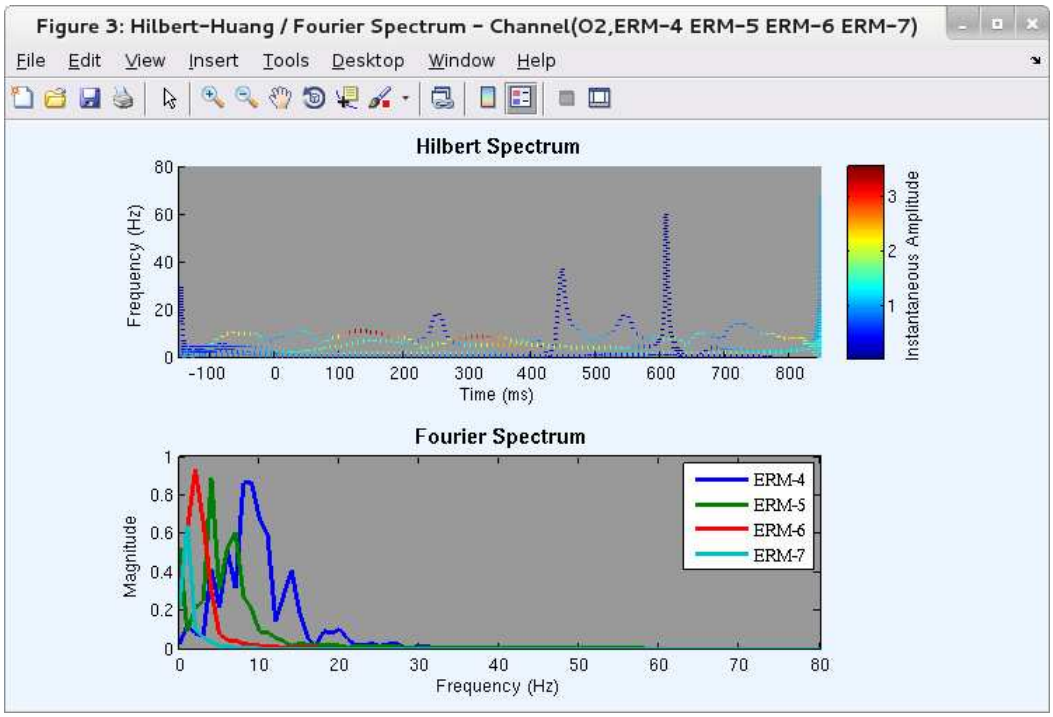

Figure 7.8 **Hilbert and Fourier spectrum for ERM4-ERM7 of an EEG signal.** *Top:* Hilbert spectrum of selected ERMs, colorbar indicates the instantaneous amplitude of ERMs. *Down:* Fourier Spectrum of selected ERMs, different colors refer to different ERMs.

in energy density and shows strong overlap of the different modes (see Figure 7.8). To further clarify the use of the Hilbert - Huang Spectra, Figure 7.9 illustrates the variation of the time-dependent frequency with time for all trials of one epoch. Hereby the user can choose

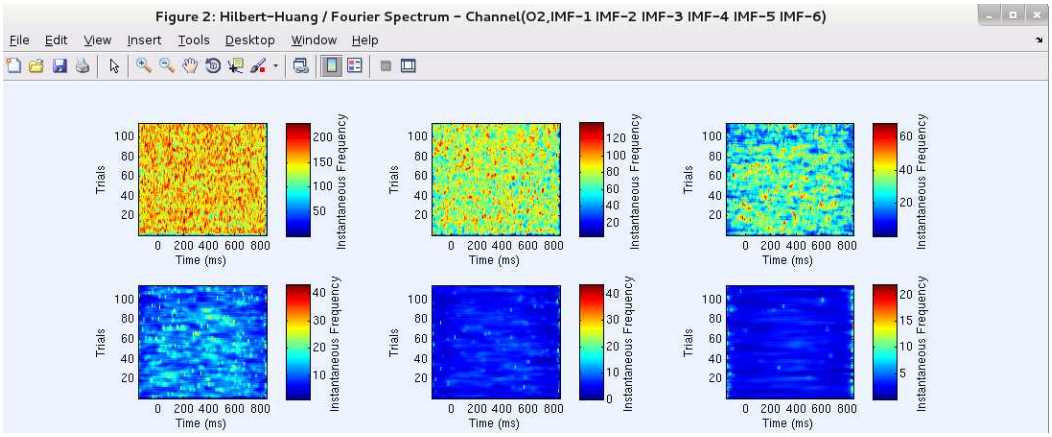

Figure 7.9 **Example of Hilbert spectrum image for some extracted modes.** From left to right, top to bottom: Hilbert spectrum image of IMF1-IMF6 of O2 single channel. It is a color-coded image of IMF1-IMF6 of all single trials. colorbars indicate the instantaneous frequency of each IMF image.

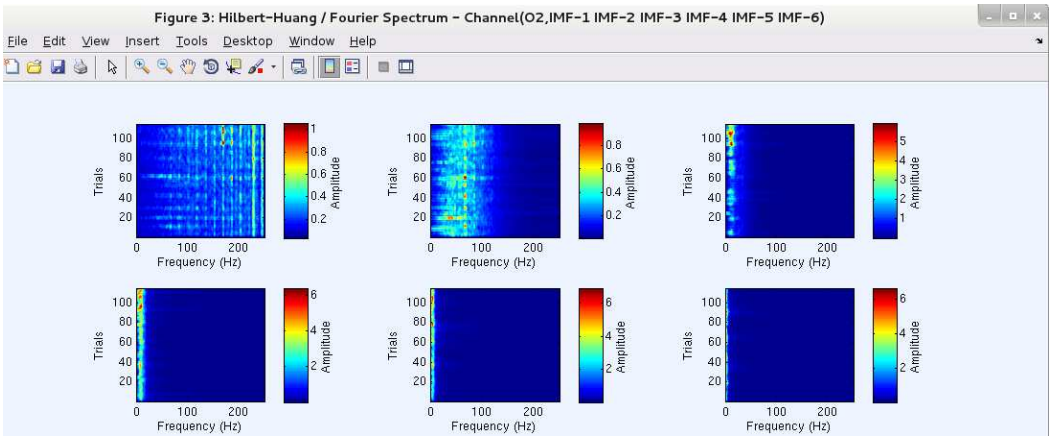

Figure 7.10 **Example of Fourier spectrum image for some extracted modes.** From left to right, top to bottom: Fourier spectrum image of IMF1-IMF6 of O2 single channel. It is a color-coded image of IMF1-IMF6 of all single trials. colorbars indicate the amplitude of each IMF image.

the channel as well as the number of IMFs to be shown. Frequency is color-coded, while the related plot exhibited in Figure 7.10 shows the corresponding variation of the amplitude of the IMFs during each trial. Here the IMF amplitude is color-coded as shown. Last but not least Figure 7.11 illustrates the variation in time of the frequency of the specified IMF for all trials within a certain frequency band selected, and the related variation of the IMF amplitude as a function of the frequency for all trials of one epoch.

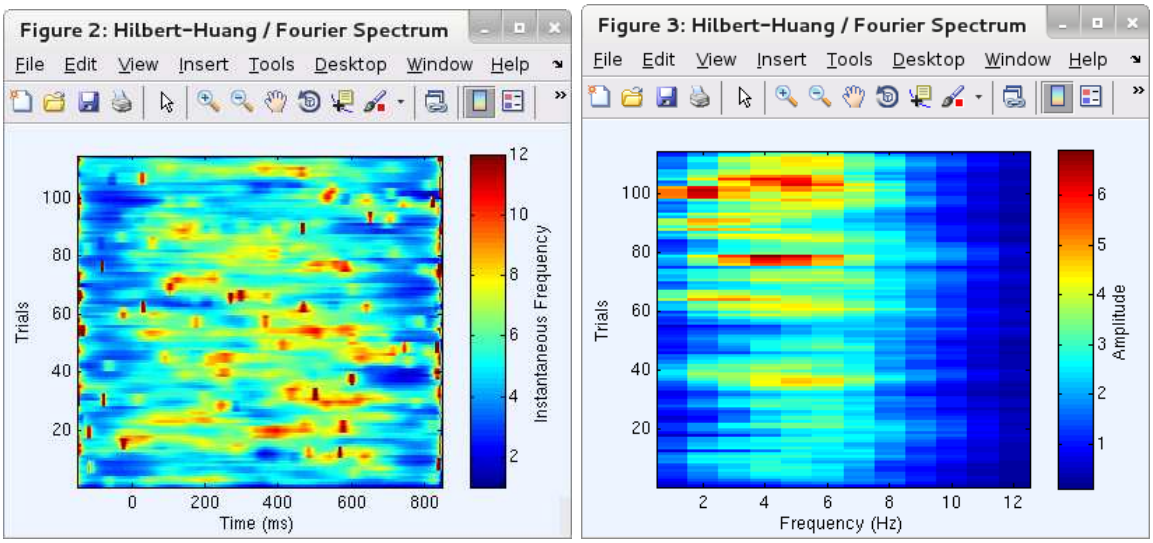

Figure 7.11 **Hilbert and Fourier spectrum image of IMF5 of O2 channel.** *Left:* Hilbert spectrum image of IMF5 at selected frequency [1 12]. *Right:* Fourier Spectrum image of IMF5 at the same frequencies.

7.2.2.6 IMFs and ERM

This option offers a plot of the activity of a prespecified extracted IMF for all trials within an epoch. Alternatively the user can select certain trials instead of choosing all trials. Also shown is the ERM resulting from an average of the specified IMF over all trials. Such trials and ERMs can be illustrated for each of the electrodes involved. The response activity is encoded by a color bar exhibited in Figure 7.12. Note that, similar to EEGLAB, the zero indicates the stimulus onset.

7.2.2.7 ERM and Maps

Figure 7.13 overlays time courses of all $ERM4$ modes extracted from 62 EEG channel recordings. Related scalp maps can be illustrated at selected latencies as well. Each of these traces plots the $ERM4$ at one channel. The scalp maps shown represent "snapshots" of the topographic distribution at various latencies 50 $[ms]$, 100 $[ms]$, 150 $[ms]$, 200 $[ms]$ during the average $ERM4$ time course.

7.2.2.8 Compare ERMs

This option offers an overview of specified ERMs for the different conditions as well as their differences at each channel as shown in Figure 7.14. In addition, the user can choose showing related simple statistics like standard deviations etc. By simply clicking on one of the channels, the user gets to a more detailed view of the ERMs shown at a specific channel selected as is illustrated in Figure 7.15 for channel $O2$. This provides especially an clear illustration of how the estimated ERMs differ for the two conditions studied.

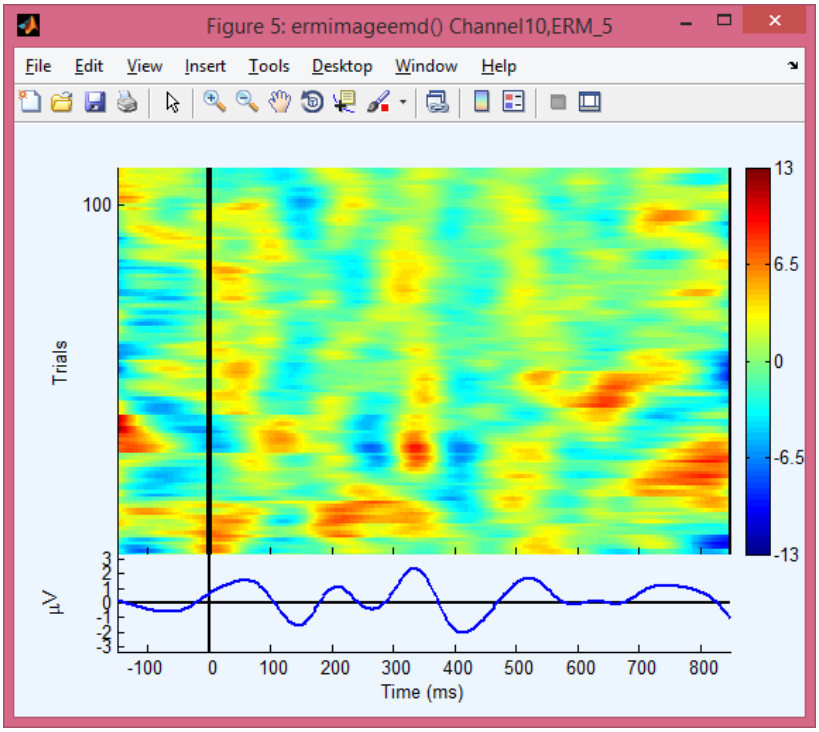

Figure 7.12 **Plot of ERM5 image of O2 channel.** It is a rectangular colored image in which every horizontal line represents activity of IMF5 of a single experimental trial. The signal below the image shows the ERM average of the imaged IMF5 of data epochs.

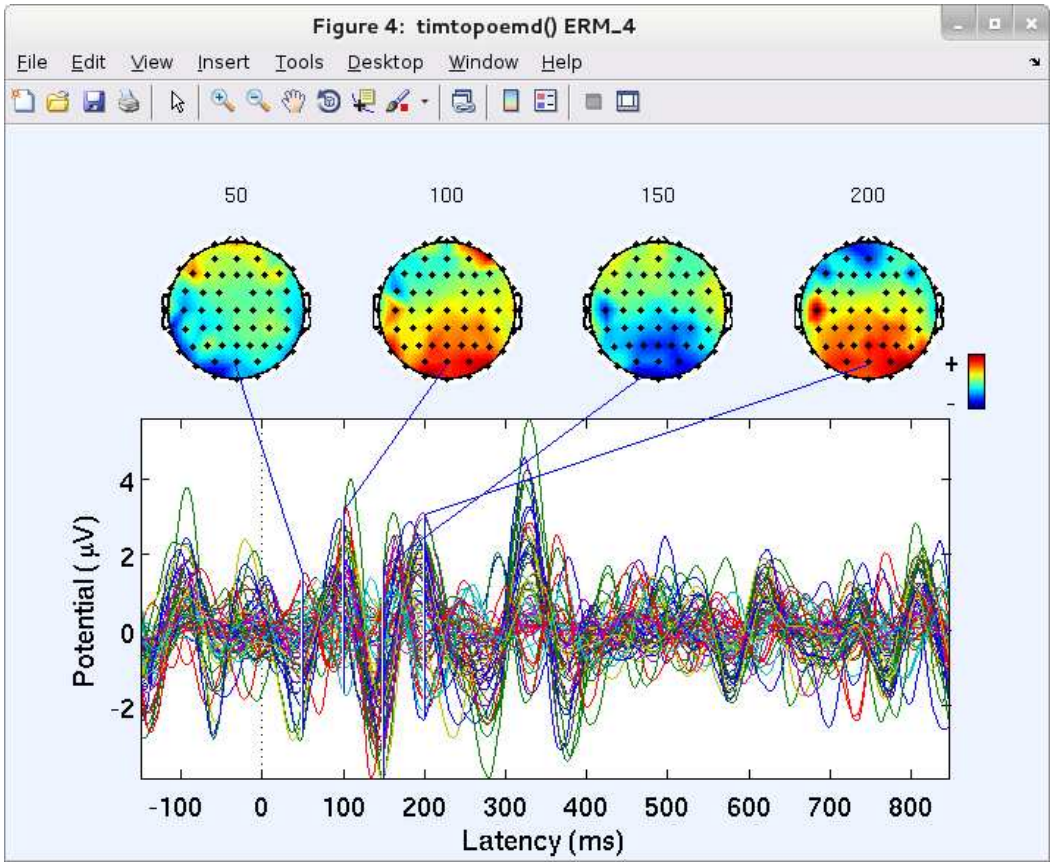

Figure 7.13 **ERM4 waveforms of 62 channels and their scalp maps at specified latencies.** *Top:* scalp maps show the topographic distribution of average potential of $IMF4$ at $50, 100, 150, 200ms$. *Down:* each trace in the waveforms plots the averaged ERM4 at one channel.

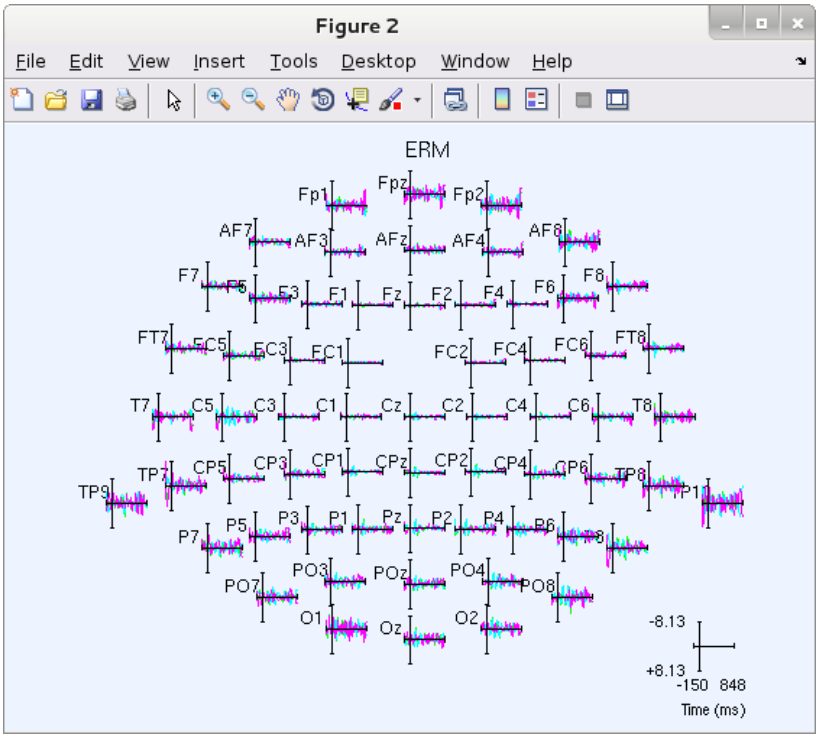

Figure 7.14 **62 different ERM plots .** Each plot represent ERM5 of two datasets: contour and non-contour conditions and the difference between them.

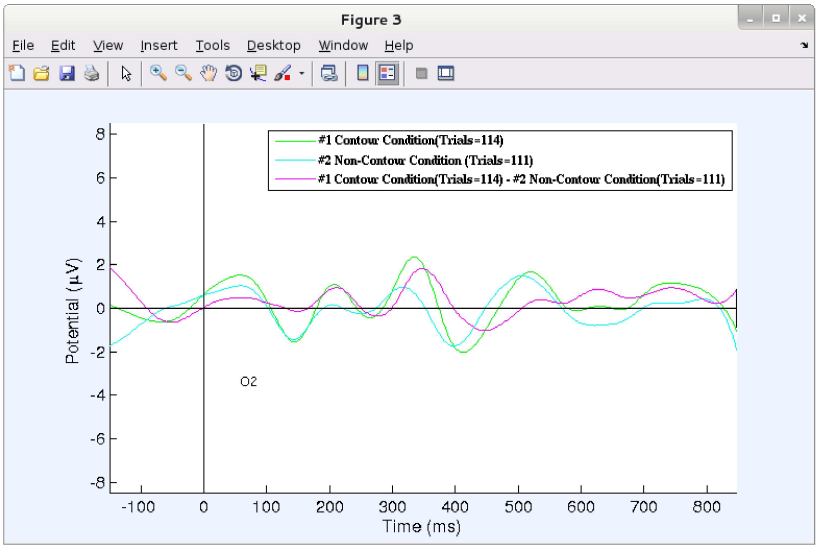

Figure 7.15 **ERM5 of contour and non-contour conditions and the difference between them for O2 channel.**

Chapter 8

Conclusion

In this investigation we used a data-driven approach to analyze EEG data from 18 subjects participating in a perceptual learning task. A contour and a non-contour stimulus were presented within the same trial in fast succession, and subjects were asked to indicate their presence *CT* (contour true) or absence *NCT* (non-contour true). An EEMD method allows to extract component signals which show differences between stimulus conditions with clear statistical significance. The analysis has been performed in two different ways: either using the raw data ERPs or EEMD intrinsic modes called event related modes (ERMs). Most notably $ERM5$ exhibits very pronounced differences between contour and non-contour stimulus responses. Signals have been pooled according to a clustering scheme that divides brain electrodes according to the latencies of the stimulus responses. Early responses are seen in occipital and parietal areas of the brain, while late responses are located in primary visual, medio-temporal and frontal areas. The pool of electrodes in the central part of the brain even exhibits both early and late responses in pronounced double peak structures. Together these findings provide independent evidence of a view of extended neuronal networks involved in visual processing, especially contour integration.

Another line of investigation concentrated on identifying related sources of neuronal activation via inverse modeling. It explored the utility of combining an EEMD analysis with a source localization scheme, more specifically an sLORETA source estimation. Note that EEMD has been applied before averaging over trials. Statistically significant differences between the two stimulus conditions have been seen mainly with ERP components $P100$ and $N200$. The previous study [10] showed that $ERM5$ exhibits very pronounced differences between contour and non-contour stimulus responses, hence only $ERM5$ has been used in the analysis. As obtained from $ERM5$, earlier differences (before $210ms$) in source activity between contour and non-contour occurred mainly in occipito-parietal areas, were lateralized to the right hemisphere and showed higher power in the non-contour compared to the contour condition. Later differences ($200-260ms$) occurred also in primary visual areas, in both hemispheres and with higher power in the contour compared to the non-contour condition. The latter result fits well with the view that contour integration relies on a top-down flow of information from higher visual areas with large receptive fields into primary visual cortex. The feedback would enhance activity of neurons coding Gabor stimuli at relevant

locations and so favor their integration [216][179]. The former result is partly unexpected in that lower source activity was for contours compared to non-contours. It is possible that the difference reflects the reduced effort of maintaining grouped compared to ungrouped visual input in working memory [86][215]. In any way, the fact that the difference showed up in right hemisphere complies with the previous finding that contour grouping is a right-lateralized brain function [214]. The results of this study which focuses on identifying related sources of neuronal activation clearly via inverse modeling of EEG data were extremely well matched with the previous ones in [10] that discussed the forward problem on the same data. Results showed that EEMD method allows to extract components, i.e *ERM*5 which present clearer spatio-temporal differences between the two stimulus responses, *CT* and *NCT* compared to the ERPs of the original signals.

In this thesis, we also presented a new toolbox, called *EMDLAB*, which allows users to conveniently analyze non-stationary time series data sets, especially EEG data, with a heuristic signal decomposition techniques called *Empirical Mode Decomposition*. The latter decomposes any signal locally without imposing additional conditions like orthogonality, independence or sparseness. The new toolbox *EMDLAB* is provided as a plug-in to the well-known *EEGLAB* toolbox and offers an alternative decomposition technique in four different variants. Beneath plain EMD, a noise-assisted variant, named *Ensemble EMD* is offered which is suitable as long as the data size is small enough to be stored in main memory. For very long time series, the weighted sliding EMD is more appropriate. Finally, a simultaneous multi-channel analysis can be pursued employing a multi-variate EMD variant. The plug-in allows to use any data visualization tool provided by the *EEGLAB* toolbox as well as statistical data analysis techniques provided there.

Bibliography

[1] Z. A. Acar and S. Makeig. Neuroelectromagnetic forward head modeling toolbox. *Journal of Neuroscience Methods*, 190(2):258–270, 2010.

[2] L.I. Aftanas, A.A. Varlamov, S.V. Pavlov, V.P. Makhnev, and N.V. Reva. Affective picture processing: event-related synchronization within individually defined human theta band is modulated by valence dimension. *Neuroscience Letters*, 303:115–118, 2001.

[3] Emad A. Al-Alem. Epilepsy awareness program - eeg resources, 2014.

[4] S. Al-Baddai. A study of information - theoretic metaheuristics applied to functional neuroimaging datasets. *PhD Thesis, Regensburg Uni*, 2016.

[5] S. Al-Baddai, K. Al-Subari, A. Tomé, D. Salas-Gonzales, and E.W. Lang. Analysis of fmri images with BEEMD based-on green's functions. *Biomedical Signal Processing and Control*, 30:53–63, 2016.

[6] S. Al-Baddai, K. Al-Subari, A. Tomé, J. Sole-Casals, and E.W. Lang. A green's function-based bi-dimensional empirical mode decomposition. *Information Sciences*, 348:305–321, 2016.

[7] S. Al-Baddai, K. Al-Subari, A. Tomé, G. Volberg, S. Hanslmayr, R. Hammwöhner, and E.W. Lang. Bidimensional ensemble empirical mode decomposition of functional biomedical images taken during a contour integration task. *Biomedical Signal Processing and Control*, 13:218–236, 2014.

[8] S. Al-Baddai, K. Al-Subari, A. Tomé, G. Volberg, and E.W. Lang. A combined EMD - ICA analysis of simultaneously registered EEG-fMRI data. *BMVA*, 2015(2):1–15, 2015.

[9] K. Al-Subari, S. Al-Baddai, A. Tomé, M. Goldhacker, R. Faltermeier, and E.W. Lang. Emdlab:a toolbox for analysis of single-trial eeg dynamics using empirical mode decomposition. *Journal of Neuroscience Methods*, 253C:193–205, 07 2015.

[10] K. Al-Subari, S. Al-Baddai, A. Tomé, G. Volberg, R. Hammwöhner, and E.W. Lang. Ensemble empirical mode decomposition analysis of EEG data collected during a contour integration task. *PLoS ONE*, 10(4):e0119489, 04 2015.

[11] B.Z. Allison, E.W. Wolpaw, and J.R. Wolpaw. Brain computer interface systems: Progress and prospects. *British review of medical devices*, 4:463–474, 2007.

[12] Ch.F. Altmann, H.H. Bülthoff, and Z. Kourtzi. Perceptual organization of local elements into global shapes in the human visual cortex. *Curr Biol*, 13(4):342–349, 2003.

[13] Ch.F. Altmann, A. Deubelius, and Z. Kourtzi. Shape saliency modulates contextual processing in the human lateral occipital complex. *J Cogn Neurosci*, 16(5):794–804, 2004.

[14] J. Aru, T. Bachmann, W. Singer, and L. Melloni. Distilling the neural correlates of consciousness. *Neurosci. Biobehav. Rev.*, 36:737–746, 2012.

[15] Ü. Aydin, J. Vorwerk, Ph. Küpper, M. Heers, H. Kugel, A. Galka, L. Hamid, J. Wellmer, Ch. Kellinghaus, S. Rampp, and C. H. Wolters. Combining EEG and MEG for the reconstruction of epileptic activity using a calibrated realistic volume conductor model. *PLoS One*, 9(3):e93154, 2014.

[16] S. Baillet and L. Garnero. A bayesian approach to introducing anatomo-functional priors in the eeg/meg inverse problem. *IEEE Transactions on Biomedical Engineering*, 44(5):374–385, 1997.

[17] S. Baillet, J. C. Mosher, and R. M. Leahy. Electromagnetic brain mapping. *IEEE Signal Processing Magazine*, 18(6):14–30, 2001.

[18] R. Bauer and S. Heinze. Contour integration in striate cortex. classic cell responses or cooperative selection? *Experimental Brain Research*, 147(2):145–152, 2002.

[19] J. Beck. Effects of orientation and shape similarity on perceptual grouping. *Perception and Psychophysics*, 1:300–302, 1966.

[20] J. Beck, A. Rosenfeld, and R. Ivry. Line segregation. *Spatial Vision*, 4(2-3):75–101, 1989.

[21] P. Belardinelli, E. Ortiz, G. Barnes, U. Noppeney, and H. Preissl. Source reconstruction accuracy of MEG and EEG Bayesian inversion approaches. *PLoS One*, 7(12):e51985, 2012.

[22] S.R. Benbadis and D.A. Rielo. Medscape-drug and diseases- eeg artifacts, 2013.

[23] P. Berg and M. Scherg. A multiple source approach to the correction of eye artifacts. *Electroencephalography and Clinical Neurophysiology*, 90:229–241, 1994.

[24] DH. Blackwood and WJ. Muir. Cognitive brain potentials and their application. *The British Journal of Psychiatry*, (9):96–101, 1990.

[25] B. Blankertz, R. Tomioka, S. Lemm, M. Kawanabe, and K. Muller. Optimizing spatial filters for robust EEG single-trial analysis. *IEEE Signal Process. Mag.*, 25:41–56, 2008.

[26] B.Mathes, D. Trenner, and M. Fahle. The electrophysiological correlate of contour integration is modulated by task demands. *Brain Res*, 1114(1):98–112, 2006.

[27] M. Brett, IS. Johnsrude, and AM. Owen. The problem of functional localization in the human brain. *Nature Reviews Neuroscience*, 3(3):243–249, 2002.

[28] P. J. Brockwell and R. A. Davis. *Time series: theory and methods.* pringer-Verlag New York, Inc., 1986.

[29] J.S. Brumberg, A. Nieto-Castanon, P.R. Kennedy, and F.H. Guenther. Brain-computer interfaces for speech communication. *Speech Commun*, 52(4):367–379, 2010.

[30] C. Chatelle, S. Chennu, Q. Noirhomme, D. Cruse, A. M. Owen, and S. Laureys. Brain-computer interfacing in disorders of consciousness. *Brain Inj*, 26(12):1510–1522, 2012.

[31] F. H. S. Chiew, M. C. Peel, G. E. Amirthanathan, and G. G. S. Pegram. Identification of oscillations in historical global stream ow data using empirical mode decomposition. *In Proc. 7th IAHS Scientific Assembly*, pages pp. 53–62, 2005.

[32] J.-H. Cho, J. Vorwerk, C.H. Wolters, and Th.R. Knösche. Influence of the head model on EEG and MEG source connectivity analysis. *NeuroImage*, 110:60–77, 2015.

[33] Y. Choe and R. Miikkulainen. Contour integration and segmentation with self-organized lateral connections. *Biological Cybernetics*, 90(2):75–88, 2004.

[34] P. M. Claessens and J. Wagemans. Perceptual grouping in gabor lattices: proximity and alignment. perception and psychophysics. *Psychophysics*, 67(8):1446–1459, 2005.

[35] P. M. Claessens and J. Wagemans. A bayesian framework for cue integration in multistable grouping: Proximity, collinearity, and orientation priors in zigzag lattices. *Journal of Vision*, 8(7)(33):1–23, 2008.

[36] F. Cong, T. Sipola, T. Huttunen-Scott, X. Xu, T. Ristaniemi, and H. Lyytinen. Hilbert-huang versus morlet wavelet transformation on mismatch negativity of children in uninterrupted sound paradigm. *Nonlinear Biomedical Physics*, 3, 2009.

[37] K.T. Coughlin and K.K. Tung. 11-year solar cycle in the stratosphere extracted by the empirical mode decomposition method. *Advances in Space Research*, 34(2):323–329, 2004.

[38] S. C. Dakin and N. J. Baruch. Context influences contour integration. *Journal of Vision*, 9(2):1–13, 2009.

[39] J. Jr. DellaBadia, WL. Bell, JW. JR. Keyes, VP. Mathews, and SS. Glazier. Assessment and cost comparison of sleep-deprived eeg, mri and pet in the prediction of surgical treatment for epilepsy. *Seizure*, 11(5):303–309, 2002.

[40] A. Delorme and S. Makeig. Eeglab: an open source toolbox for analysis of single-trial eeg dynamics . *Journal of Neuroscience Methods*, 134:9–21, 2004.

[41] A. Delorme, T. Mullen, C. Kothe, Z. Acar, N. Bigdely-Shamlo, A. Vankov, and S. Makeig. EEGLAB, SIFT, NFT, BCILAB, and ERICA: New tools for advanced EEG processing. *Computational Intelligence and Neuroscience*, 2011:12, 2011.

[42] J.C deMunck and M.J. Peters. A fast method to compute the potential in the multi-sphere model. *IEEE Trans.Biomed. Eng.*, 40:1166–1174, 1993.

[43] E. Donchin, K. M. Spencer, and R. Wijesinghe. The mental prosthesis: assessing the speed of a p300-based brain-computer interface. *IEEE Trans Rehabil Eng.*, 8(2):174–179, 2000.

[44] P.J. Durka, A. Matysiak, E. Martinez Montes, P. Valdes Sosa, and K.J. Blinowska. Multichannel matching pursuit and EEG inverse solutions. *Journal of Neuroscience Methods*, 148:49 – 59, 2005.

[45] B.J. Edelmann, N. Johnson, A. Sohrabpour, S. Tong, N. Thakor, and B. He. Systems engibneering: Understanding and interacting with the brain. *Engineering*, 1(3):292–308, 2015.

[46] J. Eriksson, A. Larsson, and L. Nyberg. Item-specific training reduces prefrontal cortical involvement in perceptual awareness. *J. Cogn. Neurosci.*, 20:1777–1787, 2008.

[47] R. Faltermeier, A. Zeiler A, AM. Tomé, A. Brawanski, and EW. Lang. Weighted Sliding Empirical Mode Decomposition. *Advances Adaptive Data Analysis*, 3:509–526, 2011.

[48] R. Faltermeier, I.R. Keck, A. Zeiler A, AM. Tomé, A. Brawanski, and EW. Lang. Sliding Empirical Mode Decomposition. In *Neural Networks (IJCNN), The 2010 International Joint Conference on*, pages 1–9. IEEE, 2010.

[49] L. A. Farwell and E. Donchin. Talking off the top of your head: toward a mental prosthesis utilizing event-related brain potentials. *Electroencephalogr Clin Neurophysiol*, 70(6):510–523, 1988.

[50] J. Feldman. Bayesian contour integration. *Perception and Psychophysics*, 63(7):1171–1182, 2001.

[51] D.J. Felleman and D.C. van Essen. Distributed hierarchical processing in the primate cerebral cortex. *Cereb. Cortex*, 1:1–47, 1991.

[52] D.H. Fender. *Source localization of brain electrical activity.*, chapter Methods of Analysis of Brain Electrical and Magnetic Signals, A.S.Gevins and A. Remond (Eds.), pages 355–403. Elsevier, Amsterdam.

[53] D.H. Fender. Models of the human brain and the surrounding media: their influence on the reliability of source localization. *Journal of Clinical Neurophysiology*, 8:381–390, 1991.

[54] D.J. Field, A. Hayes, and R.F. Hess. Contour integration by the human visual system: evidence for a local "association field". *Vision Res*, 33(2):173–193, 1993.

[55] S. Finke. évalution la méthode conventionnelle et la méthode réciproque pour résolution du probléme direct en électroencéphalographie, 1998.

[56] S. Finke, R.M Gulrajani, and J. Gotman. Conventional and reciprocal approaches to the inverse dipole localization problem of electroencephalography. *IEEE Trans. Biomed. Eng.*, 50(6):657–666, 2003.

[57] B. J. Fisch. *Fisch and Spehlmann's EEG Primer: Basic Principles of Digital and Analog EEG*. Elsevier, 1999.

[58] P. Flandrin and P. Gonçalvès. Empirical mode decompositions as data-driven wavelet-like expansions. *Int. J. Wavelets Multiresolut. Inform. Process.*, 2:477–496, 2004.

[59] P. Flandrin, G. Rilling, and P. Gonçalvès. Empirical mode decomposition as a filter bank. *IEEE Signal Process.*, 11:112–114, 2004.

[60] D.J. Fletcher, A. Amir, D.L. Jewett, and G. Fein. Improved method for computation of potentials in a realistic head shape model. *IEEE Trans Biomed Eng.*, 42:1049–1104, 1995.

[61] P. Fries. A mechanism for cognitive dynamics: Neuronal communication through neuronal coherence. *Trends Cogn. Sci.*, 9:474–480, 2005.

[62] M. Fuchs, J. Kastner, M. Wagner, S. Hawes, and J.S. Ebersole. A standardized boundary element method volume conductor model. *Clin Neurophysiol*, 113(5):702–712, 2002.

[63] W. S. Geisler, J. S. Perry, B. J. Super, and D. P. Gallogly. Edge co-occurrence in natural images predicts contour grouping performance. *Vision Research*, 41(6):711–724, 2001.

[64] A.S. Gevins, J. Le, N. Martin, P. Bricked, J. Desmond, and B. Reutter. High resolution eeg: 124-channel recording, spatial deblurring and mri integration methods. *Electroenceph Clin Neurophysiol*, 90:337–358, 1994.

[65] Z. Gigus and J. Malik. Detecting curvilinear structure in images (tech. rep.). *University of California.*, 1991.

[66] A. Gilad, E. Meirovithz, and H. Slovin. Population responses to contour integration: early encoding of discrete elements and late perceptual grouping. *Neuron*, 78(2):389–402, 2013.

[67] R. Grech, J. Muscat T. Cassar, K.P. Camilleri, S.G Fabri, M. Zervakis, P. Xanthopoulos, V. Sakkalis, and B. Vanrumste. Review on solving the inverse problem in eeg source analysis. *J. Neuroeng. Rehabil.*, 5(25):1–33, 2008.

[68] R.E. Greenblatt, A. Ossadtchi, and M. E. Pflieger. Local linear estimators for the bioelectromagnetic inverse problem. *IEEE Trans. on Signal Processing*, 53:3403–3412, 2005.

[69] S. Grossberg and L. Pessoa. Texture segregation, surface representation and figure-ground separation. *Vision Research*, 38(17):2657–2684, 1998.

[70] F. Gulli. Gale encyclopedia of mental disorders. *Gale Group Inc*, 2003.

[71] RM. Gulrajani. *Bioelectricity and Biomagnetism*. New York: John Wiley & Sons, Inc, 1998.

[72] H. Hallez, B. Vanrumste, R. Grech, J. Muscat, W. De Clercq, A. Vergult, and I. Lemahieu. Review on solving the forward problem in eeg source analysis. *Journal of NeuroEngineering and Rehabilitation*, 4(46), 2007.

[73] S. Hanslmayr, G. Volberg, M. Wimber, S. S. Dalal, and M. W. Greenlee. Prestimulus oscillatory phase at 7 *Hz* gates cortical information flow and visual perception. *Curr Biol*, 23(22):2273–2278, 2013.

[74] B. He and L. Ding. chapter Electrophysiological Neuroimaging, pages 499–544. Springer, 2013.

[75] B. He, Y. Wang, and D. Wu. Estimating cortical potentials from scalp eegs in a realistically shaped inhomogeneous head model by means of the boundary element method. *IEEE Trans Biomed Eng*, 46:1264–1268, 1999.

[76] B. He, L. Yang, Ch. Wilke, and H. Yuan. Electrophysiological imaging of brain activity and connectivity - challenges and opportunities. *IEEE Trans. Biomed. Engineering*, 58(7):1918–1931, 2011.

[77] B. He, D. Yao, and J. Lian. High-resolution EEG: on the cortical equivalent dipole layer imaging. *Clin. Neurophysiol.*, 113:227–235, 2002.

[78] H. Helmholtz. Ueber einige gesetze der vertheilung elektrischer strme in körperlichen leitern mit anwendung aud die thierisch-elektrischen versuche. *Annals Physics and Chemistry*, 9:211–233, 1853.

[79] N. E. Huang. *Hilbert-Huang Transform and its Applications*, chapter Introduction to the Hilbert-Huang transform and its related mathematical problems. World Scientific., 2005.

[80] N. E. Huang, Z. Shen, S. R. Long, M. L. Wu, H. H. Shih, Q. Zheng, N. C. Yen, C. C. Tung, and H. H. Liu. The empirical mode decomposition and Hilbert spectrum for nonlinear and nonstationary time series analysis. *Proc. Roy. Soc. London A 8*, 454:903–995, 1998.

[81] N. E. Huang, Z. Shen, S. R. Long, M. L. Wu, H. H. Shih, Q. Zheng, N. C. Yen, C. C. Tung, and H. H. Liu. A new view of nonlinear water waves: the hilbert spectrum. *Annual Reviews of Fluid Mechanics*, 31:417–457, 1999.

[82] N. E. Huang, M.-L. C. Wu, S.R. Long, S. S.P Shen, W. Qu, P. Gloersen, and K. L. Fan. A confidence limit for the empirical mode decomposition and hilbert spectral analysis. *Proc. Roy. Soc. London A*, 459:2317–2345, 2003.

[83] N. E. Huang and Z. Wu. A review on hilbert-huang transform: Method and its applications to geophysical studies. *Rev. Geophysics*, 46(2), 2008.

[84] N. E. Huang, Z.H. Wu, S.R. Long, K. C. ARNOLD, X. CHEN, and K. BLANK. On instantaneous frequency. *Advances in Adaptive Data Analysis*, 1(2):177–229, 2009.

[85] W. Huang, Z. Shen, N.E. Huang, and Y.C. Fung. Use of intrinsic modes in biology: Examples of indicial response of pulmonary blood pressure to $\pm$ step hypoxia. *Proceedings of the National Academy of Sciences of the United States of America*, 95(22):12766–12771, 1998.

[86] A. Ikkai, A. W. McCollough, and E. K. Vogel. Contralateral delay activity provides a neural measure of the number of representations in visual working memory. *J Neurophysiol*, 103:1963–1968, 2010.

[87] F. Imamoglu, J. Heinzle, A. Imfeld, and J.-D. Haynes. Activity in high-level brain regions reflects visibility of low-level stimuli. *NeuroImage*, 2014.

[88] H.H. Jasper. The ten-twenty electrode system of the international federation. *Electroencephalogr Clin Neurophysiol*, 10:371–375, 1958.

[89] M.A. Jatoi, N. Kamel, A. S. Malik, I. Faye, and T. Begum. A survey of methods used for source localization using EEG signals. *Biomed. Signal Process. Control*, 11:42–52, 2014.

[90] J.J.Vidal. Toward direct brain-computer communication. *Annual Review of Biophysics and Bioengineering*, 2(1):157–180, 1973.

[91] J.J.Vidal. Real-time detection of brain events in eeg. *IEEE Proceedings*, 65(5):633–641, 1977.

[92] C. Johnson. *The Biomedical Engineering Handbook*, chapter Numerical methods for bioelectric field problems, pages 162–180. Florida: CRC Press, 1995.

[93] R.Jr. Johnson. Event-related brain potentials. in: I. litvan and y. agid (eds.), progressive supranuclear palsy: Clinical and research approaches. *New York: Oxford University Press*, pages 122–154, 1992.

[94] V. Jurcak, D. Tsuzuki, and I. Dan. 10/20, 10/10, and 10/5 systems revisited: their validity as relative head-surface-based positioning systems. *Neuroimage*, 34(4):1600–1611, 2007.

[95] k. Takahashi, M. Saleh, R.D. Penn, and N.G. Hatsopoulos. Propagating waves in human motor cortex. *Frontiers Research Foundation*, 5:40, 2011.

[96] E.S. Kappenman and S.J. Luck. *The Oxford Handbook of Event-Related Potential Components.* 2012.

[97] A. Keil, M. M. Müller, W. J. Ray T. Gruber, and T. Elbert. Human gamma band activity and perception of a gestalt. *The Journal of Neuroscience*, 19:7152–7161, 1999.

[98] P. R. Kennedy, R. A. Bakay, M. M. Moore, K. Adams, and J. Goldwaithe. Direct control of a computer from the human central nervous system. *IEEE Trans Rehabil Eng.*, 8(2):198–202, 2000.

[99] C. Koch and G. Laurent. Complexity and the nervous system. *American Association for the Advancement of Science*, 284(5411):96 – 98, 1999.

[100] K. Koffka. Principles of gestalt psychology. *New York: Hartcourt.*, 1935.

[101] Z Koles. Trends in eeg source localization. *Electroenceph Clin Neurophysiol*, 106:127–137, 1998.

[102] Y. Kopsinis and S. McLaughlin. Improved emd using doubly-iterative sifting and high order spline interpolation. *EURASIP J. Advances Signal processing*, page 6, 2008.

[103] Y. Kopsinis and S. McLaughlin. Investigation and performance enhancement the empirical mode decomposition method based on a heuristic search optimization approach. *IEEE Trans.Signal Processing*, 56(1):1–13, 2008.

[104] C. Kothe. BCILAB, 2012.

[105] C. A. Kothe and S. Makeig. BCILAB: a platform for brain-computer interface development. *J Neural Eng.*, 10(5):056014, 2013.

[106] Z. Kourtzi, A.S. Tolias, Ch.F. Altmann, M. Augath, and N.K. Logothetis. Integration of local features into global shapes: monkey and human FMRI studies. *Neuron*, 37(2):333–346, 2003.

[107] I. Kovacs. Gestalten of today: Early processing of visual contours and surfaces. *Behavioral Brain Research*, 82(1):1–11, 1996.

[108] I. Kovacs. Human development of perceptual organization. *Vision Res.*, 40:1301–1310, 2000.

[109] I. Kovacs and B. Julesz. A closed curve is much more than an incomplete one:effect of closure in figure-ground segmentation. *Proceedings of the National Academy of Sciences of the United States of America*, 90:7495–7497, 1993.

[110] T. Kubota. Massively parallel networks for edge localization and contour integration-adaptable relaxation approach. *Neural Networks: The Official Journal of the International Neural Network Society*, 17(3):411–425, 2004.

[111] V.A.F. Lamme and P.R. Roelfsma. The distinct modes of vision offered by feedforward and recurrent processing. *Trends Neurosci*, 23:571–579, 2000.

[112] J. L. Lancaster, M. G. Woldorff, L. M. Parsons, M. Liotti, C. S. Freitas, L. Rainey, P. V. Kochunov, D. Nickerson, S. A. Mikiten, and P. T. Fox. Automated talairach atlas labels for functional brain mapping. *Hum Brain Mapp*, 10(3):120–131, 2000.

[113] J.-C. Lee, P. S. Huang, T.-M. Tu, and C.-P. Chang. Recognizing human iris by modified empirical mode decomposition. *In Adv. Image Video technology,Springer Berlin*, 4872:298–310, 2007.

[114] S. H. Lee and R. Blake. Neural synergy in visual grouping: When good continuation meets common fate. *Vision Research*, 41(16):2057–2064, 2001.

[115] T. W. Lee, M. Girolami, and T. J. Sejnowski. ndependent component analysis using an extended infomax algorithm for mixed subgaussian and supergaussian sources. *Neural Comput*, 11(2):417–441, 1999.

[116] D. Lehmann and W. Skrandies. Spatial analysis of evoked potentials in man - a review. *Progr Neurobiol*, 23:227–250, 1984.

[117] Y. Lelievre, Y. Washizawa, and T.M. Rutkowski. Single trial bci classification accuracy improvement for the novel virtual sound movement-based spatial auditory paradigm. *Asia-Pacific. IEEE*, pages 1–6, 2013.

[118] C. Y. Li and W. Li. Extensive integration field beyond the classical receptive field of cat's striate cortical neurons2̆013classification and tuning properties. *Vision Research*, 34(18):2337–2355, 1994.

[119] W. Li and CD. Gilbert. Global contour saliency and local collinear interactions. *Journal of Neurophysiology*, 88:2846–2856, 2002.

[120] Z. Li. A neural model of contour integration in the primary visual cortex. *Neural Computation*, 10(4):903–940, 1998.

[121] M. Liotti, M.G. Woldorff, R. Perez, and H. S. Mayberg. An erp study of the temporal course of the stroop color-word interference effect . *Neuropsychologia*, 2000(38):701–711, 2000.

[122] M.-T. Lo, K. Hu, Y. Liu, C.-K. Peng, and V. Novak. Multimodal pressure-flow analysis: Application of hilbert-huang transform in cerebral blood flow regulation. *EURASIP J. Adv. Sig. Proc.*, page 785243, 2008.

[123] M.-T. Lo, V. Novak, Y. Liu C.-K. Pen and, and K. Hu. Nonlinear phase interaction between nonstationary signals: A comparison study of methods based on hilbert-huang and fourier transforms. *Phys. Rev. E*, 79:061924, 2009.

[124] D. Looney, A. Hemakom, and D.P. Mandic. Intrinsic multi-scale analysis : a multivariate empirical mode decomposition framework. *Proc. R. Soc. A*, 471(20140709), 2015.

[125] S. Luck. An introduction to the event-related potential technique. *MIT Press*, pages 21–23, 2005.

[126] P. Luu, D.M. Tucker, R. Englander, A. Lockfeld, H. Lutsep, and B. Oken. Localizing acute stroke-related EEG chabges: assesing the effects od spatial undersampling. *J. Clin. Neurophysiol.*, 18(4):302–317, 2001.

[127] B. Machilsen, N. Novitskiy, K. Vancleef, and J. Wagemans. Context modulates ERP signature of contour integration. *PLoS One*, 6(9):e25151, 2011.

[128] B. Machilsen, M. Pauwels, and J. Wagemans. The role of vertical mirror symmetry in visual shape detection. *Journal of Vision*, 9(12):1–11, 2009.

[129] S. Makeig, S. Debener, J. Onton, and A. Delorme. Mining event-related brain dynamics, trends in cognitive sciences. *Trends Cogn Sci.*, 8(5):204–210, 2004.

[130] J. Malmivuo and R. Plonsey. *Bioelectric Phenomena*. New York: McGraw-Hill, 1969.

[131] J. Malmivuo and R. Plonsey. *Bioelectromagnetism: Principles and Applications of Bioelectric and Biomagnetic Fields*. New York: Oxford University Press, 1995.

[132] A. Malony, A. Salman, S. Turovets, D. Tucker, V. Volkov, K. Li, J. Song, S. Biersdorff, C. Davey, C. Hodge, and D. Hammond. Computational modeling and human head electromagnetics for source localization in milliscale brain dynamics. In *Proc. Medicine Meets Virtual Reality (MMVR'2011)*, 2011.

[133] A.P Mandic, N. Rehman, Z. Wu, and N.E. Huang. Empirical Mode Decomposition-Based Time-Frequency Analysis of Multivariate Signals: The Power of Adaptive Data Analysis. *IEEE Signal Processing Magazine*, 30(6):74–86, 2013.

[134] S. Mandon and A. K. Kreiter. Rapid contour integration in macaque monkeys. *VisionResearch*, 45(3):291–300, 2005.

[135] K. A. May and R. F. Hess. Dynamics of snakes and ladders. *Journal of Vision*, 7:1–9, 2007.

[136] J. Mazziotta, A. Toga, A. Evans, P. Fox, J. Lancaster, K. Zilles, R. Woods, T. Paus, G. Simpson, B. Pike, C. Holmes., L. Collins, P. Thompson, D. MacDonald, M. Iacoboni, T. Schormann, K. Amunts, N. Palomero-Gallagher, S. Geyer, L. Parsons, K. Narr, N. Kabani, G. Le Goualher, D. Boomsma, T. Cannon, R. Kawashima, and B. Mazoyer. A probabilistic atlas and reference system for the human brain: International consortium for brain mapping (icbm). *Philos Trans R Soc Lond B Biol Sci.*, 356(1412):1293–1322, 2001.

[137] McGill.Uni. Introductory physiology laboratory. *McGill University*, 2005.

[138] W. H. McIlhagga and K. T. Mullen. Contour integration with colour and luminance contrast. *Vision Research*, 36(9):1265–1279, 1996.

[139] S. Meignen and V. Perrier. A new formulation for empirical mode decomposition based on constrained optimization. *IEEE Signal processing Letters*, 14:932–935, 2007.

[140] C. M. Michel, M. M. Murray, G. Lantz, S. Gonzalez, L. Spinelli, and R. Grave de Peralta. Eeg source imaging. *Clin Neurophysiol*, 115(10):2195–2222, 2004.

[141] B. Mijovic, M. De Vos, K. Vanderperren, B. Machilsen, S. Sunaert, S. Van Huffel, and J. Wagemans. The dynamics of contour integration: A simultaneous EEG-MRI study. *NeuroImage*, 88:10 – 21, 2013.

[142] A. Mobascher, J. Brinkmeyer, T. Warbrick, F. Musso, H.J. Wittsack, R. Stoermer, A. Saleh, A. Schnitzler, and G. Winterer. Fluctuations in electrodermal activity reveal variations in single trial brain responses to painful laser stimuli - a fmri/eeg study. *NeuroImage*, 44(3):1081–1092, 2009.

[143] H. Morita, M. Morita, and T. Kumada. Integration process of contours defined by different attributes. *Brain Research. Cognitive Brain Research*, 15(3):324–327, 2003.

[144] J.C. Mosher, R.M. Leahy, , and P.S. Lewis. Eeg and meg: Forward solutions for inverse methods. *IEEE Trans Biomed Eng*, 46:245–259, 1999.

[145] J.C. Mosher, P.S. Lewis, and R.M Leahy. Multiple dipole modeling and localization from spatio-temporal meg data. *J. Neuroeng. Rehabil.*, 39(6):541–557, 1992.

[146] T. Mullen, A. Delorme, C. Kothe, and S. Makeig. An electrophysiological information flow toolbox for EEGLAB. *Society for Neuroscience Conference, San Diego, CA, USA*, 2010.

[147] M. M. Murray, C. Brunet, and C. M. Michel. Topographic ERP analyses: A step-by-step tutorial review. *Brain Topography*, 20:249–264, 2008.

[148] A.Y. Mutlu and S. Aviyente. Multivariate Empirical Mode Decomposition for Quantifying Multivariate Phase Synchronization. *EURASIP Journal on Advances in Signal Processing*, 2011:1–13, 2011.

[149] D. Neuffer. Prohealth, 2016.

[150] R. K. Niazy, C. F. Beckmann, G. D. Iannetti, J. M. Brady, and S. M. Smith. Removal of fmri environment artifacts from eeg data using optimal basis sets. *Neuroimage*, 28(3):720–737, 2005.

[151] N. Novitskiy, J.R. Ramautar, K. Vanderperren, M. De Vos, M. Mennes, B. Mijovic, B. Vanrumste, P. Stiers, B. Van den Bergh, L. Lagae, S. Sunaert, S. Van Huffel, and J. Wagemans. The {BOLD} correlates of the visual {P1} and {N1} in single-trial analysis of simultaneous eeg-fmri recordings during a spatial detection task. *NeuroImage*, 54(2):824 – 835, 2011.

[152] U.S. National Library of Medicine. Trusted health information for you.

[153] S. Olbrich, C. Mulert, S. Karch, M. Trenner, G. Leicht, O. Pogarell, and U. Hegerl. Eeg-vigilance and bold effect during simultaneous eeg/fmri measurement. *NeuroImage*, 45(2):319–332, 2009.

[154] R. Oostenveld and P. Praamstra. The five percent electrode system for high-resolution eeg and erp measurements. *Clin Neurophysiol*, 112:713–719, 2001.

[155] R. D. Pascual-Marqui. Low resolution brain electromagnetic tomography (LORET A) functional imaging in acute, neuroleptic-naive,first-episode, productive schizophrenia. *Psychiatry Res*, 90(2):169–179, 1999.

[156] R. D. Pascual-Marqui. Standardized low-resolution brain electromagnetic tomography (sLORET A) : technical details. *Find Exp Clin Pharmacal*, 24:5–12, 2002.

[157] R. D. Pascual-Marqui. Sdiscrete, 3d distributed, linear imaging methods of electric neuronal activity. part 1: Exact, zero error localization,, 2007.

[158] R. D. Pascual-Marqui. *Quantitative EEG Analysis: Methods and Clinical Applications*, chapter Theory of the EEG Inverse Problem, pages 121–140. Artech House, Boston, 2009.

[159] R. D. Pascual-Marqui. Assessing interactions in the brain with exact low-resolution electromagnetic tomography. *Philos Trans A Math Phys Eng Sci*, 369:3768–3784, 2011.

[160] R. D. Pascual-Marqui, C. M. Michel, and D.Lehmann. Low resolution electromagnetic tomography: a new method for localizing electrical activity in the brain. *Int J Psychophysiol*, 18(1):49–65, 1994.

[161] H. Pashler. Cross-dimensional interaction and texture segregation. *Perception and Psychophysics*, 43(4):307–318, 1988.

[162] SC. Dakin PD. Butler, SM. Silverstein. Visual perception and its impairment in schizophrenia. *Biol. Psychiatry*, 64(1):40–47, 2008.

[163] M. C. Peel, G. E. Amirthanathan, G. G. S. Pegram, T. A. McMahon, and F. H. S. Chiew. Issues with the application of empirical mode decomposition analysis. *In MODSIM 2005, Int. Congress Modelling Simulation, A. Zerger and R: M. Argent, eds.*, pages 1681–1687, 2005.

[164] M. C. Peel, G. G. S. Pegram, and T. A. McMahon. Empirical mode decomposition:improvement and application. *In Proc. Int. Congress Modelling Simulation*, 1(Modelling and Simulation Society of Australia,Canberra):2996–3002, 2007.

[165] M. W. Pettet, S. P. McKee, and N. M. Grzywacz. Constraints on long range interactions mediating contour detection. *Vision Research*, 38(6):865–879, 1998.

[166] pinterest.

[167] R. Plonsey. *The Biomedical Engineering Handbook*, chapter Volume Conductor Theory, pages 119–125. CRC Press, 1995.

[168] C. M. Michel R. Martuzzi S. G. Andino R. Menendez, M. M. Murray. Electrical neuroimaging based on biophysical constraints. *Neuroimage*, 21(2):527–539, 2004.

[169] R. R. Ramiŕez. Source localization. *Scholarpedia*, 3(11):1733, 2008. revision 150342.

[170] N. Rehman and D. P. Mandic. Multivariate empirical mode decomposition. *Proceedings of the Royal Society A: Mathematical, Physical and Engineering Sciences*, 466(2117):1291–1302, 2009.

[171] N. Rehman and D. P. Mandic. Filter Bank Property of Multivariate Empirical Mode Decomposition. *IEEE Transactions on Signal Processing*, 59(5):2421–2426, 2011.

[172] N. Rehman, C. Park, N. E. Huang, and D. P. Mandic. EMD via MEMD: multivariate noise-aided computation of standard EMD. *Advances in Adaptive Data Analysis*, 05(02):1350007, 2013.

[173] R. Ramírez Rey, Wipf Daved, and Baillet Sylvain. *Neuroelectromagnetic Source Imaging of Brain Dynamics*, volume 38, chapter 8, pages 127–155. Springer New York, 2010.

[174] G. Rilling and P. Flandrin. On the influence of sampling on the empirical mode decomposition. *Proceedings of IEEE International Conference on Acoustic, Speech and Signal Processing ICASSP-06*, 06, 2006.

[175] G. Rilling and P. Flandrin. One or two frequencies? the empirical mode decomposition answers. *IEEE Trans. on Signal Proc.*, 56(1):85–95, 2008.

[176] G. Rilling and P. Flandrin. Sampling effects on the empirical mode decomposition. *Advances in Adaptive Data Analysis*, 1(1):43–59, 2009.

[177] G. Rilling, P. Flandrin, and P. Gon ¸calv ` es. Empirical mode decomposition, fractional gaussian noise and hurst exponent estimation. *In Proceedings of IEEE International Conference on Acoustic, Speech and Signal Precessing.*, 4, 2005.

[178] G. Rilling, P. Flandrin, and P. Gonçalv ` es. On empirical mode decomposition and its algorithms. *In Proc. 6th IEEE-EURASIPWorkshop on Nonlinear Signal andImage Processing.*, 2003.

[179] P. R. Roelfsema, H. S. Scholte, and H. Spekreijse. Temporal constraints on the grouping of contour segments into spatially extended objects. *Vision Research*, 39(8):1509–1529, 06.

[180] P.R. Roelfsema. Cortical algorithms for perceptual grouping. *Annu Rev Neurosci*, 29:203–227, 2006.

[181] V. Rojansky. *Electromagnetic fields and waves*. Dover books on physics, 1971.

[182] M. Rullmann, A. Anwander, M. Dannhauer, S. Warfield, F. Duffy, and C. Wolters. Eeg source analysis of epileptiform activity using a 1 mm anisotropic hexahedra finite element head model. *NeuroImage*, 44(2):399–410, 2009.

[183] T. M. Rutkowski, F. Vialatte, A. Cichocki, D. Mandic, and A. K. Barros. Auditory feedback for brain computer interface management - an EEG data sonification approach. *Knowledge-Based Intelligent Information and Engineering Systems*, 4253:1232–1239, 2006.

[184] O. Ryyänen, J. Hyttinen, P. Laarne, and J. Malmivuo. Effect of electrode density and measurement noise on the spatial resolution of cortical potential distribution. *IEEE Trans. Biomed. Eng.*, 51(9):1547–1554, 2004.

[185] O. Ryynänen, J. Hyttinen, and J. Malmivuo. Effect of measurement noise and electrode density on the spatial resolution of cortical potential distribution with different resistivity values for the skull. *IEEE Trans. Biomed. Eng.*, 53(9):1851–1858, 2006.

[186] J. M. Samonds, Z. Zhou, M. R. Bernard, and A. B. Bonds. Synchronous activity in cat visual cortex encodes collinear and cocircular contours. *Journal of Neurophysiology*, 95(4):2602–2616, 2006.

[187] D. T. Sandwell. Biharmonic spline interpolation of geos-3 and seasat altimeter data: Geophys. *Res. Lett.*, 14(2):139–142, 1987.

[188] J. Sarvas. Basic mathematical and electromagnetic concepts of the biomagnetic inverse problem. *Phys Med Biol*, 32:11–22, 1987.

[189] G. Schalk and J. Mellinger. *A Practical Guide to Brain-Computer Interfacing with BCI2000*. 2010.

[190] G. Schalk, J. R. Wolpaw, D. J. McFarland, and G. Pfurtscheller. Eeg-based communication: presence of an error potential. *Clin Neurophysiol*, 111(12):2138–2144, 2000.

[191] N. Schinkel, K. R. Pawelzik, and U. A. Ernst. *Robust integration and detection of noisy contours in a probabilistic neural model.*, volume 65-66C. 2005.

[192] R. Schmidt. Multiple emitter location and signal parameter estimation. *IEEE Trans*, 34(3):276–280, 1986.

[193] W. Schneider and J.M. Chein. Controlled & automatic processing: behavior, theory, and biological mechanisms. *Cognitive Science*, 27:525–559, 2003.

[194] M. Schwartz, W.R. Bennett, and S. Stein. *Communications systems and techniques*. New York: McGraw-Hill, 1966.

[195] K. Sekihara, S.S. Nagarajan, D. Poeppel, A. Marantz, and Y. Miyashita. Reconstructing spatio-temporal activities of neural sources using an MEG vector beamformer technique. *IEEE Trans. Biomed. Eng.*, 48:760–771, 2001.

[196] K. Sekihara, M. Sahani, and S. S. Nagarajan. Localization bias and spatial resolution of adaptive and nonadaptive spatial filters for meg source reconstruction. *NeuroImage*, 25:1056–1067, 2005.

[197] DW. Shattuck, M. Mirza, V. Adisetiyo, C. Hojatkashani, G. Salamon, KL. Narr, RA. Poldrack, RM. Bilder, and AW. Toga. Construction of a 3D probabilistic atlas of human cortical structures. *Neuroimage*, 2007.

[198] M. Shpaner, S. Molholm, E. Forde, and J.J. Foxe. Disambiguating the roles of area V1 and the lateral occipital complex (LOC) in contour integration. *Neuroimage*, 69:146–156, 2013.

[199] D.U. Silverthorn. *Human Physiology: An Integrated Approach (5th Edition)*. 2009.

[200] A. Sohrabpour, Y. Lu, P. Kankirawatana, J. Blount, H. Kim, and B. He. Effect of EEG electrode number on epileptic source localization in pediatric patients. *Clin Neurophysiol.*, 126(3):472–480, 2015.

[201] J. Song, C. Davey, C. Poulsen, Ph. Luu, S. Turovets, E. Anderson, K. Li, and D. Tucker. EEG source localization: Sensor density and head surface coverage. *J. Neurosci. Methods*, 256:9–21, 2015.

[202] J. Song, K. Morgan, T. Sergei, K. Li, C. Davey, P. Govyadinov, P. Luu, K. Smith, F. Prior, L. Larson-Prior, and D. Tucker. Anatomically accurate head models and their derivatives for dense array EEG source localization, functional neurology. *Rehabil. Ergon.*, 3(2):275–294, 2013.

[203] N. Stevenson, M. Mesbah, and B. Boashash. A sampling limit for the empirical mode decomposition. *Proceedings of International Symposium on Signal Processing and its Applications*, 55(3):647–650, 2005.

[204] F. Tadel, S. Baillet, J.C. Mosher, D. Pantazis, and R.M. Leahy. Brainstorm: A user-friendly application for MEG/EEG analysis. *Computational Intelligence and Neuroscience*.

[205] A. Tarantola. *Inverse Problem Theory and Methods for Model Parameter Estimation (SIAM).* Society for Industrial and Applied Mathematics Philadelphia, PA, USA, 2005.

[206] L. Tarokh. Eeg oscillations induced by contour closure in a noisy visual field. *Behav Brain Res*, 196:55–62, 2009.

[207] M.J. Taylor and T. Baldeweg. Application of eeg, erp and intracranial recordings to the investigation of cognitive functions in children. *Developmental Science*, 5(3):318–334, 2002.

[208] N. Tsakalozos, K. Drakakis, and S. Rickard. A formal study of the nonlinearity and consistency of the empirical mode decomposition. *Signal Processing*, 92(9):1961–1969, 2012.

[209] W. R. Uttal, N. S. Davis, C. Welke, and R. Kakarala. The reconstruction of static visual forms from sparse dotted samples. *Perception and Psychophysics*, 43(3):223–240, 1988.

[210] B. Vanrumste. Eeg dipole source analysis in a realistic head model. *PhD thesis. Ghent University*, 2001.

[211] B. Vanrumste, G. Van Hoey, R. Van de Walle, P. Van Hese, M. DH́ave, P. Boon, and I. Lemahieu. The realistic versus the spherical head model in eeg dipole source analysis in the presence of noise. *Proceedings of the 23rd Annual International Conference of the IEEE*, 1:994–997, 2001.

[212] F. Varela, J.-P. Lachaux, E. Rodriguez, and J. Martineri. The brainweb: phase synchronisation and large-scale integration. *Nature Reviews:Neuroscience*, 2:228–239, 2001.

[213] P. Vitali, C. Di Perri, A.E. Vaudano, St. Meletti, and F. Villani. Integration of multimodal neuroimaging methods: a rationale for clinical applications of simultaneous EEG-fMRI. *Functional Neurology*, 30(1):9–20, 2015.

[214] G. Volberg. Right-hemisphere specialization for contour grouping. *Experimental Psychology*, pages 1–9, 2014.

[215] G. Volberg, M. Artinger, M. Becker, M. Traurig, J. Binapfl, M. Tahedl, and U. Zach. Visual working memory and grouping., 2016.

[216] G. Volberg and M.W. Greenlee. Brain networks supporting perceptual grouping and contour selection. *Frontiers in Psychology*, 5(264), 2014.

[217] G. Volberg, A. Wutz, and M. W. Greenlee. Top-down control in contour grouping. *PLoS ONE*, 8(1):e54085, 2013.

[218] J. Vorwerk, M. Clerc, M. Burger, and C. H. Wolters. Comparison of boundary element and finite element approaches to the EEG forward problem. *Biomed Tech*.

[219] M. Wagner, M. Fuchs, and J. Kastner. Evaluation of sloreta in the presence of noise and multiple sources. *Brain Topogr*, 16(4):277–280, 2004.

[220] M. Wagner, M. Fuchs, and J. SWARM. sloreta-weighted accurate minimum-norm inverse solutions. *Proceedings of the 15th International Conference on Biomagnetism*, page 1300, 2007.

[221] G. Wang and D. Ren. Effect of brain-to-skull conductivity ratio on EEG source localization accuracy. *BioMed. Res. Int.*, page 459346, 2013.

[222] W. Wang, A.D. Degenhart, G.P. Sudre, D.A. Pomerleau, and E.C. Tyler-Kabara. Decoding semantic information from human electrocorticographic (ecog) signals. *Engineering in Medicine and Biology Society, EMBC, 2011 Annual International Conference of the IEEE.*, pages 6294–6298, 2011.

[223] Z. Wang and B. S. Peterson. Partner-matching for the automated identification of reproducible ica components from fmri datasets: algorithm and validation. *Human Brain Mapping*, 29(8):875–893, 2008.

[224] Y. Washizawa, T. Tanaka, D. P. Mandic, and A. Cichocki. A flexible method for envelope estimation in empirical mode decomposition. In *in Proceedings of the 10th International Conference on Knowledge-Based Intelligent Information and Engineering Systems, (KES'06), B. Gabrys, R. J. Howlett, and L. C. Jain, Eds.*, volume 4, pages 1248–1255, 2006.

[225] K. Wendel, O. Väisänen, J. Malmivuo, N.G. Gencer, B. Vanrumste, P. Durka, R. Magjarevic, S. Supek, M.L. Pascu, H. Fontenelle, and R. Grave de Peralta Menendez. EEG/MEG source imaging: Methods, challenges and open issues. *Comput. Intelligence Neuroscience*, ID 656092:1–12, 2009.

[226] M. Wertheimer. Laws of organization in perceptual forms. *London, UK: Harcourt (Brace & Jovanovich*, 1938.

[227] M. Wertheimer. Principles of perceptual organization. *Readings in perception. Princeton: Van Nostrand*, 1958.

[228] K. Whittingstall, G. Stroink, L. Gates, J. Connolly, and A. Finley. Effects of dipole position, orientation and noise on the accuracy of eeg source localization. *BioMedical Engineering OnLine*, 2(14), 2003.

[229] Wikipedia. Electroencephalography, 2001.

[230] J.R. Wolpaw, J.R. Birbaumer, D.J. McFarland, G. Pfurtscheller, and T.M. Vaughan. Brain-computer interfaces for communication and control. *Clin Neurophysiol*, 113(6):767–791, 2002.

[231] J.R. Wolpaw and E.W.Wolpaw. *Brain-Computer Interfaces: Principles and Practice*, chapter Brain-Computer Interfaces: Something New Under the Sun. Oxford University Press, 2012.

[232] G. F. Woodman and S. J. Luck. Dissociations among attention, perception, and awareness during object-substitution masking. *Psychological Science*, 14:605–611, 2003a.

[233] G. F. Woodman and S. J. Luck. Serial deployment of attention during visual search. *Journal of Experimental Psychology: Human Perception and Performance.*, 29:121–138, 2003b.

[234] Z. Wu, E. Schneider, Z. Hu, and L. Cao. The impact of global warming on enso variability in climate records. *Technical report, Center for Ocean-Land-Atmosphere Studies.*, 110(25), 2001.

[235] Zh. Wu and N. E. Huang. A study of the characteristics of white noise using the empirical mode decomposition method. *Proc. Roy. Soc. London,A460*, pages 1597–1611, 2004.

[236] Zh. Wu and N. E. Huang. Ensemble Empirical Mode Decomposition: a noise-assisted data analysis method. *Adv. Adaptive Data Analysis*, 1(1):1–41, 2009.

[237] Zh. Wu, N. E. Huang, and X. Chen. The Multidimensional Ensemble Empirical Mode Decomposition Method. *Adv. Adaptive Data Analysis*, 1:339–372, 2009.

[238] A. Zeiler. Weighted sliding empirical mode decomposition and its application to neuromonitoring data. *Ph.D. thesis, Regensburg Uninversity, Germany.*, 2012.

[239] A. Zeiler, R. Faltermeier, A. Brawanski, A. M.Tomé, C. G. Puntonet, J. M. Górriz, and E. W. Lang. Brain status data analysis by sliding emd. *LNCS*, 6687:77–87, 2011.

[240] A. Zeiler, R. Faltermeier, A. M.Tomé, I. Keck, C. G. Puntonet, A. Brawanski, and E. W. Lang. Sliding empirical mode decomposition-brain status data analysis and modeling. *P. Georgieva, L. Mihaylova, and L. C. Jain, eds., Advances in Intelligent Signal Processing and Data Mining*, 410:311–349, 2013.

[241] A. Zeiler, R. Faltermeier, A. M.Tomé, C. G. Puntonet, A. Brawanski, and E. W. Lang. Sliding empirical mode decomposition for online analysis of biomedical time series. *LNCS*, 6691:299–306, 2011.

[242] A. Zeiler, R. Faltermeier, A. M.Tomé, C. G. Puntonet, A. Brawanski, and E. W. Lang. Weighted sliding empirical mode decomposition for online analysis of biomedical time series. *Neural Process Lett*, pages 1–12, 2012.

[243] Z. Zhang. A fast method to compute surface potentials generated by dipoles within multilayer anisotropic spheres. *Phys. Med. Biol.*, 40:335–349, 1995.